




Universitetet
i Stavanger

FACULTY OF SCIENCE AND TECHNOLOGY

MASTER'S THESIS

Study programme/specialisation: Master of Science in Petroleum Engineering/ Natural Gas	Spring semester, 2020. Open access
Author: Sandra Knutsen	 (Author's signature)
Supervisors: Prof. Arild Saasen Dr. Mahmoud Khalifeh	
Title of master's thesis: Use of the Quemada Model for Modelling Viscous Behaviour of Drilling Fluids.	
Credits: 30 ECTS	
Keywords: Quemada model Herschel-Bulkley model Yield stress Rheology Viscosity Flow curves	Number of pages: XIII + 55 + supplemental material/other: 16 Stavanger, 15th July 2020

**Use of the Quemada Model for Modelling Viscous Behaviour of
Drilling Fluids**

By

Sandra Knutsen

Master's Thesis

Presented to the Faculty of Science and Technology

The University of Stavanger

THE UNIVERSITY OF STAVANGER

JULY 2020

Acknowledgement

I would like to extend my sincere gratitude to my supervisors, Prof. Arild Saasen and Dr. Mahmoud Khalifeh, for guiding and supporting me throughout the process of writing this thesis.

Besides my supervisors, I would like to take this opportunity to thank Silje Slåttsveen for helping with the English grammar corrections, and to thank Kim André Vorland, Head Engineer at the Faculty of Science and Technology at UiS, for teaching me how to use the Anton Paar MCR 302 Rheometer.

Abstract

Drilling fluids are essential for drilling operations and serve many important functions. To maintain control of the wellbore, while ensuring sufficient cutting transportation, good understanding of the rheological properties and behaviours of drilling fluids are required. The rheological behaviours of drilling fluids are often unknown for the relevant range of shear rates, making available models a necessity when simulating their rheological behaviour. Traditionally, the drilling industry uses simple models when simulating the viscosity profile of drilling fluids, e.g. Herschel-Bulkley or Power Law. However, the accuracy of these models can be questioned. Therefore, this study investigated the use of the Quemada model for modelling viscous behaviour of drilling fluids, while the Herschel-Bulkley model was used to serve as a basis of comparison.

The shear stress/shear rate relationship was measured by OFITE Model 900 and Anton Paar MCR 302 to analyse the fluid properties and behaviours. The drilling fluids were also exposed to simulated well conditions (elevated temperatures and dynamic ageing) to characterise their rheological change. The Herschel-Bulkley model curves were fitted with nonlinear regression by reducing the residual sum of squares (RSS), where the shear rate range had to be limited to $0.0511\text{-}287\text{ s}^{-1}$ to improve model accuracy. This resulted in models able to describe the characterised rheological behaviours of the drilling fluids with decent accuracy. The Quemada model was curve fitted for the entire measured shear rate range of $0.0511\text{-}1020\text{ s}^{-1}$ with nonlinear regression by using the weighted least square (WLS) method. Additionally, the infinite- and zero-shear viscosities were treated as curve fitting values. This yielded one highly accurate solution for all viscosity profiles, where most of the curves had indications of the infinite- and zero-shear plateaus due to the extensive shear rate range. This resulted in good estimations of the infinite- and zero-shear plateaus.

Nomenclature

Abbreviations

APE	Absolute Percentage Error
API	American Petroleum Institute
BHA	Bottom Hole Assembly
EVF	Effective Volume Fraction
GRG	Generalised Regression Gradient
HSR	High Shear Rate
IF	Individual Floc
LSR	Low Shear Rate
lpm	Litre per Minute
MAPE	Mean Absolute Percentage Error
n.d.	No Date
OBDF	Oil Based Drilling Fluid
OWR	Oil Water Ratio
rpm	Revolutions per Minute
SBF	Synthetic Based Fluid
ROP	Rate of Penetration
RSS	Residual Sum of Squares
SU	Structural Unit
WBDF	Water Based Drilling Fluid
WLS	Weighted Least Square

Symbols

Γ	Dimensionless Shear Variable
$\dot{\gamma}$	Shear Rate [1/s]
$\dot{\gamma}_c$	Characteristic Shear Rate [1/s]
$\dot{\gamma}_s$	Specified Shear Rate [1/s]
$\dot{\gamma}_{NW}$	Newtonian Wall Shear Rate [1/s]
$\dot{\gamma}_W$	Wall Shear Rate [1/s]
η	Shear Viscosity [Pa·s]
η_∞	Infinite-Shear Viscosity [Pa·s]
η_0	Zero-Shear Viscosity [Pa·s]
η_F	Suspension Fluid Viscosity [Pa·s]
η_{eff}	Effective Viscosity [Pa·s]
κ_A	Shear-Dependent Kinetic Constant [1/s]
κ_D	Shear-Dependent Kinetic Constant [1/s]
μ_p	Plastic Viscosity [Pa·s]
ρ	Density [kg/m ³]
τ	Shear Stress [Pa]
τ_0	Yield Stress [Pa]
τ_W	Wall Shear Stress [Pa]
τ_c	Characteristic Shear Stress [Pa]
τ_s	Surplus Shear Stress [Pa]
ϕ	Solid Volume Fraction
ϕ_∞	Infinite-Shear Maximum Packing Fraction
ϕ_0	Zero-Shear Maximum Packing Fraction
ϕ_A	Aggregated Volume Fraction
$\phi_{A\infty}$	Infinite-Shear Aggregated Volume Fraction
ϕ_{A0}	Zero-Shear Aggregated Volume Fraction
ϕ_m	Maximum Packing Fraction
φ	Mean Compactness
χ	Structural Index
A	Area [m], Arrhenius Relationship Liquid Constant [Pa·s]
B	Arrhenius Relationship Liquid Constant [K]
a	Particle Radius [m]

C	Compactness Factor
D	Diameter [m]
D_i	Inner Diameter [m]
D_o	Outer Diameter [m]
dp/dz	Frictional Pressure Drop [Pa/m]
F	Force [N]
h	Height [m]
k	Herschel-Bulkley Consistency Index [Pa·s ⁿ]
N_p	Number of Measurement Points
n	Herschel-Bulkley Flow Behaviour Index
n'	Local Power Law Index
p	Shear Exponent
Q	Volumetric Flow Rate [m ³ /s]
S	Structural Variable
S_∞	Infinite-Shear Structural Variable
S_0	Zero-Shear Structural Variable
S_{eq}	Structural Variable at Steady State
T	Temperature [°C, K]
t_A	Mean Relaxation Time [s]
t_D	Mean Relaxation Time [s]
t_c	Characteristic Time [s]
V	Volume [m ³]
v	Velocity [m/s]
\bar{v}	Average Velocity [m/s]
W_I	Particle Interaction Energy [J]
w_i	Weight in Least Square Regression
y_i	General Measured Values
\hat{y}_i	General Model Values

List of Contents

Acknowledgement.....	3
Abstract	4
Nomenclature	5
List of Contents	8
List of Figures	10
List of Tables.....	12
1 Introduction	1
1.1 Objective and Limitations	2
2 Theory	3
2.1 Rheology	3
2.1.1 Shear Stress, Shear Rate, and Shear Viscosity	3
2.1.2 Rotational Principles	4
2.1.3 Flow and Viscosity Curves	5
2.1.4 Effects of Temperature and Ageing on Drilling Fluid Rheology.....	7
2.2 Rheology Models	7
2.2.1 Herschel-Bulkley Model	9
2.2.2 Quemada Model	10
2.3 Model Application.....	11
2.3.1 Nonlinear Regression	11
2.3.2 Goodness-of-Fit.....	12
2.3.3 Yield Stress	14
2.3.4 Wellbore Shear Rates	15
2.3.5 Limiting the Quemada Parameters	17
3 Previous Work.....	19
4 Methodology	21
4.1 Materials.....	21

4.1.1	Oil Based Drilling Fluids	21
4.1.2	Water Based Drilling Fluids.....	22
4.2	Equipment and Experimental Procedure.....	22
4.2.1	Preparation and Treatment of the Drilling Fluids	22
4.2.2	Drilling Fluid Measurements	23
4.3	Implementing the Rheological Models	25
4.3.1	Fitting of the Herschel-Bulkley Model	25
4.3.2	Fitting of the Quemada Model	26
5	Results and Discussions	28
5.1	Laboratory Results and Fluid Rheology.....	28
5.1.1	Properties and Flow Behaviours	29
5.1.2	Temperature and Ageing Effects.....	31
5.2	Herschel-Bulkley Model	33
5.2.1	Flow Curves	33
5.2.2	Herschel-Bulkley Parameters	39
5.3	Quemada Model	41
5.3.1	Viscosity Curves	41
5.3.2	Curve Fitted Quemada Parameters.....	45
5.3.3	Calculated Quemada Parameters.....	48
5.3.4	Infinite- and Zero-Shear Viscosities	49
6	Conclusion.....	51
	References	53
	Appendix A – OFITE 900 Measurement Data.....	56
	Appendix B – Anton Paar MCR 302 Measurement Data	60
	Appendix C – Herschel-Bulkley Model Values.....	64
	Appendix D – Quemada Model Values	68

List of Figures

Figure 1. Two-Plates-Model (Mezger, 2006).....	3
Figure 2. Rotational principles: Couette (left) and Searle (right).....	4
Figure 3. Flow curves (left) and viscosity curves (right): (1) Newtonian fluid, (2) shear-thinning fluid, (3) shear-thickening fluid (Anton Paar, n.d.-a).	5
Figure 4. Log viscosity curve of shear-thinning fluids (Duffy, 2016).	6
Figure 5. Rheology models: (1) Bingham Plastic model, (2) Herschel-Bulkley model, (3) Newtonian model, and (4) Power Law model.	8
Figure 6. GRG nonlinear solver run (EngineerExcel, n.d.).....	12
Figure 7. Watson (2004) review article enactment. People in photo: Niall W.G. Young (left) and Mats Larsson (right). In agreement with the photographer: Tor Henry Omland (2004).	14
Figure 8. OBDF and WBDF: MCR 302 at 25°C (left) and OFITE at 21°C (right). ...	29
Figure 9. OFITE and MCR 302 measurements at 50°C after ageing: OBDF (left) and WBDF (right).	30
Figure 10. MCR 302: Temperature effects in OBDF for the entire shear rate range (right) and the very low shear rate range (left).....	31
Figure 11. MCR 302: Temperature effects in WBDF for the entire shear rate range (right) and the very low shear rate range (left).....	32
Figure 12. OBDF 25°C before and after ageing for the entire shear rate range (right) and the very low shear rate range (left).	32
Figure 13. WBDF 25°C before and after ageing for the entire shear rate range (right) and the very low shear rate range (left).	33
Figure 14. OBDF 1 at 25°C (pink) and 50 °C (green) before ageing including Herschel-Bulkley model (HBM) for low shear rates (LSRs) and high shear rates (HSRs).....	35
Figure 15. OBDF 2 at 25°C (pink) and 50 °C (green) before ageing including Herschel-Bulkley model (HBM) for low shear rates (LSRs) and high shear rates (HSRs).....	36
Figure 16. WBDF 3 at 25°C (pink) and 50 °C (green) before ageing including Herschel-Bulkley model (HBM) for low shear rates (LSRs) and high shear rates (HSRs).....	37
Figure 17. WBDF 4 at 25°C (pink) and 50 °C (green) before ageing including Herschel-Bulkley model (HBM) for low shear rates (LSRs) and high shear rates (HSRs).....	38
Figure 18. OBDF 1 at 25 and 50°C before ageing.	42
Figure 19. OBDF 2 at 25 and 50°C before ageing	42

Figure 20. WBDF 3 at 25 and 50°C before ageing.	43
Figure 21. WBDF 4 at 25 and 50°C before ageing.	43
Figure 22. OBDF 1 at 25°C, Herschel-Bulkley and Quemada model comparison.	44
Figure 23. OBDF 1 at 25°C before ageing, curve fitted using residual sum of squares (RSS) and weighted least square (WLS).	47
Figure 24. OBDF 1 at 25°C before ageing: Change in Quemada parameters when the shear rate range is shorter, including the difference between curve fitting with weighted least squares (WLS) and residual sum of squares (RSS).	50

List of Tables

Table 1. Approximate formulation of the OBDF at 20°C.	21
Table 2. Approximate formulation of the WBDF at 20°C.	22
Table 3. Mixing times for each component of the OBDFs and the WBDFs, *10 min. Heidolph + 15 min. Silverson.....	23
Table 4. OBDFs: Optimal Herschel-Bulkley model parameters and surplus shear stress at the different wall shear rates.....	40
Table 5. WBDFs: Optimal Herschel-Bulkley model parameters and surplus shear stress at the different wall shear rates.....	40
Table 6. OBDF: Optimal parameters of the Quemada model.	46
Table 7. WBDF: Optimal parameters of the Quemada model.	46
Table 8. OBDF: Calculated values of the Quemada model.....	49
Table 9. WBDF: Calculated values of the Quemada model.....	49
Table 11. OFITE 900 measurements of OBDF 1 at $21 \pm 1^\circ\text{C}$ before ageing, incl. gel-strength, APE, and MAPE. The values marked in “red” are the excluded 20 rpm readings.....	56
Table 12. OFITE 900 measurements of OBDF 1 at $21 \pm 1^\circ\text{C}$ after ageing, incl. gel-strength, APE, and MAPE. The values marked in “red” are the excluded 20 rpm readings.....	56
Table 13. OFITE 900 measurements of OBDF 1 at $50 \pm 3^\circ\text{C}$ after ageing, incl. gel-strength, APE, and MAPE. The values marked in “red” are the excluded 20 rpm readings.....	56
Table 14. OFITE 900 measurements of OBDF 2 at $21 \pm 1^\circ\text{C}$ before ageing, incl. gel-strength APE, and MAPE. The “red” values are the excluded 20 rpm readings.....	57
Table 15. OFITE 900 measurements of OBDF 2 at $21 \pm 1^\circ\text{C}$ after ageing, incl. gel-strength APE, and MAPE. The “red” values are the excluded 20 rpm readings.....	57
Table 16. OFITE 900 measurements of OBDF 2 at $50 \pm 1^\circ\text{C}$ after ageing, incl. gel-strength APE, and MAPE. The “red” values are the excluded 20 rpm readings.....	57
Table 17. OFITE 900 measurements of WBDF 3 at $21 \pm 1^\circ\text{C}$ before ageing, incl. gel-strength, APE and MAPE. The “red” values are the excluded 20 rpm readings.....	58
Table 18. OFITE 900 measurements of WBDF 3 at $21 \pm 1^\circ\text{C}$ after ageing, incl. gel-strength, APE and MAPE. The “red” values are the excluded 20 rpm readings.....	58

Table 19. OFITE 900 measurements of WBDF 3 at $50 \pm 3^\circ\text{C}$ after ageing, incl. gel-strength, APE and MAPE.....	58
Table 20. OFITE 900 measurements of WBDF 4 at $21 \pm 1^\circ\text{C}$ before ageing, incl. gel-strength, APE and MAPE. The “red” values are the excluded 20 rpm readings.....	59
Table 21. OFITE 900 measurements of WBDF 4 at $21 \pm 1^\circ\text{C}$ after ageing, incl. gel-strength, APE and MAPE. The “red” values are the excluded 20 rpm readings.....	59
Table 22. OFITE 900 measurements of WBDF 4 at $50 \pm 2^\circ\text{C}$ after ageing, incl. gel-strength, APE and MAPE. The “red” values are the excluded 20 rpm readings.....	59
Table 23. MCR 302 measurements of OBDF 1 including APE.....	60
Table 24. MCR 302 measurements of OBDF 2 including APE.....	61
Table 25. MCR 302 measurements of WBDF 3 including APE.....	62
Table 26. MCR 302 measurements of WBDF 4 including APE.....	63
Table 27. Measured and *Herschel-Bulkley model shear stress of OBDF 1.....	64
Table 28. Measured and *Herschel-Bulkley model shear stress of OBDF 2.....	65
Table 29. Measured and *Herschel-Bulkley model shear stress of WBDF 3.....	66
Table 30. Measured and *Herschel-Bulkley model shear stress of WBDF 4.....	67
Table 31. Measured and Quemada model viscosity of OBDF 1.....	68
Table 32. Measured and Quemada model viscosity of OBDF 2.....	69
Table 33. Measured and Quemada model viscosity of WBDF 3.....	70
Table 34. Measured and Quemada model viscosity of WBDF 4.....	71

1 Introduction

During a drilling operation, drilling fluid is pumped from the pits, through the drill string, where it exits the drill bit into annulus. When the drilling fluid enters the annular gap between the exposed formation and the bottom hole assembly (BHA), it collects the solid cuttings and transports them to the shale shakers. These devices separate the cuttings from the drilling fluid, before the fluid is prepared for recirculation (Willamson, 2013).

During the described process, the drilling fluid serves several important functions. This includes maintaining the wellbore stability by controlling the wellbore pressure, minimising hydraulic erosion, and controlling clays (Willamson, 2013). The pressure in the well, exerted by the weight of the drilling fluid column, must slightly exceed the pore pressure of the formations, to prevent inflow of formation fluids. By only slightly exceeding the pore pressure, the likelihood of exceeding the fracture pressure of the formation is minimised, evading well control issues related to loss of circulation. The hydraulic erosion is minimised by balancing hole-cleaning requirements, carrying capacity, and fluid velocity against hole geometry. The hole-cleaning efficiency and carrying capacity relies on the drilling fluid's rheological properties and behaviours. During circulation, low viscosity is desired to achieve an efficient rate of penetration (ROP) without excessive frictional forces. In addition, maintaining good carrying capacity upon circulation stops. Under these static conditions, the fluid should quickly form a sufficient gel-structure to keep cuttings and weighing material suspended. However, the gel-structure must be easily broken and returned to low-viscosity fluid when circulation restarts. A gauge hole can be cleaned by low-viscosity fluids with minimal problems, but in the event of an enlarged hole section, a different viscosity profile to ensure sufficient hole cleaning is required. Increasing the pump rate to sufficiently clean the enlarged hole section may lead to excessive fluid velocity in the gauge hole section. This results in different fluid velocities in the enlarged and gauge holes, i.e. the wellbore has a range of different shear rates. These conflicting rheological requirements are minimised by using shear-thinning drilling fluids.

Understanding the rheological properties and behaviours of drilling fluids is crucial to efficiently clean the wellbore and to maintain the hole stability. However, the flow behaviour is not always known for the entire range of relevant shear rates. Simulating rheological behaviour of drilling fluids, by means of available models is a necessity, but can sometimes be challenging due to changes in drilling parameters. Traditionally, the drilling industry uses simple models like Herschel-Bulkley model, but the accuracy of these models can be

questioned. Therefore, researching other viscosity models, to describe the viscous behaviour of drilling fluids with increased accuracy over a wide range of wall shear rates, is of interest.

In this thesis, the model of interest is the Quemada model, developed by Quemada in 1998. It is a more complex viscosity model compared to the previously mentioned Herschel-Bulkley model. Quemada (1998) declared that structural models are more suitable for complex fluids such as drilling fluids. The model describes a concept of shear-dependent structures, i.e. the construction and destruction of structural units (SUs) caused by shear forces. Thus, researching this model, regarding the shear-thinning behaviour of drilling fluids, is of interest. Previous work has been conducted on the Quemada model with regards to drilling and well fluid, i.e. cementitious materials (Hodne et al., 2007) and synthetic based fluids (SBF) (Baldino et al., 2018). This is further discussed in Chapter 3 in relation to the approach of this thesis.

1.1 Objective and Limitations

The main objective of this thesis is to analyse the use of the Quemada model for predicting the viscous behaviour of drilling fluids, where the Herschel-Bulkley model serves as a basis of comparison. This study is limited to four selected drilling fluids, where two are water-based drilling fluids (WBDFs) and two are oil-based drilling fluids (OBDFs).

The objective is accomplished by reviewing relevant literature, and by characterising the rheological properties, behaviours, and changes of the selected drilling fluids. Generally, the complexity of drilling fluids makes their rheological behaviours not well understood. Attempts have been made to characterise these behaviours through standard measurement data, governed by current American Petroleum Institute (API) standards (American Petroleum Institute, 2014, 2019), and through superior measurement data with a wider range of shear rates. Finally, the analysis of the selected models includes how the rheological change affects the model parameters. To induce changes in rheological properties, the drilling fluids are subjected to specific temperatures and dynamic ageing, to simulate different wellbore conditions.

2 Theory

This chapter is divided into three main topics containing information about concepts and findings that supports the work of this thesis. The first topic contains relevant information on fluid rheology. The next topic includes the different models and their use in predicting the drilling fluid's rheological behaviour. Lastly, the third topic outlines how to determine or limit the model parameters, and the approaches of curve fitting the models.

2.1 Rheology

Rheology is the science of deformation and flow of matter. By applying forces to the materials of interest, their rheological behaviour can be determined. This subchapter discusses the relationship between shear stress, shear rate, and shear viscosity. Additionally, the different principles of measuring these values are outlined, along with how the rheological behaviour can be interpreted through flow and viscosity curves.

2.1.1 Shear Stress, Shear Rate, and Shear Viscosity

In this study, the rheological parameters of interest are the shear stress, shear rate, and shear viscosity. To define these parameters, the Two-Plates-Model, described by Fig. 1, is utilised. This model describes how shear area A is moved by shear force F , thus moving the plate at velocity v , while the parallel plate, located at distance h , is kept stationary ($v = 0$). This model assumes laminar flow in the shear gap between the adjacent plates, where the fluid does not slip or glide along.

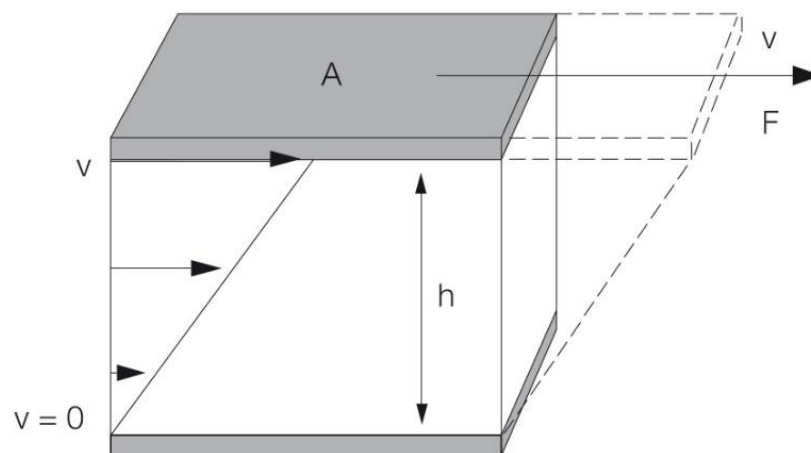


Figure 1. Two-Plates-Model (Mezger, 2006).

The flow conditions in a rheometer are not as simple as described by the Two-Plates-Model. Nonetheless, if the given conditions are met, and the shear gap is adequately narrow, the rheological parameters is defined as follows.

The shear rate, denoted by $\dot{\gamma}$, is defined as the rate of change in velocity when adjacent layers of fluid move at different velocities. Shear rate can be described as $\dot{\gamma} = \frac{v}{h}$, or by differential $\dot{\gamma} = \frac{dv}{dh}$, with unit [1/s]. The shear stress, denoted by τ , is defined by force F , which moves the upper layer, divided by the layer's surface area A , i.e. $\tau = \frac{F}{A}$ with unit [Pa]. By using the shear rate and shear stress, the shear viscosity η is defined as $\eta = \frac{\tau}{\dot{\gamma}}$ with unit [Pa·s] (Mezger, 2006). Viscosity is related to the internal friction of the fluid and shows its resistance to flow.

2.1.2 Rotational Principles

To obtain the flow and viscosity curves of the selected drilling fluids, and to characterise their rheological behaviour, rheometers or viscometers are used. These instruments measure the relationship between the shear rate and the corresponding shear stress and viscosity by using two different rotational principles, Couette and Searle (Fig. 2). OFITE Model 900 Viscometer and Anton Paar MCR 302 Rheometer are the two instruments used to obtain the flow curves in this study.

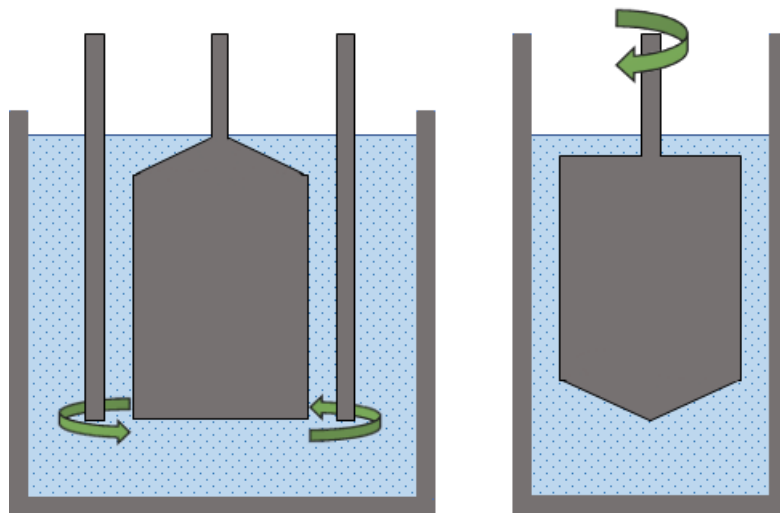


Figure 2. Rotational principles: Couette (left) and Searle (right).

The OFITE Model 900 Viscometer is a coaxial cylinder rotational viscometer based on the Couette principle. The fluid is sheared in the annular space between the cylinder and the bob during measurements. When the cylinder rotates at a measured angular velocity, the fluid exerts a viscous drag on the bob. To overcome the viscous drag, the bob is held fixed by creating

a torque, which is deflected by a spring. The viscometer is then able to measure the angular displacement of the bob. The OFITE 900 uses calculations to display output data based on the shear rate and displacement of the bob (Gucuyener, Kok, & Batmaz, 2002; OFITE, 2015; Skadsem & Saasen, 2019). This technology minimises unstable flow in low viscosity fluid samples and is the most used among the oilfield viscometers (Mezger, 2006). Nonetheless, there have been studies conducted showing the inaccuracy of concentric cylinder Couette geometry at low shear rates (LSRs). In a study conducted by Skadsem and Saasen (2019), they look at how shear-thinning yield stress fluids yield at LSRs, and how the Newtonian shear rate assumptions causes errors when measuring these fluids. Skadsem and Saasen (2019) show how decreasing shear rates, in a standard oilfield viscometer (Fann 35), increases the deviation between the assumed Newtonian wall shear rates and the actual wall shear rates. This effect depends on the size of the shear gap, where narrower shear gaps are shown to be better.

The Anton Paar MCR 302, with a concentric cylinder system, uses the Searle principle. The measuring bob rotates in the sample filled cup, i.e. the outer cylinder. For the motor to drive the inner bob at a given speed, it needs to exceed the viscous forces of the fluid. Thus, the necessary torque is a measure of the viscosity (Anton Paar, n.d.-b). The downside of this measuring system is the potential occurrence of unstable flow in low-viscosity fluids at high shear rates (HSRs) (Mezger, 2006).

2.1.3 Flow and Viscosity Curves

Flow and viscosity curves are graphical representations of a fluids change in rheological behaviour when shear forces are applied. Plotting the obtained shear stress or viscosity against shear rate characterises the fluid behaviour and make them possible to interpret.

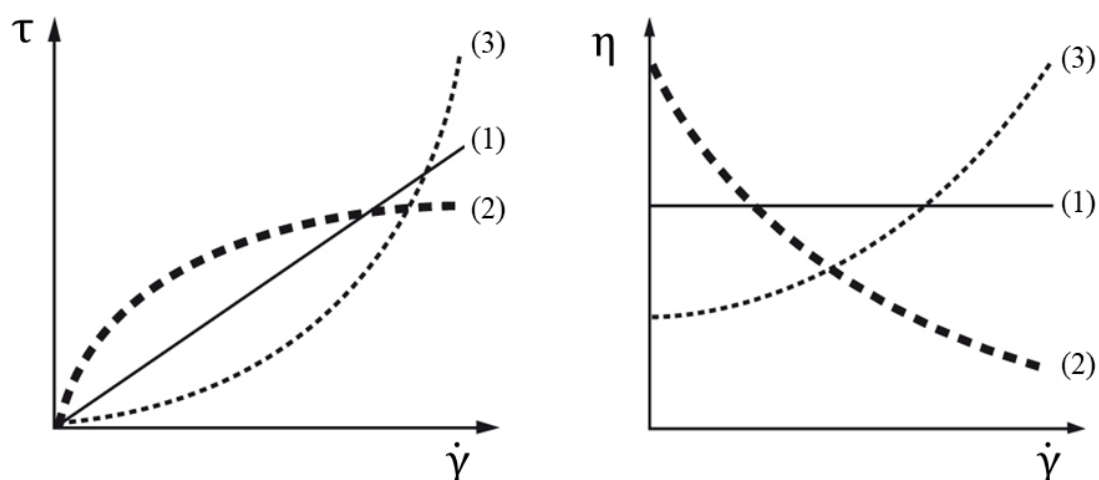


Figure 3. Flow curves (left) and viscosity curves (right): (1) Newtonian fluid, (2) shear-thinning fluid, (3) shear-thickening fluid (Anton Paar, n.d.-a).

The three main rheological behaviours are illustrated in Fig. 3 in terms of shear stress and viscosity against shear rate. The figure does not perfectly represent all fluid behaviours but describes the general curve shapes. As explained in the introduction, shear-thinning drilling fluid minimises the conflicting rheological requirements caused by wellbore conditions and differences in wall shear rates. Thus, the scope of this study only includes shear-thinning behaviour.

The viscosity curves can also be interpreted at logarithmic scales to understand a larger range of viscosity data. Fig. 4 displays two different types of shear-thinning fluids, one with apparent yield stress and one without yield stress. The existence of yield stress is discussed in Chapter 2.3.3. The blue curve has a plateau at LSRs, indicating the zero-shear viscosity, and one at HSRs, indicating the infinite-shear viscosity. The two plateaus are also referred to as the first and second Newtonian plateau, due to their constant viscosity. When the fluid exhibits Newtonian behaviour (Fig. 3 curve (1)) at LSRs the fluid has no yield stress. On the other hand, the green curve shows no zero-shear plateau. This may be explained by the zero-shear plateau existing outside the area of possible measurements and is thus described by an apparent yield stress (Barnes, Hutton, & Walters, 1989). Fig. 4 also illustrates how the limited shear rate range of a typical viscometer can be unable to reveal the zero-shear plateau.

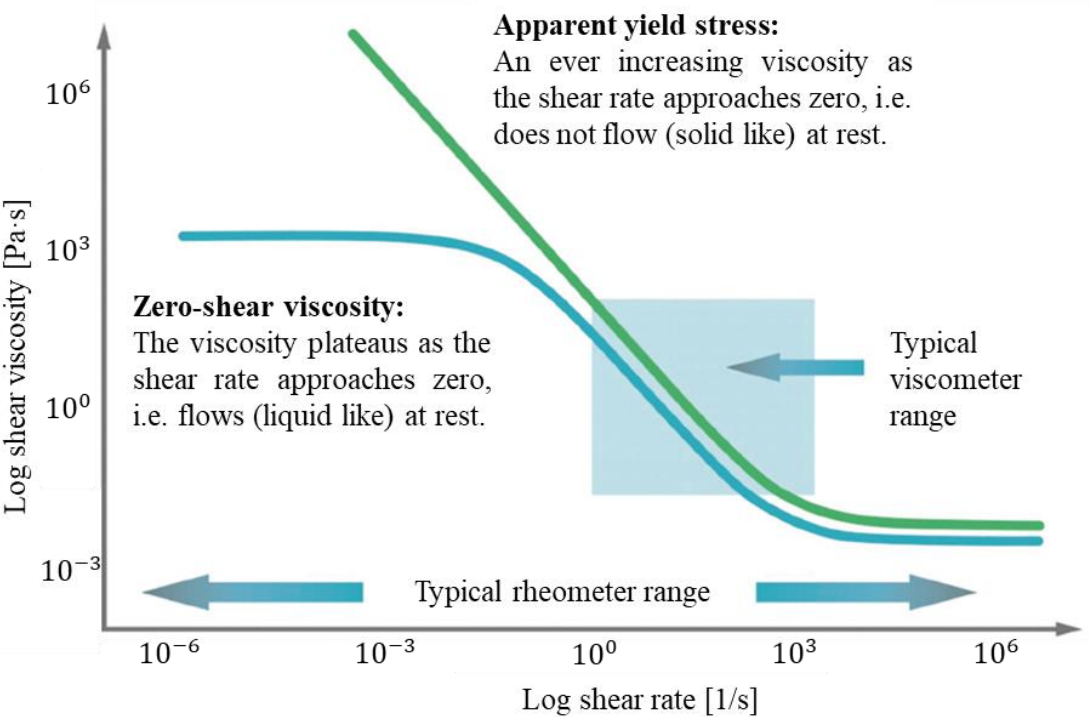


Figure 4. Log viscosity curve of shear-thinning fluids (Duffy, 2016).

2.1.4 Effects of Temperature and Ageing on Drilling Fluid Rheology

The temperature is an important factor when characterising drilling fluid properties and behaviours. Measuring the fluid at different temperatures give insight into the rheological behavioural changes in the wellbore. These temperature changes can affect rheological properties physically, chemically, or electrochemically (Caenn, Darley, & Gray, 2017). How the rheology changes with differing temperatures depends on its composition. Even small variations in the concentration of the fluid components can affect the behaviour of the fluid (Bartlett, 1967), making it difficult to determine which fluid components are more affected by the changes in temperature.

A study was conducted on OBDFs by Halvorsen et al. (2019), where the selected fluids were exposed to a temperature range of 20-70°C with increments of 10°C. Their results show the change in shear stress decreases with each increment. Other studies conducted on bentonite-WBDFs show similar behaviour as on OBDFs (Anawe & Folyan, 2018; Teymoori & Alaskari, 2007). This study has WBDFs containing polymers. In general, the viscosity's rate of change in polymer solutions depend on different factors such as temperature, salinity, polymer concentration, and molecular weight (Ghasem & Al-Marzouqi, 2011; Nouri & Root, 1971).

Another important area of study is the rheological changes caused by ageing drilling fluids. In the field, the fluid is circulated through the wellbore, and reused multiple times. Thus, simulating this process and study how the fluid will react to higher temperature exposure over time is essential to ensure the drilling fluids ability to handle the well conditions and to ensure correct usage of additives and chemicals.

2.2 Rheology Models

Over the years, several mathematical models to describe the experimental data of drilling fluids, have been developed. These models are used to predict the shear-dependent rheological behaviour of the drilling fluid outside the measured interval by characterising its flow properties (Andaverde, Wong-Loya, Vargas-Tabares, & Robles, 2019; Hodne et al., 2007). Some of the most recognised models for describing the rheological behaviour of drilling fluids are the Bingham Plastic, Power Law, and Herschel-Bulkley model (Fig. 5).

The Newtonian (Fig. 5 curve (3)) and Bingham Plastic (Fig. 5 curve (1)) models are widely used linear models. These models are very comparable, the only difference being the existence of yield stress. The Bingham Plastic model is defined as $\tau = \tau_0 + \mu_p \dot{\gamma}$ when $\tau > \tau_0$ and becomes the Newtonian model $\tau = \mu_p \dot{\gamma}$ when $\tau_0 = 0$. The shear stress (τ) is defined by

the plastic viscosity (μ_p) which is independent of shear rate ($\dot{\gamma}$) and the initial yield stress (τ_0) (Andaverde et al., 2019). However, these models cannot describe the non-linearity of shear-thinning behaviour, making them inaccurate models for drilling fluids (Gucuyener, 1983).

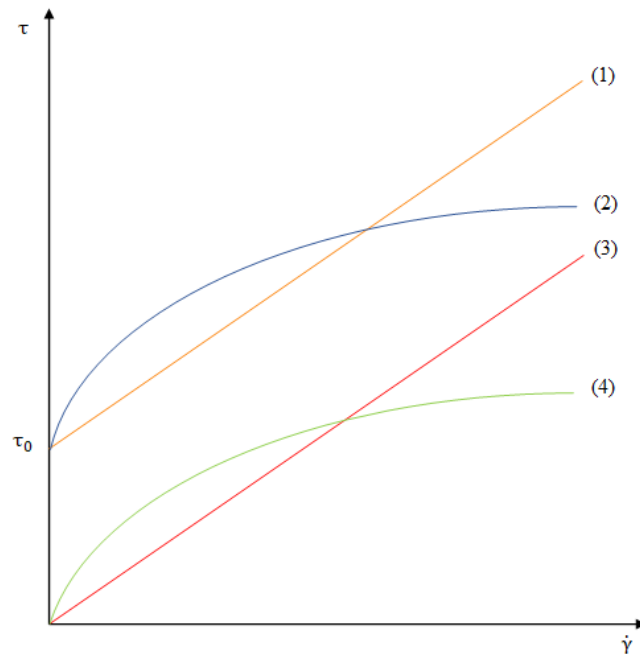


Figure 5. Rheology models: (1) Bingham Plastic model, (2) Herschel-Bulkley model, (3) Newtonian model, and (4) Power Law model.

The Power Law (Fig. 5 curve (4)) model is a non-linear model not accounting for yield stress. It describes the non-Newtonian behaviour of a fluid and is defined by $\tau = k\dot{\gamma}^n$. The shear stress (τ) depends on the shear rate ($\dot{\gamma}$), as well as the consistency index k , and flow behaviour index n . However, because this model does not include yield stress, it is inaccurate in describing the rheological behaviour of some drilling fluids (Andaverde et al., 2019; Gucuyener, 1983). On the other hand, the Herschel-Bulkley model (Fig. 5 curve (2)) is considered a combination of Bingham plastic and Power Law, by including the yield stress and the non-Newtonian behaviour of drilling fluids. This makes the Herschel-Bulkley model a common model in the drilling industry, and it therefore serves as a basis of comparison with the Quemada model in this thesis. For this purpose, the Herschel-Bulkley model and the Quemada model is explained in-depth in the two following subchapters.

2.2.1 Herschel-Bulkley Model

The Herschel-Bulkley model (Herschel & Bulkley, 1926) is a non-linear, three-parameter model. This is the simplest model used to describe the flow behaviour of drilling fluids with reasonable accuracy (Saasen & Ytrehus, 2018). It is defined as:

$$\tau = \tau_0 + k\dot{\gamma}^n \quad \text{when} \quad \tau > \tau_0 \quad (1)$$

where the shear stress (τ) depends on the yield stress (τ_0), shear rate ($\dot{\gamma}$), and the consistency and flow behaviour indices, k and n respectively (Skadsem, Leulseged, & Cayeux, 2019). The k - and n -parameters are the empirical curve fitting parameters (Chhabra & Richardson, 2008). The n -parameter determines the rheological behaviour of the fluids. As stated in Chapter 2.1.3, shear thinning is the rheological behaviour of interest, which is characterised by the flow behaviour index in the range of $0 < n < 1$. The closer n is to zero, the more shear-thinning behaviour the fluid has. The yield stress can be approximated through different methods as explained in Chapter 2.3.3.

The Herschel-Bulkley model has a few limitations. The fitted values of k and n depend on the applied range of shear rates, and the model does not take the zero- and infinite-shear viscosities into account. Furthermore, the k -parameter is dependent on the dimensionless n (Chhabra & Richardson, 2008). Due to this dependency, the k -parameter cannot be used as a comparison between differently modelled flow curves and is of little practical use.

To circumvent the problem of comparing the k -parameter, Saasen and Ytrehus (2018) rewrote the Herschel-Bulkley model, Eq. (1), by using the dimensionless shear rate to include comparable independent parameters, and defined it as:

$$\tau = \tau_0 + \tau_s \left(\frac{\dot{\gamma}}{\dot{\gamma}_s} \right)^n \quad \text{when} \quad \tau > \tau_0 \quad (2)$$

This model is based on Nelson's and Ewoldt's (2017) model, which is extended further to be used on drilling fluids, where the surplus shear stress, $\tau_s = \tau - \tau_0$, is given at a characteristic shear rate $\dot{\gamma}_s$. Unlike k , these parameters do not depend on any of the other parameters. Therefore, they can be used as a comparison between different fluids when planning to drill a well section. If the model-parameters have been optimised through curve fitting for the shear rate range of interest, some of the uncertainties will be reduced. Thus, the surplus shear stress can easily be determined from Eq. (3) through the optimised k and n parameters (Saasen & Ytrehus, 2018).

$$\tau_s = k\dot{\gamma}_s^n \quad (3)$$

2.2.2 Quemada Model

The Quemada model, developed by Quemada (1998), is an extension of the hard-sphere model and a revisited concept of the effective volume fraction (EVF). This extension includes complex fluids under the assumption they are monodisperse dispersions of approximately spherical structural units (SUs). The Quemada model describes how the viscosity is affected by the construction and destruction of shear-dependent SUs suspended in the fluid. When the fluid is prepared, it may form aggregated flocs of the initial fluid particles, called individual flocs (IFs). At low shear rates (LSRs), the inter-particle forces result in the formation of SUs from the initial fluid particles and/or the IFs. When, SUs are formed, they lock up some of the suspending fluid, increasing the EVF of the particles, resulting in increased viscosity. When the shear rate increases, these SUs break apart, subsequently releasing the locked-up fluid, decreasing the EVF, and reducing the viscosity (Quemada, 1998; Hodne et al., 2007). Quemada (1998) used this concept to define the following viscosity equation:

$$\eta = \eta_{\infty} \left[\frac{1 + \Gamma^p}{\chi + \Gamma^p} \right]^2 \quad (4)$$

In Eq. (4), η_{∞} is the steady state infinite-shear viscosity, where the dimensionless shear variable $\Gamma \rightarrow \infty$. This variable can be expressed in terms of shear rate or shear stress, $\Gamma = (\dot{\gamma}/\dot{\gamma}_c)$ or (τ/τ_c) , depending on the viscometer used in the measurements (Quemada, 1998). The exponent of the dimensionless shear variable, p , has been pre-defined by Quemada (1998) to be $0 < p < 1$, and has been found to usually be close to 0.5 in colloidal dispersions (van der Werff & de Kruif, 1989).

The model is dependent on its structural index (χ), defined as:

$$\chi(\phi) = \frac{1 - \phi/\phi_0}{1 - \phi/\phi_{\infty}} \equiv \pm \left(\frac{\eta_{\infty}}{\eta_0} \right)^{\frac{1}{2}} \quad (5)$$

which works as a rheological index by describing the rheological behaviour of the fluid. For shear-thinning drilling fluids, the structural index is limited to $0 < \chi < 1$. It can be expressed by the limiting zero- and infinite-shear viscosities where $\Gamma \rightarrow 0$ and $\Gamma \rightarrow \infty$:

$$\eta_0 = \eta_F \left(1 - \frac{\phi}{\phi_0} \right)^{-2} \quad \text{and} \quad \eta_{\infty} = \eta_F \left(1 - \frac{\phi}{\phi_{\infty}} \right)^{-2} \quad (6)$$

Each limiting viscosity depend on their respective limiting maximum-packing fraction defined as:

$$\phi_0 = \frac{\phi_m}{1 + CS_0} \quad \text{and} \quad \phi_{\infty} = \frac{\phi_m}{1 + CS_{\infty}} \quad (7)$$

These parameters depend on the maximum packing fraction ϕ_m , the compactness factor $C = \varphi^{-1} - 1$ where φ is the SU's mean compactness, and the limiting values of the structure variable. The structure variables are defined as $S_0 = \phi_{A0}/\phi$ and $S_\infty = \phi_{A\infty}/\phi$ when $\Gamma \rightarrow 0$ and $\Gamma \rightarrow \infty$ respectively, where Quemada (1998) describes ϕ_A as the volume fraction of particles in the SUs. For pseudo-plastic behaviour, Quemada (1998) confines the limiting maximum packing fractions to $\phi < \phi_0 < \phi_\infty$ and the limiting aggregated volume fractions to $\phi \geq \phi_{A0} \geq \phi_{A\infty}$.

The structure variable S is also defined as:

$$\frac{dS}{dt} = \kappa_A(S_0 - S) - \kappa_D(S - S_\infty) \quad (8)$$

where κ_A and κ_D are shear-dependent constants of construction and destruction of SUs. When $dS/dt = 0$, the equation gives the steady state solution:

$$S_{eq} = \frac{S_0 + S_\infty \theta}{1 + \theta} \quad (9)$$

where Quemada (1998) assumes θ to be:

$$\theta(\dot{\gamma}) = \frac{\kappa_D}{\kappa_A} = \frac{t_A}{t_D} = (t_c \dot{\gamma})^p = \Gamma^p \quad (10)$$

in concentrated systems. The characteristic time t_c is required for dimensional homogeneity and it needs to be closely related to one of the relaxation times, t_A and/or t_D (Hodne et al., 2007; Quemada, 1998).

Some of the parameters ($t_c, \eta_0, \eta_\infty, \phi$, and ϕ_m) can be determined by different methods and needs to be limited with care. This will be explained further in Chapter 2.3.5.

2.3 Model Application

2.3.1 Nonlinear Regression

The main objective of nonlinear regression (NLR) is to find the “best fit” of the model through optimising its goodness-of-fit (see Chapter 2.3.2). NLR is a very flexible method for curve fitting. Multiple software programs have an add-in/built-in function that makes NLR possible when fitting a model to experimental data. Microsoft Excel Solver is an add-in program where NLR is a possibility for curve fitting. Excel's standard solver uses the Generalised Reduced Gradient (GRG) method, which is based on Lasdon et al.'s (1978) nonlinear optimised GRG, also called GRG2 (Fylstra et al., 1998; Lasdon et al., 1978). This method looks at the

gradient of the model as the curve-fitting parameters change to create a better fit. It reaches the optimum solution when the partial derivatives equal zero (EngineerExcel, n.d.).

The problem with this method is that it may find a local optimum solution, closest to the initial conditions, instead of the global optimum solution, as illustrated in Fig. 6. Another necessity when utilising this algorithm is for the function to be smooth without any discontinuities (EngineerExcel, n.d.; FrontlineSolvers, n.d.). However, a local minimum will rarely be encountered if the measured data has little scatter, is over an appropriate range of X-values (range of shear rates in this case), has an appropriate model, and has sensible initial values (Motulsky & Christopoulos, 2003). Nonetheless, the Excel Solver has a multistart function to circumvent the problem of the local and global optimisation. This function chooses random starting points, within given limitations, to find the best global solution. By having well defined variable boundaries and longer solver runs, the likelihood of finding the global optimisation is higher (EngineerExcel, n.d.; FrontlineSolvers, n.d.).

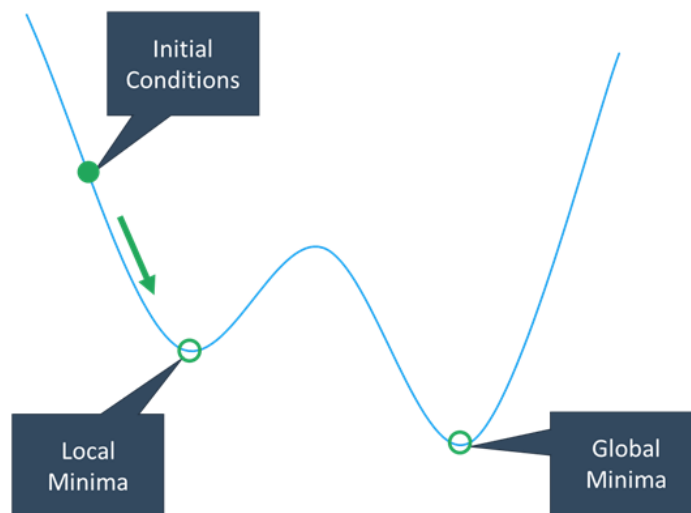


Figure 6. GRG nonlinear solver run (EngineerExcel, n.d.).

2.3.2 Goodness-of-Fit

Goodness-of-fit is a statistical model that describes the relation between expected and observed data. In this case, referring to the expected data of the selected models and the measured data obtained by the rheometer and viscometer. A well know measure of goodness-of-fit is the correlation coefficient, R^2 . In a regression model, R^2 measures the linear relationship by how much variance in the dependent variables are caused by the independent variables.

However, studies have been shown that this correlation is only valid for linear regression and should not be trusted in NLR (Spiess & Neumeyer, 2010).

A common way to reduce the deviation between observed data and the applied model, is least square regression. By reducing the residual sum of squares (RSS), also called sum of squared error, the vertical distances between the empirical and predicted values are reduced. RSS is generally defined as:

$$RSS = \sum_i^{N_p} (y_i - \hat{y}_i)^2 \quad (11)$$

where the y_i represent the measured value, \hat{y}_i the predicted value decided by the model, and N_p the number of measurement points (Motulsky & Christopoulos, 2003; NIST/SEMATECH, 2012).

Sometimes experimental data range from very low to very high values. The goodness-of-fit will mostly be influenced by the high y_i values, because the residual squares are consequently larger. If this is undesirable, weights can be applied to even out the influence of the high value data points and the low value data points, thus reducing the sum of the weighted squares between the experimental data and the model curve. This is the weighted least square (WLS) method and it is defined as:

$$WLS = \sum_i^{N_p} w_i (y_i - \hat{y}_i)^2 \quad \text{where} \quad w_i = \frac{1}{y_i} \text{ or } \frac{1}{y_i^2} \quad (12)$$

where y_i , \hat{y}_i , and N_p represent the same as in Eq. (11), and the weight w_i , in Eq. 12, shows two common weighing methods.

When $w_i = 1$ no weights are added and WLS equals RSS. However, reducing the relative distance, given when $w_i = 1/y_i^2$, will over-proportionate the weight of smaller values and result in the model not being as good at LSRs. Therefore, a compromise between the two, where $w_i = 1/y_i$, can be used. (Motulsky & Christopoulos, 2003; Thermo Scientific, 2005).

The RSS and WLS quantifies the goodness-of-fit but can only be used when there is a basis of comparison (Motulsky & Christopoulos, 2003). The lowest WLS/RSS-values describe the model with the “best fit”. However, this method is not very intuitive, high observed values yields higher RSS/WLS compared to low observed values. To supplement the RSS and WLS, the absolute and mean absolute percentage errors (APEs and MAPEs) can be used. They represent the normal and average absolute percentage differences between the measured and

the model values. They may, however, be unpredictable when applied to data of low values and do not work where the measured value is zero.

When the regression methods of the nonlinear regression have been decided, limiting and determining the model parameters are the next steps in obtaining accurate models.

2.3.3 Yield Stress

The yield stress is a parameter in the Herschel-Bulkley model. It is considered a physical fluid property and can be determined through other methods than curve fitting. However, the existence and definition of yield stress, along with how to approximate it, must be discussed further.

Reviewing yield stress related studies can be very complicated. There is a controversy around how it should be defined, how it should be measured (directly or indirectly), and whether yield stress even exists. This problem has been summarised in an interesting review article written by Niall W. G. Young and Mads Larsson, attributed Watson (2004), and were enacted as a play by the same people (Fig. 7). Yield stress is commonly defined as a mark between the solid- and liquid-like behaviour of the fluid. If shear stress is applied below the yield stress, the fluid will exhibit a solid-like behaviour and when the yield stress is exceeded, it behaves like a liquid (Duffy, 2012). However, this does not necessarily mean that the fluid structure is completely destroyed when the applied stress equals the yield stress. According to Balmforth et al. (2014), fluid structures typically exist after the fluid has yielded, making the viscosity shear-rate dependent.



Figure 7. Watson (2004) review article enactment. People in photo: Niall W.G. Young (left) and Mats Larsson (right). In agreement with the photographer: Tor Henry Omland (2004).

Blair (1933) defined yield stress as “the critical shear stress below which no flow can be observed under the condition of experimentation”. On the other hand, Barnes and Walters (1985) would say true yield stress do not exist and defines what cannot be measured. They came to this conclusion due to the newly developed stress instruments that were able to measure at shear rates as low as 10^{-6} s^{-1} .

Assuming yield stress exists, it can be approximated through direct and indirect measurements. The indirect method uses the shear stress data at low shear rates (LSRs) to extrapolate a value at zero shear rate. However, this method can be very inaccurate. The LSR data may be inaccurate due to slippage, or the shear stress is simply measured at too HSRs. (Watson, 2004). One direct method for determining yield stress is the vane method. It will measure the yield stress as a physical property of the fluid. As the vane rotates, it stretches the network bond between the particles and aggregates, eventually breaking the bonds. When the majority of these bonds have been broken, the fluid has yielded (Dzuy & Boger, 1983). Barnes and Carnali (1990) conducted a numerical analysis on vane geometry and showed that no yield stress existed. They claimed that a thixotropic layer, forming at the vane surface, lead to apparent slip. When removing this, they produced viscosity curves with zero-shear plateau indications and thus showed the non-existence of true yield stress.

The review article by Watson (2004) concludes that the language used and the definitions of the of the measurement parameters are the most important when studying yield stress related cases.

2.3.4 Wellbore Shear Rates

Drilling fluids have a very complex rheological behaviour. The standard models like Herschel-Bulkley is rarely capable of representing a wide range of shear rates, e.g. $0-1020 \text{ s}^{-1}$, with high accuracy. Therefore, it is necessary to fit the model to a limited shear rate range, depending on the wall shear rates of the relevant hole-sections.

Assuming laminar flow in a pipe or in a narrow concentric annulus, where the annular gap is assumed to be adequately small compared to the wellbore, Eq. (13) to (17) can be derived (Guillot, 1990). These equations calculate the wall shear rates of non-Newtonian and Newtonian fluids and are found in textbooks, e.g. Nelson (1990). The wall shear rate, Eq. (13), is the maximum shea rate value, and depends on the non-Newtonian behaviour of the fluid that is described by n' . The problem with the wall shear rate is the shear stress at the wall, Eq. (15).

It depends on the often unknown friction pressure (E. B. Nelson, 1990), making the wall shear rates difficult to define for non-Newtonian fluids.

	<u>Pipe flow:</u>	<u>Annular flow:</u>
Wall shear rates	$\dot{\gamma}_W = \frac{3n' + 1}{4n'} \dot{\gamma}_{NW}$	$\dot{\gamma}_W = \frac{2n' + 1}{3n'} \dot{\gamma}_{NW}$ (13)
where	$n' = \frac{d \log (\tau_w)}{d \log (\dot{\gamma}_{NW})}$	$n' = \frac{d \log (\tau_w)}{d \log (\dot{\gamma}_{NW})}$ (14)
and	$\tau_w = \frac{D}{4} \frac{dp}{dz}$	$\tau_w = \frac{(D_o - D_i)}{4} \frac{dp}{dz}$ (15)

For shear-thinning fluids ($n' < 1$), such as most drilling fluids, the Newtonian wall shear rate is the lower boundary of the wall shear rate, and is given by:

	<u>Pipe flow:</u>	<u>Annular flow:</u>
Newtonian wall shear rates	$\dot{\gamma}_{NW} = \frac{8\bar{v}}{D}$	$\dot{\gamma}_{NW} = \frac{12\bar{v}}{D_o - D_i}$ (16)
Average velocity	$\bar{v} = \frac{Q}{A} = \frac{4Q}{\pi D^2}$	$\bar{v} = \frac{Q}{A} = \frac{4Q}{\pi(D_o^2 - D_i^2)}$ (17)

The Newtonian wall shear rates, Eq. (16), is defined by the volumetric flow rate of the mud pump and the size of the pipe or annular gap.

The geometry of a wellbore can vary greatly depending on the position of the drill string in the well. These variations in the wellbore geometry can cause large variations in the true wall shear rates, even more so than the non-Newtonian behaviour of the drilling fluids (E. B. Nelson, 1990). However, this study will assume a gauge hole with the drill string in the centre in all hole-sections, due to unknown wellbore geometry. This study uses the wall shear rates from the Newtonian wall shear rate equations, due to the unknown conditions of the well. For

the purposes of this study, the Newtonian wall shear rates provide a sufficiently good approximation.

When the relevant wall shear rates have been determined for different hole-sections, one model for HSR in the pipe and one model for LSRs in annulus can be fitted with Herschel-Bulkley. By fitting two models for each of their relevant shear rate range, the accuracy of the model will increase and yield better shear stress estimates. The focus will be the wall shear rates of the annular gap due to the pore and fracture pressures of the exposed formations in a well.

2.3.5 Limiting the Quemada Parameters

The Quemada model is a complex model with several parameters requiring a fitting process to find the optimal solution for modelling the fluids viscous behaviours. When fitting the Quemada model to the experimental data, these parameters must be defined by upper and lower boundaries through accurate sample preparation and measurements.

The characteristic time is defined by the characteristic shear rate ($t_c = \dot{\gamma}_c^{-1}$). Hodne et al. (2007) recognised the characteristic time t_c , as defined by Quemada (1998) to be the time needed for obtaining a suspension of almost mono-disperse SUs. The characteristic shear rate, compared to the shear rate range applied by the viscometer, describe the rheological behaviour of the selected fluids. Pseudo-plastic behaviour requires a characteristic shear rate within the range of applied shear rates (Quemada, 1978). Furthermore, the characteristic time can be given by $t_c \approx \eta_{eff} a^3 / W_I$ (Baldino et al., 2018; Quemada, 1998), where t_c depends on the effective viscosity η_{eff} , particle radius a , and particle interaction energy W_I . This equation explains how the characteristic time will decrease with increased temperature, due to the increase in W_I and decrease in η_{eff} (Baldino et al., 2018).

Infinite- and zero-shear viscosity was described from the viscosity curve in Fig. 4 (Chapter 2.1.3). These parameters can be estimated indirectly through curve fitting, directly measured, or be estimated through the volume fraction parameters described by Quemada (1998). However, attempts to directly measure these values are not always possible due to the limitation on the measuring equipment (Baldino et al., 2018). When using the method of determining the infinite- and zero-shear viscosity by Eq. (6) and Eq. (7) in Chapter 2.2.2, limiting the boundaries and estimating values of the parameters in the equations are crucial when fitting the model.

The solid volume fraction ϕ is an important factor of the viscous behaviour. It is a measure of the fraction of particles suspended in a fluid compared to the total volume of the

suspension. It is important to define it by the volume, and not the weight, due to the rheology's dependence on the forces acting on the particle surface and not on the particle's density. The viscosity is heavily dependent on the ϕ . Increasing the concentration of particles results in increased flow resistance, due to the particles being in each other's way, i.e. increased internal friction (Barnes et al., 1989). This volume fraction can be estimated from the weight of the materials used in the selected drilling fluids and the known/measured material/suspension densities, yielding equation:

$$\phi = \frac{V_{Suspended\ particles}}{V_{Total}} = \frac{V_{Total} - V_{Suspending\ fluid}}{V_{Total}} \quad (18)$$

The maximum packing fraction ϕ_m is defined as the solid volume fraction needed for flow to stop i.e. infinite viscosity. This happens when a solid structure, continuous throughout the suspension, is formed by the dispersed particles (Barnes et al., 1989; De Visscher & Vanelstraete, 2004). The ϕ_m of a suspension depends on several factors. One factor is the particle shape, where spherical particles having better space-filling properties than non-spherical particles. Another is the particle size distribution, where large distribution of particle sizes in a dispersion lead to the pores between the larger particles being filled by smaller particles. Lastly, including the arrangement of packing, where monodisperse spheres range from simple cubic ($\phi_m = 0.52$) to hexagonal close packed ($\phi_m = 0.74$) (Barnes et al., 1989).

3 Previous Work

The structural model proposed by Quemada (1998) is not normally used for modelling drilling and well fluids. The oil industry prefers simple models like Bingham, Power Law, and Herschel-Bulkley. However, there has been conducted some studies on the Quemada model in relation to drilling and well fluids.

Hodne et al. (2007) used this model for cementitious materials to predict the rheological behaviour of the fluid outside the range of measurement. The method utilised by Hodne et al. (2007), consisted of viscosity measurements and a thorough sample preparation to measure the particle packing fractions and the solid volume fractions. These measurements were necessary to limit the upper and lower boundaries of the six parameters used in the curve fitting, $p, t_c, \phi, \phi_m, \phi_{A0}, \phi_{A\infty}$.

The exponent p was limited to $0 < p < 1$ according to Quemada (1998). The applied range of shear rates were $0.05-511 \text{ s}^{-1}$. However, the characteristic time ($t_c = \dot{\gamma}^{-1}$) was limited to the shear rate range of $3.1-511 \text{ s}^{-1}$. Cementitious mixtures often contain air, resulting in air bubbles acting as particles, increasing the solid volume fraction, and affecting the experiment. Therefore, the limits of the solid volume fraction ϕ depended on the measured air content of the samples. For the maximum packing fraction ϕ_m , Hodne et al. (2007) were able to determine the lower limit packing fractions through a packing experiment. The maximum packing fraction for face centred packing of mono-disperse spheres, at 0.74 (Barnes et al., 1989), were set as the upper limit. The last two parameters, the limiting aggregated volume fractions, were limited to $\phi_{A\infty} \leq \phi_{A0} \leq \phi$ according to Quemada (1998) (Hodne et al., 2007).

Hodne et al. (2007) found two optimal solutions for each of their samples, where one was optimal for high shear rates (HSRs) and the other for low shear rates (LSRs). The two different curves showed two different behaviours, denoted by J- and S-curve. The J-curve only indicates the existence for infinite-shear viscosity and fits the LSR data. While the S-curve indicates both the zero- and infinite-shear viscosity and fits the HSR data. Hodne et al. (2007) concluded that the Quemada model (Quemada, 1998) could be used to predict the rheological behaviour of the cementitious materials. However, care had to be taken when choosing a solution to study a phenomenon at HSRs or LSRs.

Baldino et al. (2018) used a different method to fit the model to describe the behaviour of a synthetic based drilling fluid (SBF). Instead of looking at the volume fractions of the fluid, they tried to measure the infinite-shear viscosity (η_{∞}) and the zero-shear viscosity (η_0) by using the stress-over-shoot (SOT) testing technique. They met on technical limitations when

evaluating the zero-shear viscosity and were expecting a larger value. To correct for this, they introduced the correction parameter α into the model and defined the viscosity by:

$$\eta = \eta_{\infty} \left[\frac{1 + \Gamma^p}{(\eta_{\infty}/\alpha\eta_0)^{0.5} + \Gamma^p} \right]^2 \quad (19)$$

The only parameters requiring fitting were t_c , α , and p . The correction parameter α had to be greater than 1 to give a larger value of η_0 (Baldino et al., 2018), and the exponent p was treated the same as Quemada (1998) and Hodne et al. (2007). Unlike Hodne et al. (2007), they used the applied range of shear rates, $0.15 \text{ s}^{-1} \leq \dot{\gamma} \leq 1000 \text{ s}^{-1}$, to define the limits of the characteristic time.

The method applied by Baldino et al. (2018) resulted in a J-curve accurately describing the rheological behaviour at LSRs. However, like Hodne et al. (2007), the resulting J-curves introduced large discrepancies between the model and measured values at HSRs.

This thesis presents another modelling approach compared to Hodne et al. (2007) and Baldino et al. (2018). Instead of trying to limit the limiting viscosities, though the volume fraction like Hodne et al. (2007) or trying to measure the limiting viscosities like Baldino et al. (2018), the limiting viscosities were treated as empirical curve fitting parameters. The resulting optimal fit and the calculated solid volume fraction were then used to calculate the structural index and the limiting maximum volume fractions. These values were used to verify the rheological behaviour of the selected drilling fluids. Further explanation of this approach to the Quemada model can be found in Chapter 4.3.2.

4 Methodology

Four different drilling fluid recipes, both oil and water based, were prepared in the lab. Two comparable batches of each recipe were made to ensure the integrity of the experiment and to reduce the uncertainties one fluid sample would present, i.e. a total of eight samples were prepared and measured. Sample preparation, equipment, and method for measuring is presented in chapters 3.1 and 3.2, followed by model implantation methods in chapter 3.3.

4.1 Materials

4.1.1 Oil Based Drilling Fluids

The OBDFs made in the lab were field applicable fluids. Both recipes are tabulated in Tab. 1, presenting the quantity of components used in the fluids, along with some important fluid properties.

Properties	Recipe 1	Recipe 2	Units
Density ρ	1 195	1 190	[kg/m ³]
Oil/Water Ratio	74/26	80/20	
Oil Viscosity	4.477	4.477	[mPa·s]
Components			
Water	210.63	164.51	[kg/m ³]
CaCl ₂ Solution	46.62	36.40	[kg/m ³]
Ca(OH) ₂	5.62	4.30	[kg/m ³]
Emulsion (Primary and Secondary: One-Mul)	33.42	26.08	[kg/m ³]
Mineral Oil (EDC 95/11)	488.67	540.28	[kg/m ³]
Organophilic Clay (VG Supreme)	22.47	22.93	[kg/m ³]
Barite	387.57	395.50	[kg/m ³]

Table 1. Approximate formulation of the OBDF at 20°C.

The fluid-preparation process began by solving an appropriate amount of CaCl₂ solution into the water. This is done to prevent osmosis when drilling in water-sensitive shales. Next, Ca(OH)₂ was added into the solution, to increase the alkalinity of the drilling fluids to prevent corrosion of the equipment in the wellbore. To obtain stable emulsion in the OBDFs, the emulsifier, One-Mul, was mixed in to act as the primary and secondary emulsion. Subsequently, the mineral oil was added, making the fluid an invert emulsion, where the water was suspended into the fluid as water droplets. To suspend the particles and lift the cuttings, a viscosifier is necessary. Organophilic clay was used, due to its oil-wet surface, making it able to disperse in oil-based fluids. Lastly, the barite was mixed into the fluid as a weighting agent to gain the appropriate fluid density.

4.1.2 Water Based Drilling Fluids

The two water-based recipes prepared in the lab were typical field applicable inhibitive-WBDFs. Their components and fluid properties are tabulated in Tab 2.

Properties	Recipe 3	Recipe 4	Units
Density	1 300	1 295	[kg/m ³]
Water Viscosity	1.0	1.0	[mPa·s]
Components			
Water	861.15	857.84	[kg/m ³]
KCl	101.31	100.92	[kg/m ³]
Na ₂ CO ₃ (Soda Ash)	1.31	1.30	[kg/m ³]
Polymer (PolyPAC ELV)	7.60	7.57	[kg/m ³]
Starch (Trol FL)	4.43	3.15	[kg/m ³]
Xanthan Gum	2.53	3.78	[kg/m ³]
Barite	321.67	320.43	[kg/m ³]

Table 2. Approximate formulation of the WBDF at 20°C.

KCl, a soluble salt, is first added to the water. This additive is capable of efficiently stabilise exposed water-sensitive shale. Soda ash is then added to get the desired alkalinity (like Ca(OH)₂ in the OBDF recipes). This is followed up with polymer and starch. The polymer used controls fluid loss, is a shale inhibitor and a lubricator. The starch is added next, and it supplements the fluid loss control. Xanthan gum is the main viscosifier in these recipes. It enhances the suspension of the particles, while giving the drilling fluids their shear-thinning behaviour. As with the OBDFs, barite is used as a weighting agent to obtain desired fluid density.

4.2 Equipment and Experimental Procedure

4.2.1 Preparation and Treatment of the Drilling Fluids

All chemicals and additives used in the drilling fluids were weighted with a Mettler Toledo PB 1502-S balance with a precision of ± 0.01 g. This precision is necessary when preparing smaller fluid samples in the lab.

The OBDFs were mixed with a Heidolph Overhead Stirrer (~600-700 rpm). When all the chemicals had been added and there were 15 minutes left of the mixing time (indicated in Tab. 3), the mixer was switched to a Silverson high shear mixer. The Silverson requires the mixing head to be totally submerged in fluid, which were not possible at the start of preparing OBDFs, thus Heidolph was used first. The switch made it possible to mix at greater speeds

(~3000 rpm) than achievable with the Heidolph, thus, ensuring a better oil/water emulsion and particle dispersion.

When mixing the WBDFs, the initial water volume was large enough to use the Silverson from the start. The mixing speed was kept at ~2500-3000 rpm, thus, breaking apart aggregated particles and making an evenly dispersed fluid. After utilising the Silverson, the friction from the fluid particles increased the fluid temperature. Therefore, the fluids were left to cool overnight to regain room temperature before proceeding with measurements.

Order #	Oil Based Mud		Water Based Mud	
	Components	Mixing Time [min]	Components	Mixing Time [min]
1	Water	-	Water	-
2	CaCl ₂ solution	5	KCl	5
3	Ca(OH) ₂	5	Na ₂ CO ₃	5
4	One-Mul	10	PolyPAC ELV	10
5	EDC 95/11	10	Trol FL	10
6	VG Supreme	5	Xanthan Gum	10
7	Barite	10 + 15*	Barite	25

Table 3. Mixing times for each component of the OBDFs and the WBDFs, *10 min. Heidolph + 15 min. Silverson.

After completing the first set of measurements, each fluid was aged in a hot rolling oven, to simulate the circulation of a wellbore. Each sample was transferred to a mud cell before being left in the hot rolling oven at 80°C, a common reservoir temperature, to roll for 16 hours. When the test was complete, the samples were removed from the oven and left to cool for at least 3 hours. They were then measured with Anton Paar MCR 302, however the OFITE Model 900 measurements were completed the day after.

4.2.2 Drilling Fluid Measurements

Fluid density of each sample was obtained by using a Fann Model 141 Pressurised Mud Balance. When pressure is applied, the volume of potential air bubbles entrapped in the fluid sample decreases to a negligible amount. All density measurements were conducted between 20.5-21.5°C before the ageing test. The OBDF Recipes 1 and 2 had respective densities of 1195 and 1190 kg/m³, while the WBDF Recipes 3 and 4 had higher respective densities of 1300 and 1295 kg/m³. However, these values were difficult to read accurately from the measuring instrument.

The rheological measurements were done with OFITE Model 900, an oilfield viscometer made to satisfy API (OFITE, 2015), and Anton Paar MCR 302 Rheometer, a more advanced rheometer designed for laboratory testing. Both have rotational measurement systems

but are based on different rotational principle, as explained in Chapter 2.1.2. Drilling fluids being the objects of measurement, the OFITE 900 was utilised to obtain a representation of field data. However, coaxial cylinder rotational viscometers like OFITE 900 and Fann 35 have been shown to be inaccurate at low shear rates (LSRs) when measuring liquids exhibiting yield stress. Anton Paar MCR 302 has a more accurate measurement system due to its narrower shear gap, and more extensive range of shear rates. Hence, it is possible to model the viscous behaviour of the fluid more accurately. The shear gap (≈ 1 mm) is more than ten times larger than the largest barite particle of 0.075 mm, yielding a sufficient shear gap for rheological measurements of the selected fluids. However, other effects can influence the rheological measurements of the non-Newtonian fluids. This may include slippage and thixotropic behaviour at LSRs. If the fluid contains weighting particles, such as barite, sedimentation can also affect the measurements (Skadsem & Saasen, 2019).

Prior to these measurements, the fluid samples were re-mixed with a Heidolph Overhead Stirrer at 600 rpm for 1 minute to suspend and disperse the particles, making the fluid homogeneous. Measuring of the rheological behaviour of drilling fluid samples with the OFITE 900 was done at ramp down: 600 – 300 – 200 – 100 – 60 – 30 – 20 – 10 – 6 – 3 – 2 – 1 rpm. The fluids were sheared at a constant shear rate for 20 seconds before measurements were taken. This was followed up with 10 sec. and 10 min. gel measurements based on API specifications (American Petroleum Institute, 2014, 2019). When measuring with OFITE, the temperatures of interest were room temperature and 50°C, where 50°C is considered a standard temperature when reporting viscosity measurements in the field. The room temperature was kept constant at $21 \pm 1^\circ\text{C}$. To achieve 50°C in the fluid, an OFITE Universal Heat Cup was used. The OFITE measurements at 50°C were only conducted after ageing the fluid. When using this heating tool, the rheology of the used fluid might change, due to possible water evaporation. Thus, the heated fluid cannot be reused. The fluid volume required to fill the sample cup was too large for the test to be conducted before and after the ageing test, making this test not feasible before ageing the fluid.

The second set of data was obtained with the Anton Paar MCR 302 Rheometer by using its concentric cylinder system. The measuring cylinder was a CC27 with its associated cup, which is good for measuring low viscosity to viscoelastic liquids. All fluid samples were sheared at 1020 s^{-1} for 60 seconds in the cup, before the first measurement was taken at this shear rate. This was followed by a logarithmic ramp down with five measuring points per decade in the interval 511 down to 0.0511 s^{-1} , to evenly spread the measuring points on the

viscosity curve. The fluids were sheared at constant shear rate for 20 seconds before measurements were taken. These measurements were conducted at 25 and 50°C, before and after the fluid samples were aged. This was feasible with the MCR 302 due to the required sample volume being very small. The temperature was controlled by MCR 302's integrated temperature system. The system was temperature stable for 10 minutes with acceptable error of $\pm 0.1^\circ\text{C}$ before running the tests, making it very temperature accurate.

4.3 Implementing the Rheological Models

Fitting the Herschel-Bulkley, Eq. (1), and the Quemada model, Eq. (4), to the experimental data sets were done by the standard add-in solver program in Excel. When utilising this function, it is necessary to choose an objective, variable cells, constraints, and a solving method. The iteration will stop when the nonlinear GRG has repeated itself five times and the target change is significantly small. This is dependent on the convergence value, which in this case is set at the standard of 0.0001.

4.3.1 Fitting of the Herschel-Bulkley Model

When implementing the Herschel-Bulkley model, the yield stress was approximated through linear extrapolation of the two lowest measurement points. This was done under the assumption that no slippage happened when measuring the shear stress of the fluids with Anton Paar MCR 302. The MCR 302 has a far more extensive shear rate range compared to an oilfield viscometer, yielding low enough shear rate data to get a sufficient yield stress estimate for the purpose of this thesis.

The optimal values of the model-parameters, k and n , were determined through Excel's GRG Nonlinear solver method, where n was limited to $0 < n < 1$ for shear-thinning behaviour. The model was fitted for two different ranges of shear rates, where one adhered to the LSRs and the other to the HSRs, to obtain more accurate models. The LSRs represents the Newtonian wall shear rates of the annulus, and the HSRs the inside of the drill string, resulting in two different solutions for n and k . These results were obtained through reducing the RSS Eq. (20) in each of their relevant shear rate ranges. Each model curve reduced:

$$RSS = \sum_{i=1}^{N_p} (\tau_i - \hat{\tau}_i)^2 \quad (20)$$

where N_p is the number of measurement points, τ_i is the measured shear-stress values, and the $\hat{\tau}_i$ is the shear-stress values obtained by the curve fitted Herschel-Bulkley model.

The estimates for the wall shear rates were determined through the Newtonian wall shear rate described in Chapter 2.3.4. The estimates were made for hole-sections 8.5”, 12.25”, and 17.5” with a 5.5” drill pipe, with the respective pumping rates of 1800, 4500, 6000 lpm. The data represents typical field values determined from experience (Sayindla et al., 2017). The wall shear rates are expected to be below 250 s^{-1} , which is rarely exceeded in the field with the exception of the area around the bottom hole assembly (BHA) (Sayindla et al., 2017; Werner et al., 2017). The estimated wall shear rates were used as the specified shear rates ($\dot{\gamma}_s$) when determining the surplus shear stress $\tau_s = k\dot{\gamma}_s^n$ through the model parameters. This is a valid method when the model is accurately curve fitted within its relevant range of shear rates (Saasen & Ytrehus, 2018).

4.3.2 Fitting of the Quemada Model

In this study, the parameter variables are p , t_c , η_∞ , and η_0 , where the limiting viscosities are treated as theoretical values that can be estimated through curve fitting. As mentioned in Chapter 2.2.2, this model has a dimensionless shear variable dependent on shear stress or shear rate. In this study, the shear variable is shear rate dependent and defined as $\Gamma = (\dot{\gamma}/\dot{\gamma}_c)$. The objective was to reduce the weighted least square (WLS) to find the optimal values of the parameters. By reducing the WLS, all the low-viscosity values at HSRs were not completely outweighed by the large values at LSRs. The reducing eq. is defined as:

$$WLS = \sum_{i=1}^{N_p} \frac{1}{\eta_i} (\eta_i - \hat{\eta}_i)^2 \quad (21)$$

where the measured viscosities are η_i and the Quemada model viscosities are $\hat{\eta}_i$. The WLS will be used as a goodness-of-fit indicator on which curves modelled by Quemada is the most accurate.

The initial values for the parameters were decided by an educated guess before the Excel solver iterated a solution by using GRG Nonlinear as the solution method. The parameters to be fitted were limited within acceptable constraints. These consisted of the zero-shear plateau being larger than the highest measured viscosity and varying freely to infinity, while the infinite-shear plateau could vary from the lowest measured viscosity to zero. The exponent p was pre-defined by Quemada (1998), and the characteristic time was limited by the applied shear range.

To verify the best fit solutions of the model parameters, the limiting maximum packings ϕ_∞ and ϕ_0 were calculated by rearranging Eq. (6), by using the fitted limiting viscosities, suspending fluid viscosity, and solid volume fraction. These values verify pseudo-plastic fluids when $\phi < \phi_0 < \phi_\infty$ (Quemada, 1998). In the case of determining the viscosity of the Newtonian suspending fluid η_F of the OBDFs, the relevant temperatures, 25 and 50°C, were excluded from the known values, 20 and 40°C. These were estimated from the Arrhenius relationship, $\eta = Ae^{B/T}$. This relationship contains two liquid constants, A and B, and describes the absolute temperature dependency of the viscosity. Increasing the temperature in the Newtonian fluid will decrease the viscosity, and higher viscosity gives greater temperature dependency (Barnes et al., 1989). On the other hand, the solid volume fractions and the suspending fluid viscosity of the WBDFs were based on non-saline water, despite containing KCl-salt. However, the effects of the salt were assumed to be negligible and were omitted from this study, due to the limiting viscosities not being determined by use of the volume fraction parameters.

5 Results and Discussions

This chapter analyses the rheological properties and behaviours through the fluid measurements and the graphically represented flow curves. The rheological change is characterised by data obtained at elevated temperatures and after dynamic ageing. To represent the areas outside measurements, Herschel-Bulkley and Quemada model were applied and analysed in terms of the modelled flow and viscosity curves, and the model parameters. Additionally, calculated parameters have been added and evaluated to substantiate the models.

5.1 Laboratory Results and Fluid Rheology

The results of the measurement data obtained by use of MCR 302 and OFITE 900 is presented in this subchapter. As mentioned in the beginning of Chapter 4.1, two comparable batches were made to ensure the integrity of the experiments. When the OBDFs, Recipes 1 and 2, were prepared, the first two batches of Recipe 1 were deemed not comparable, based on the large absolute percentage errors (APEs) between the different batches. However, the measurements of Batches 3 and 4 were comparable. The mean absolute percentage error (MAPE) of the measured shear stresses in Recipe 1 varied from 5.9-9.3%. For Recipe 2, Batches 2 and 3 were comparable with acceptable MAPE of 2.3-8.3%.

The preparation of the WBDFs were easier. Both WBDF recipes, referred to as Recipes 3 and 4, had acceptable Batches 1 and 2. The WBDFs had lower MAPE between the batches than the OBDFs. Recipe 3 had a MAPE of 2.7-3.8%, while Recipe 4 had a MAPE of 0.5-1.1%. The MAPE of the WBDFs measured with OFITE at 50°C have been omitted due to OFITE's inability to measure at low shear rates (LSRs), which is discussed further in the next section.

Some deviations between the different batches were expected. Viscosity is sensitive to particle concentration when the solid volume fraction ϕ is higher than 0.3, and especially around a ϕ of 0.5. Small batches leave room for weighing errors, affecting the viscosity of the fluid. Recipe 1 have the highest ϕ of 0.399, and consequently the highest MAPEs. In comparison, Recipe 2 where ϕ is 0.336, have lower MAPEs. The solid volume fractions of the WBDFs were $\phi < 0.3$ and thus were not largely affected by changes in the particle concentration (Barnes et al., 1989).

The measurement data have been tabulated and can be found in Appendix A and B. The tables and their respective APEs vary depending on the measurement instrument, applied temperatures, and whether the fluid was aged or not. Generally, the APEs can yield large errors

in low values, in comparison with high values. This were reflected in some of the LSR measurement results, tabulated in Appendix A and B, but do not necessarily reflect bad results.

The rest of the results were based on Recipe 1 Batch 3 (OBDF 1), Recipe 2 Batch 2 (OBDF 2), Recipe 3 Batch 1 (WBDF 3), and Recipe 4 Batch 1 (WBDF 4) when characterising the flow and viscosity behaviour, temperature and ageing effects, and the applied models.

5.1.1 Properties and Flow Behaviours

This chapter characterises the measured fluid properties and the rheological behaviours before the models were applied, with respect to the different measurement instruments. The measured shear stress/shear rate relationship at room temperature is presented in Fig. 8. The OFITE 900 and MCR 302 measurement curves show the expected shear-thinning behaviours as explained by Fig. 3 curve (2) in Chapter 2.1.3. At HSRs, both OBDFs show a steep linear slope, before a more shear-thinning behaviour at LSRs. In comparison, the WBDFs have a more characteristic shear-thinning behaviour due to the flatter slope at HSRs.

The MCR 302 measurements show smooth curves through all measurement points. However, the OFITE 900 measurements demonstrated a dip in the curve at all 20 rpm readings (34 s^{-1}). Due to the regularity of this inconsistency, it was concluded to be an instrument error at the 20 rpm measurements, and these measurement points were omitted from the analysis.

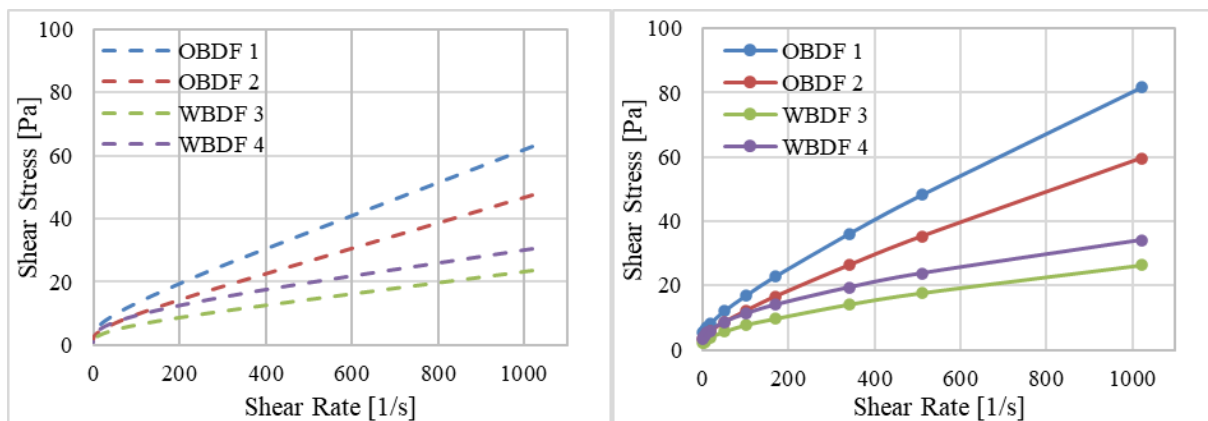


Figure 8. OBDF and WBDF: MCR 302 at 25°C (left) and OFITE at 21°C (right).

When comparing OBDF 1 and OBDF 2, the former shows higher viscosity compared to the latter. A study conducted by Halvorsen et al. (2019) showed that decreasing oil-water ratio (OWR) of invert emulsions results in increased viscosity. The same behaviour is observed in this study, where the OWR of OBDF 1 is lower compared to OBDF 2. In invert emulsions, the water droplets act as suspended particles, thus the increased particle concentration resulted in increased internal friction, i.e. higher viscosity.

In the WBDFs, the content of starch was decreased while the content of xanthan gum was increased from Recipes 3 to 4, i.e. replacing one type of polymer with another. The viscosity was affected by the change due to the xanthan gum being more viscosifying compared to starch (Schlumberger, n.d.-a, n.d.-b).

Comparing the different measurement methods in Fig. 8 were not feasible due to the differences in temperature influencing the flow curves, thus resulting in lower values obtained by MCR 302. Different measurement results were expected due to the size of the shear gap being different in the two instruments (Skadsem & Saasen, 2019; Werner et al., 2019) Additionally, OFITE can have some inaccuracies at LSRs due to the Newtonian shear rate assumption (see Chapter 2.1.2).

In this study, the most comparable data between MCR 302 and OFITE, were the 50°C measurements of the aged fluid, which is graphically represented in Fig. 9. The OBDF-curves in Fig. 9 (left) show OFITE measuring higher shear stress values compared to MCR 302. The measurement values of the OFITE might have some additional inaccuracies due to the difficulties in regulating the temperature of the universal heating cup. This resulted in temperature variations of $50 \pm 3^\circ\text{C}$. However, the OBDF-viscosities are generally not as affected by temperature variations at elevated temperatures as the fluids at 20-30°C (Halvorsen et al., 2019).

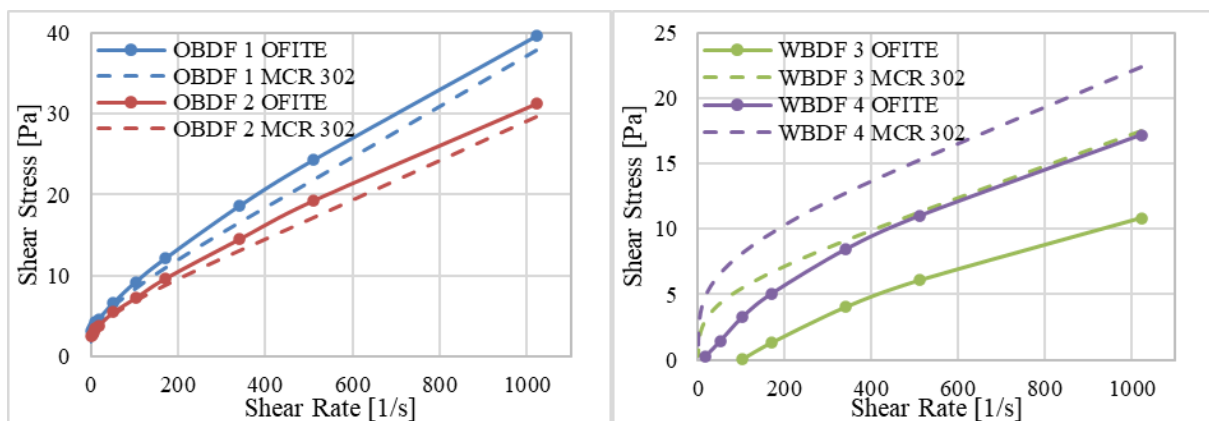


Figure 9. OFITE and MCR 302 measurements at 50°C after ageing: OBDF (left) and WBDF (right).

In Fig. 9 (right) contains the data based on the WBDF-measurements. The discrepancies between the MCR 302 and the OFITE are large, and OFITE was not able to measure the values of the entire shear rate range. To some degree, this may be caused by the difficulties in regulating the temperature of the heating cup. However, this were not likely to be the only cause, as the issue was observed in all batches measured with OFITE at 50°C. The results in Fig. 9 differs from Werner et al. (2016), where the Fann 35 measurements of the KCl-WBDF

were higher than the MCR 302 measurements, and the OBDf-measurements from MCR 302 were higher than Fann 35 measurements at 50°C.

Additional, fluid properties measured with the OFITE were the 10 sec. and 10 min. gel-strengths. The exact measured values are found in Appendix A. All the selected drilling fluids formed measurable gel-structures at $21 \pm 1^\circ\text{C}$. At 50°C the OBDfS still formed measurable gel-structures, while the WBDfS did not. As seen in Fig. 9 (right) the OFITE was not able to measure the shear stresses at the lowest shear rates and was therefore not able to measure the gel-strengths. If the MCR 302 was utilised for these measurements, other results may have been obtained. The rest of this study bases its analysis on the MCR 302 data, due to its extensive shear range, more accurate temperature system, and more reliable LSR measurements.

5.1.2 Temperature and Ageing Effects

As explained in Chapter 2.1.4, the rheological behaviours of drilling fluids were affected by temperature and ageing, and the resulting changes are characterised in this section. In Fig. 10 and 11, the rheological change of the fluids, caused by elevating the temperature from 25°C to 50°C, can be observed. The resulting curves show a general decrease in the shear stress measurements in all the fluid samples as a consequence of the increased temperature.

Fig. 10 displays the measured results of the OBDfS. The results show that the rheological change, caused by the temperature increase, are larger in OBDf 1 than in OBDf 2. This is due to the OWR, the higher water content in OBDf 1 (76/24) compared to OBDf 2 (80/20), resulted in a larger shear stress drop. However, there were also some smaller variations in the concentration of the other compounds between the recipes (Tab. 1 in Chapter 4.1.1) that could affect the rheological change of the fluid.

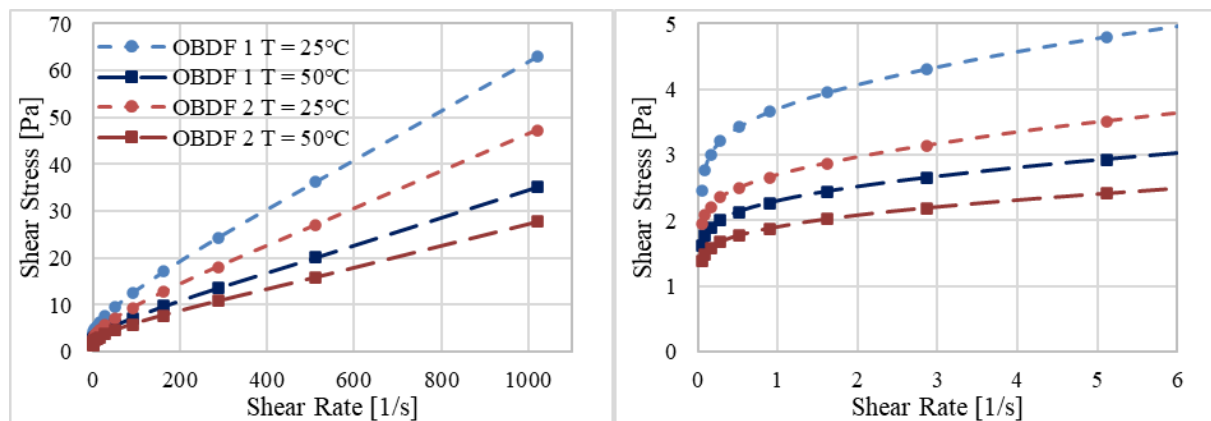


Figure 10. MCR 302: Temperature effects in OBDf for the entire shear rate range (right) and the very low shear rate range (left).

The rheological change in the WBDFs, caused by elevating the temperature, are displayed in Fig. 11, where the drop in the shear stress at HSRs of the WBDFs are very comparable and is not as considerable as in the OBDFs. It can be observed that the largest differences are at HSRs, before decreasing as the shear rate approaches zero.

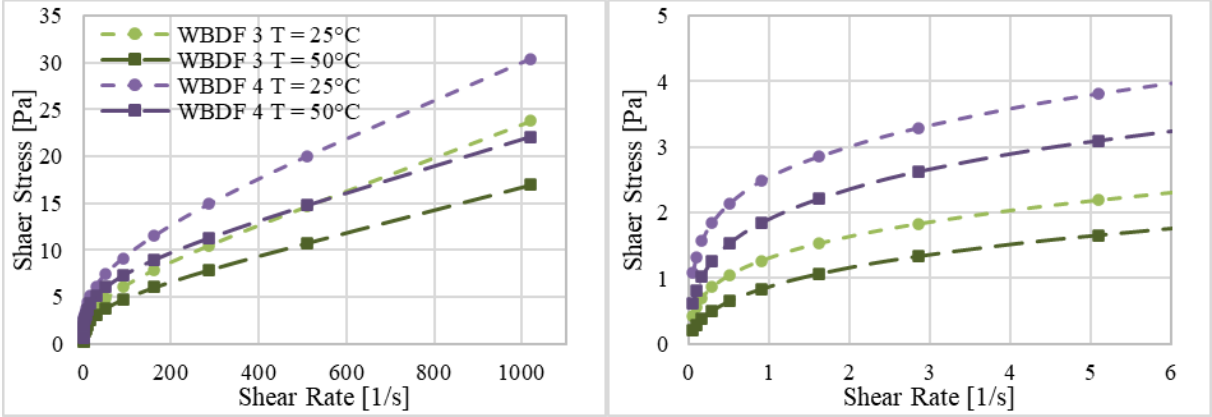


Figure 11. MCR 302: Temperature effects in WBDF for the entire shear rate range (right) and the very low shear rate range (left).

To simulate the drilling fluid circulation in a wellbore, the fluids were exposed to dynamic ageing. The results of ageing the OBDFs are shown in Fig. 12. The OBDFs have clearly been affected by the ageing process, yielding increased shear stress values. OBDF 1 was the fluid with lower OWR, and were slightly more affected by the ageing, most noticeable at HSRs.

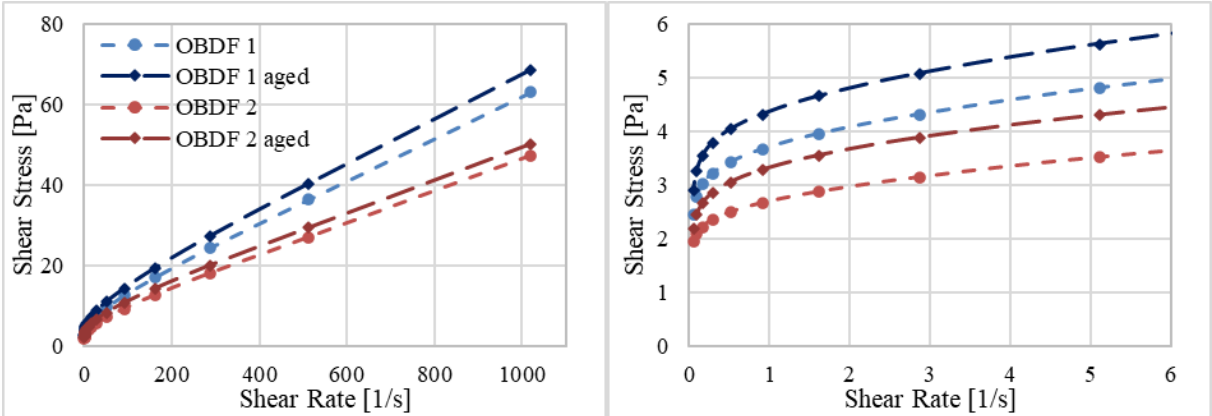


Figure 12. OBDF 25°C before and after ageing for the entire shear rate range (right) and the very low shear rate range (left).

When interpreting the effect of ageing in the WBDFs in Fig. 13, WBDF 3 clearly shows approximately the same shear stress values at 1020 s⁻¹, before diverging at lower shear rates where the aged fluid was more viscous. In WBDF 4, the aged fluid had a slightly lower viscosity at 1020 s⁻¹, before the flow curves intersect at lower shear rates where the aged fluid was more viscous.

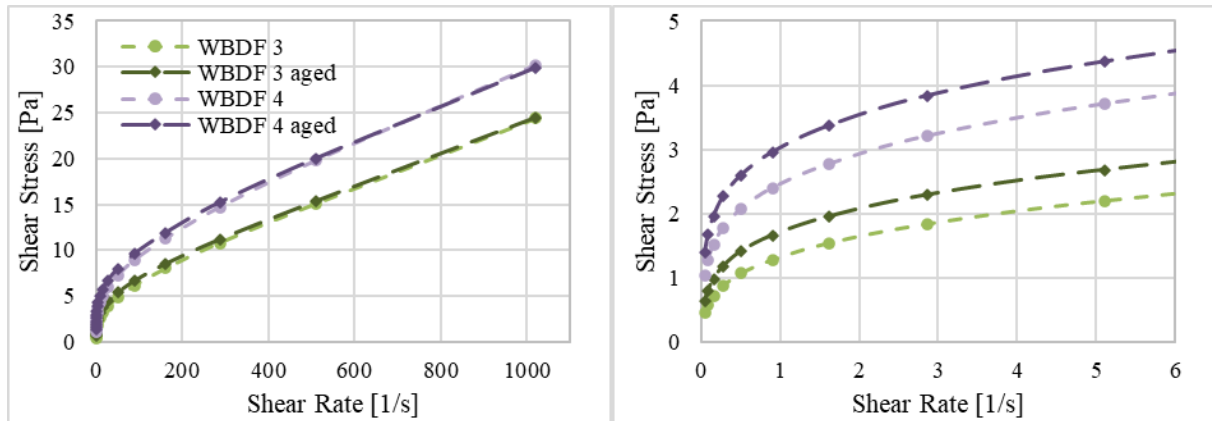


Figure 13. WBDF 25°C before and after ageing for the entire shear rate range (right) and the very low shear rate range (left).

The data from before and after ageing the OBDFs at 50°C show a very similar trend as the data at 25°C, except that the WBDFs at 50°C were consistently higher at 50°C after being aged. Because there were no significant differences in the trends in the data at 50°C, compared to 25°C, the graphical representation was not included. However, the measurement data can be found in Appendix A and B.

5.2 Herschel-Bulkley Model

The results of modelling the fluid with the Herschel-Bulkley model is presented and discussed in this section. The Herschel-Bulkley model served as a basis of comparison for Quemada model, due to its use in the drilling industry. Fig. 14-17 graphically represents the two different models for the fluids at 25 and 50°C. They only include the OBDFs and WBDFs before ageing. However, the fitted values of the aged fluids are added to Tab. 4 and 5. These figures also include the respective Newtonian wall shear rates for different hole-sections to display the different relevant shear rates compared to the model.

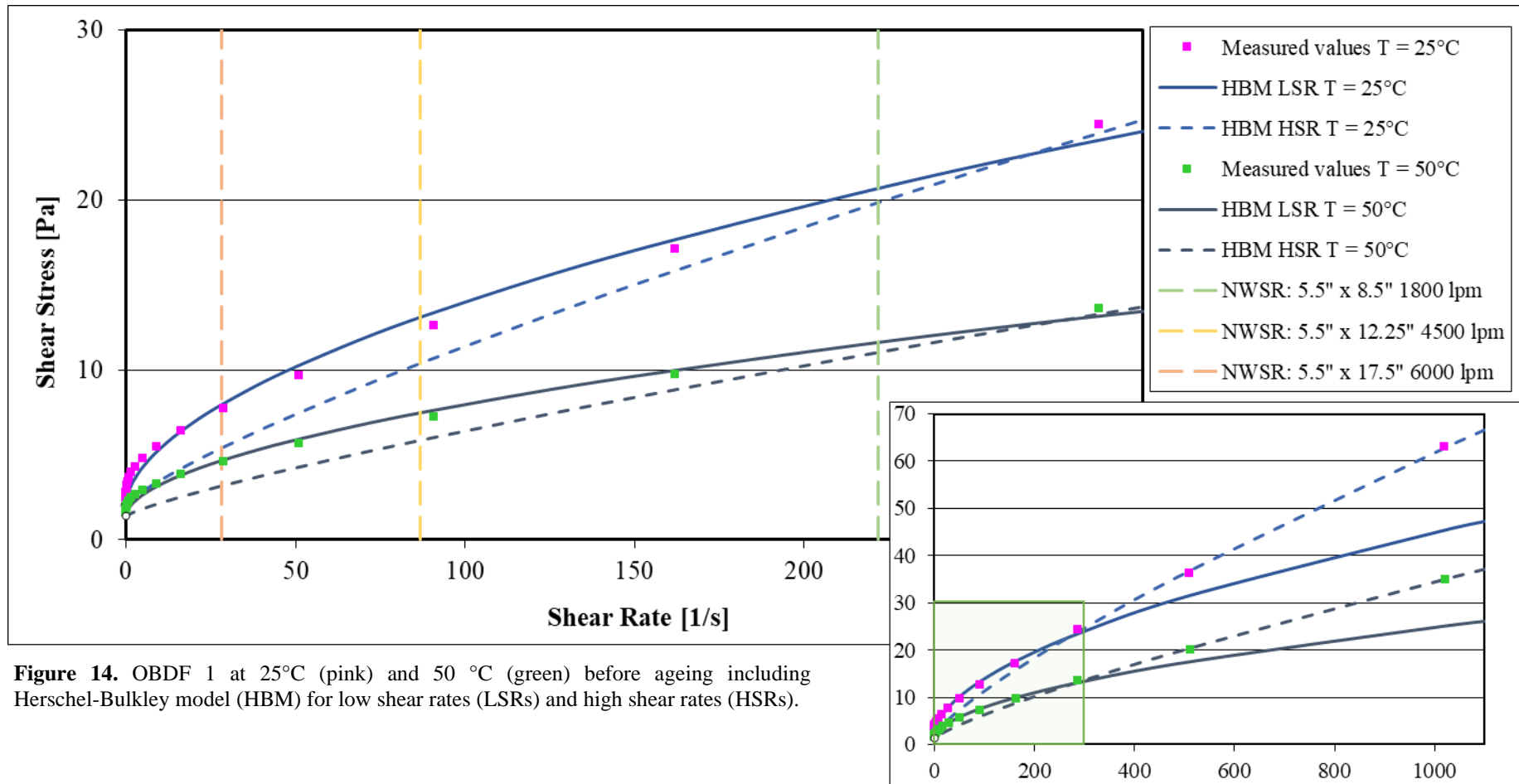
5.2.1 Flow Curves

Two Herschel-Bulkley model curves (denoted by HBM in the legend) along with the measurement data are included in Fig. 14-17. Having two different models for each of their respective shear rate range results in a more accurately fitted model. If the models were curve fitted for the entire measured range of shear rate, it would yield larger errors at the LSRs. The measured values and the Herschel-Bulkley model values are summarised in Appendix C along with their differences described by APEs.

The shear rates in the annulus rarely exceed 250 s^{-1} , except around the BHA (Sayindla et al., 2017; Werner et al., 2017). However, the curves named HBM LSR are curve fitted in the shear rate range of $0.0511\text{-}287 \text{ s}^{-1}$. In this case, the model rapidly deviates beyond the last measurement point included in the curve fitting. If the upper boundary, of the model shear rates, was limited to 162 s^{-1} , the model would under-estimate the values from 162 to 250 s^{-1} . To avoid this, the measurement point at 287 s^{-1} was included. The HSR ranges were curve fitted from 287 to 1020 s^{-1} .

Fig. 14-17 consists of two graphs. The graph to the right includes the entire measured range of shear rates, where the LSR range, representing the annular gap, and is marked with a green square representing the figure to the left. The LSR range includes the calculated annular Newtonian wall shear rates for their respective hole-sections, denoted by NWSR in Fig. 14-17. The approximated yield stress values are marked with a white circle for their respective fluid.

By visually interpreting the curve fit of the models in Fig. 14, it is observed that the model curve HBM LSR at 25°C follows the general shape of the measurement points but the model does not go through most of them. Generally, the models of the LSR range over-estimated the upper half while under-estimating the lower half. In Fig. 15, the same curve fit is observed in OBDF 2 at 25°C . However, the HBM LSR at 50°C seem to go through most measurement points in both OBDF 1 and OBDF 2. For the WBDFs 3 and 4, Fig. 16 and 17 respectively, a better fit of the HBM LSR curves are observed, compared to the OBDFs. WBDF 3 were slightly superior to WBDF 4. This can be confirmed by the RSS values in the next section.



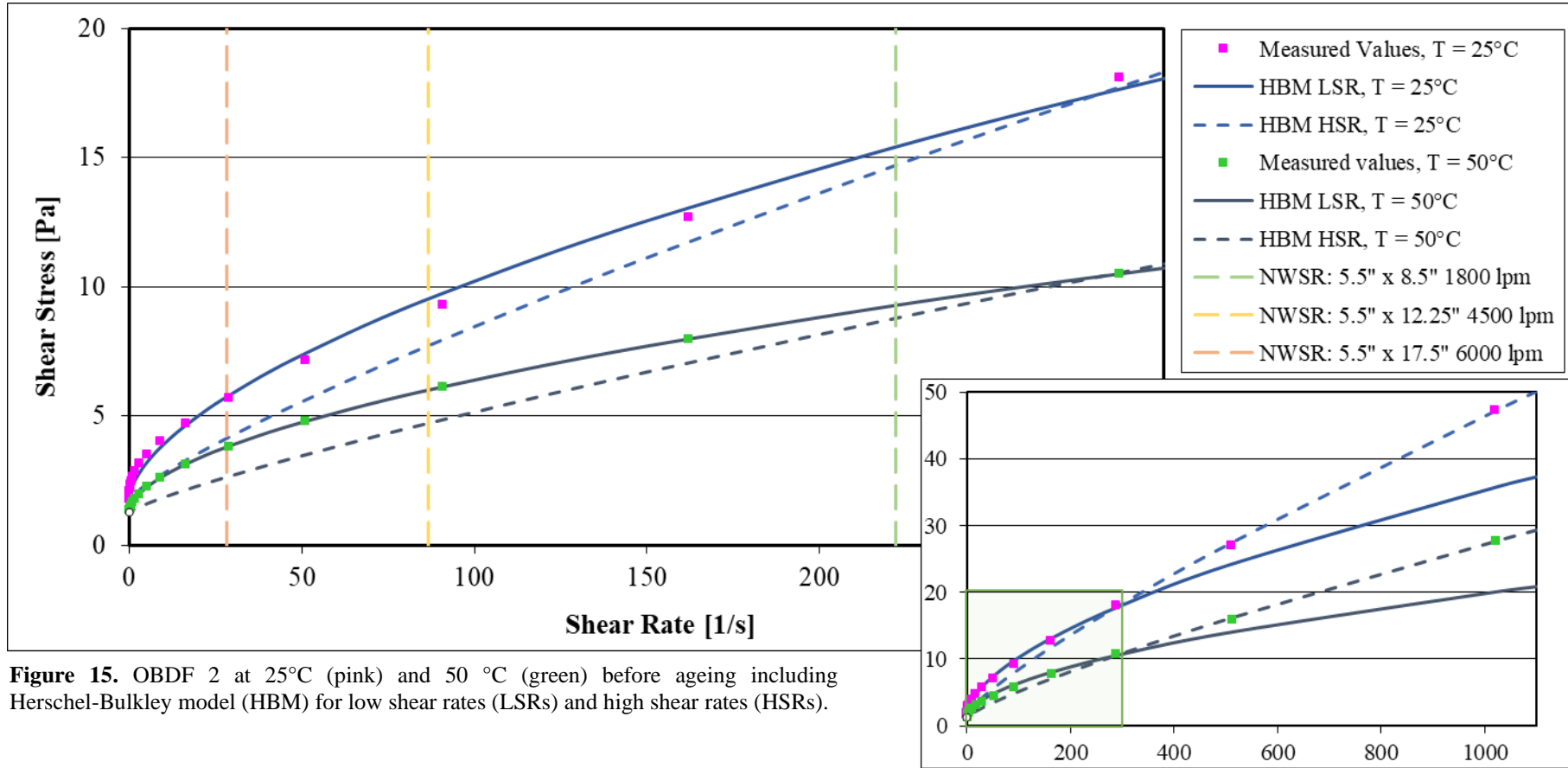
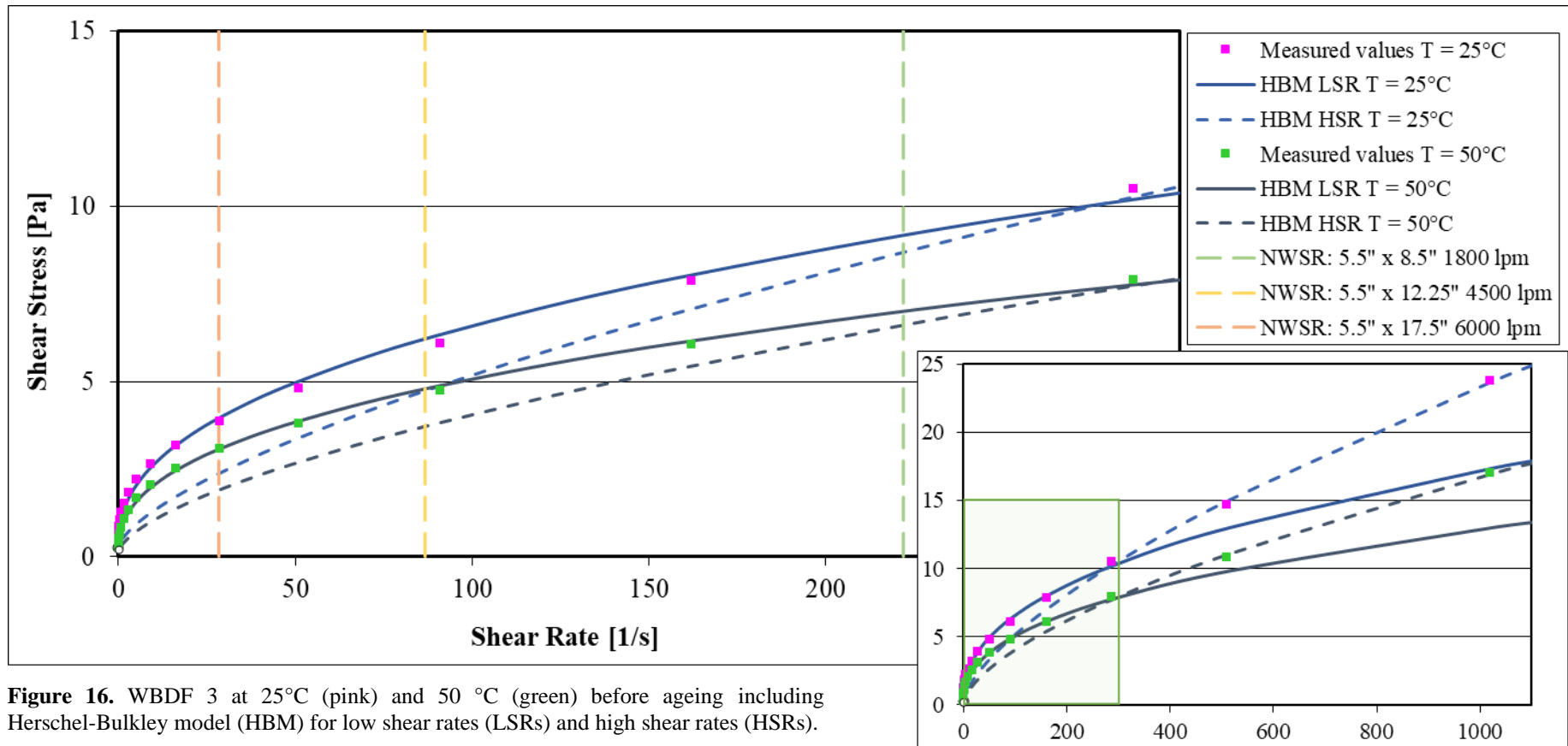


Figure 15. OBDF 2 at 25°C (pink) and 50 °C (green) before ageing including Herschel-Bulkley model (HBM) for low shear rates (LSRs) and high shear rates (HSRs).



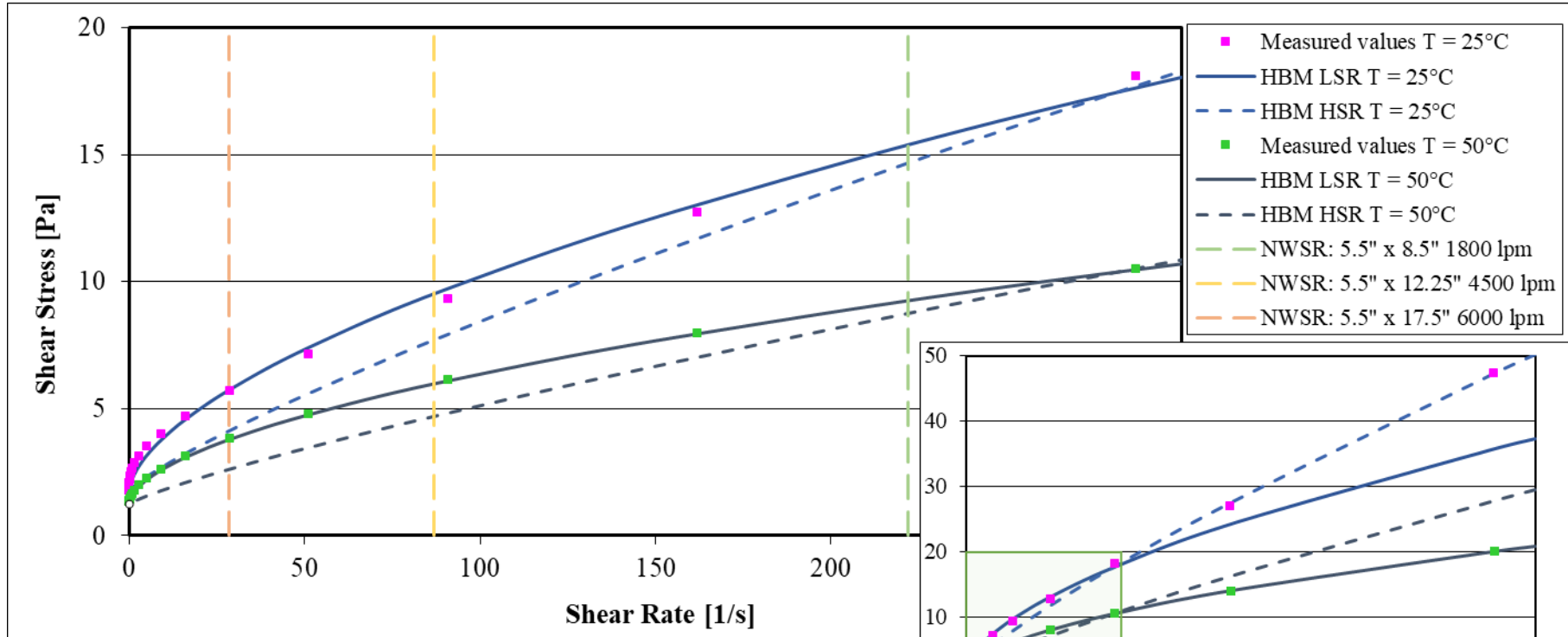


Figure 17. WBDF 4 at 25°C (pink) and 50 °C (green) before ageing including Herschel-Bulkley model (HBM) for low shear rates (LSRs) and high shear rates (HSRs).

5.2.2 Herschel-Bulkley Parameters

The results of the approximated the yield stresses and the Newtonian wall shear rates, along with the optimal curve fitted parameters, are summarised in Tab. 4 and 5. The OBDFs at 25 and 50°C, before and after ageing are in Tab 4., while the WBDF equivalents are in Tab. 5.

The yield stresses were approximated by extrapolating the lowest measurement points and resulted in higher yield stress values at 25°C and lower at 50°C in all the fluids. All the yield stress values increased from the non-aged to the aged fluids. This were expected since the shear stresses decreased when the fluids were heated and increased when they were aged. Extrapolating the yield stress values can be a good estimate if the shear rates are sufficiently low, like the MCR 302 measurements in this study, but this method provides a model value and not necessarily a physical property (Dzuy & Boger, 1983). Approximating the yield stress through this method left the n - and k -parameters to be curve fitted.

The flow behaviour indices were within the limits of shear-thinning behaviour. The n -values decreased significantly when the model changed from HSRs to LSRs, meaning the LSR range exhibited more shear-thinning behaviour than the HSR range. All fluids except for OBDF 1 became more shear thinning at LSRs when aged.

The k -values were not comparable with each other as they are dependent on their respective n -values, as explained in Chapter 2.2.1. Instead, the surplus shear stress values, relevant for different hole-sections, were used as a basis of comparison between fluids and were defined by the optimal model parameters of the LSR range. OBDF 1, as the most viscous fluid had the highest surplus shear stress values for its respective fluid conditions, followed by OBDF 2, WBDF 4, and WBDF 3, respectively. These values increased when the individual fluids were aged and decreased when the fluids were heated.

The least RSS quantified the goodness-of-fit but could only be used to compare the Herschel-Bulkley models for each of their respective shear rate range. According to the RSS, the model generally fitted WBDF 3 the best and OBDF 1 the least. The RSS_{LSR} values were very large in the OBDFs compared to the WBDFs. However, the RSS values depend on the magnitude of the viscosity values. Higher viscosity values, will to some degree, yield higher RSS values. OBDF 1 generally had the highest viscosity and RSS, and WBDF 3 generally had the lowest viscosity and RSS.

MAPE were not the best method in determining the accuracy of a model due to the low shear stress values, but it were a simple and intuitive method to demonstrate the vast

improvement in accuracy from Herschel-Bulkley to Quemada, which is discussed in Chapter 5.3.2.

Sample	OBDF 1		OBDF 1 (aged)		OBDF 2		OBDF 2 (aged)	
	25°C	50°C	25°C	50°C	25°C	50°C	25°C	50°C
τ_0	2.0391	1.4274	2.4506	1.7303	1.7831	1.2616	1.8690	1.3474
n_{LSR}	0.5553	0.5530	0.5447	0.5589	0.5989	0.5583	0.5289	0.5090
k_{LSR}	0.9271	0.5130	1.0949	0.5383	0.5350	0.3916	0.8721	0.5616
n_{HSR}	0.8064	0.7321	0.7846	0.8115	0.8258	0.8269	0.7897	0.8259
k_{HSR}	0.2280	0.2061	0.2872	0.1302	0.1488	0.0861	0.2024	0.1082
$\tau_s^{5.5" \times 8.5"} (\dot{\gamma}_s = 222)$	18.62	10.18	20.76	11.02	13.60	7.99	15.19	8.79
$\tau_s^{5.5" \times 12.25"} (\dot{\gamma}_s = 86.8)$	11.05	6.06	14.45	6.52	7.75	4.73	9.24	5.45
$\tau_s^{5.5" \times 17.5"} (\dot{\gamma}_s = 23.8)$	5.39	2.96	6.15	3.17	3.57	2.30	4.66	2.82
RSS_{LSR}	5.626	1.313	6.771	1.389	1.470	0.644	3.476	1.169
RSS_{HSR}	0.582	0.243	0.575	0.238	0.353	0.168	0.441	0.185
$MAPE_{LSR}$	11.4%	8.7%	10.6%	7.7%	7.5%	7.2%	9.7%	8.3%
$MAPE_{HSR}$	1.3%	1.5%	1.1%	1.3%	1.3%	4.6%	1.4%	1.5%

Table 4. OBDFs: Optimal Herschel-Bulkley model parameters and surplus shear stress at the different wall shear rates.

Sample	WBDF 3		WBDF 3 (aged)		WBDF 4		WBDF 4 (aged)	
	25°C	50°C	25°C	50°C	25°C	50°C	25°C	50°C
τ_0	0.2736	0.1011	0.4009	0.1435	0.7947	0.3972	1.0433	0.4756
n_{LSR}	0.4279	0.4109	0.3924	0.3746	0.3938	0.3566	0.3638	0.3320
k_{LSR}	0.8803	0.7487	1.1118	0.9740	1.4937	1.4225	1.7564	1.7067
n_{HSR}	0.6728	0.6249	0.6389	0.6004	0.5964	0.5563	0.5748	0.5272
k_{HSR}	0.2217	0.2219	0.2790	0.2700	0.4739	0.4581	0.5395	0.5655
$\tau_s^{5.5" \times 8.5"} (\dot{\gamma}_s = 222)$	8.89	6.89	9.26	7.37	12.34	9.77	12.54	10.26
$\tau_s^{5.5" \times 12.25"} (\dot{\gamma}_s = 86.8)$	5.95	4.69	6.41	5.19	8.55	6.99	8.91	7.51
$\tau_s^{5.5" \times 17.5"} (\dot{\gamma}_s = 23.8)$	3.42	2.75	3.86	3.19	5.15	4.40	5.56	4.89
RSS_{LSR}	0.382	0.119	0.472	0.204	0.848	0.326	0.913	0.489
RSS_{HSR}	0.153	0.089	0.145	0.109	0.186	0.157	0.256	0.180
$MAPE_{LSR}$	6.9%	10.3%	6.3%	11.4%	5.6%	7.3%	5.1%	7.4%
$MAPE_{HSR}$	1.6%	1.6%	1.6%	1.8%	1.3%	1.5%	1.4%	1.6%

Table 5. WBDFs: Optimal Herschel-Bulkley model parameters and surplus shear stress at the different wall shear rates.

5.3 Quemada Model

The results of the applied Quemada model are presented and discussed in this subchapter. The APEs between the model values and the measured values are found in Appendix D. The Quemada model predicts the viscous behaviour of the drilling fluids and is more complex compared to the Herschel-Bulkley model. The model curves, in Fig. 18-21, represent their respective fluids at 25 and 50°C before ageing. The model parameters of the OBDFs are summarised in Tab. 6 and the WBDFs in Tab. 7.

5.3.1 Viscosity Curves

This chapter analyses the flow behaviour of the drilling fluids through their viscosity profiles presented in Fig. 18-21. As explained in Chapter 2.1.4, shear-thinning fluids can have two different viscosity profiles depending on the existence of a zero-shear plateau. When Hodne et al. (2007) modelled cementitious materials with Quemada model, they characterised these viscosity behaviours as J- and S-curves (see Chapter 3).

Fig. 18 and 19 present the measured viscosity values of OBDFs 1 and 2 and their respective models. The measured values of all the OBDF-curves clearly deviated from the linear behaviour at HSRs indicating an infinite-shear plateau. The infinite-shear plateau signifies that the SUs of the fluid have broken apart completely, leaving only the initial particles and/or IFs (Quemada, 1998). Extending the measurement range beyond 1020 s^{-1} may have yielded the actual infinite-shear viscosity and more accurate models. However, the HSR range were not of great interest, as the annular wall shear rates mainly stay below 250 s^{-1} .

The viscosity curve in Fig. 18, representing OBDF 1, does not clearly indicate a zero-shear plateau at LSRs. Instead, by analysing the gradient of the LSR measurements at 25°C before and after ageing, the two lowest points at 0.0511 and 0.0909 s^{-1} , deviated from linear behaviour. This deviation indicated the existence of a zero-shear plateau. According to Hodne et al. (2007), the existence of a zero-shear plateau categorises an S-curve and denies the existence of true yield stress. This contradicts the approximated yield stress of the Herschel-Bulkley model in Chapter 5.2. The gradient of the fluid at 50°C before and after ageing did show slight deviation at the two lowest measured shear rates, but were not as prominently as at 25°C.

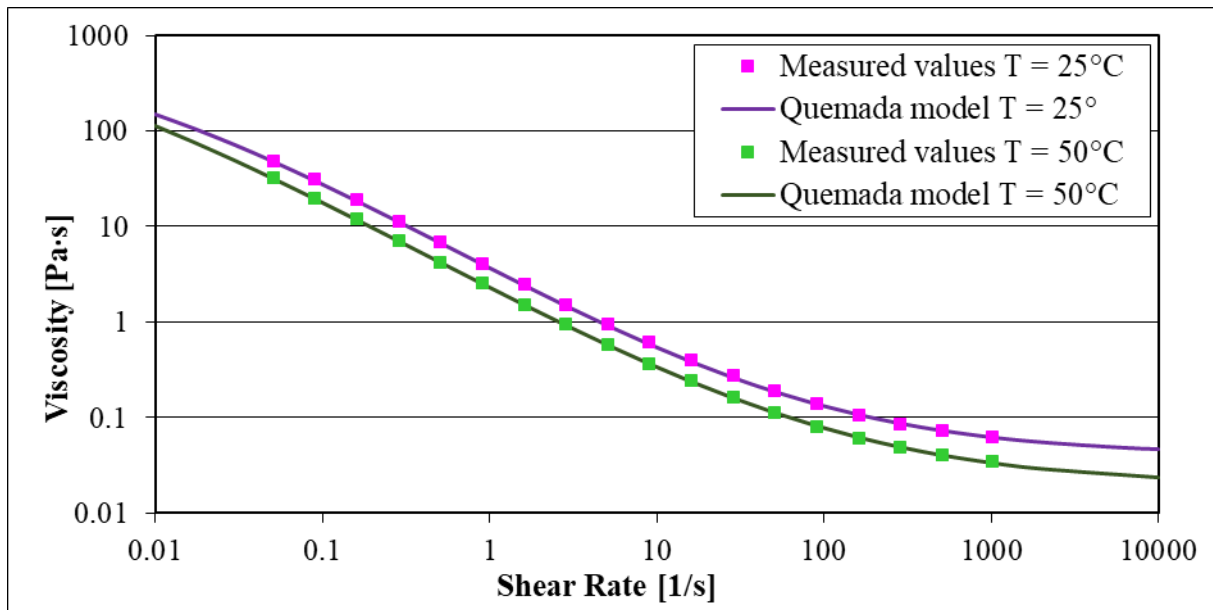


Figure 18. OBDF 1 at 25 and 50°C before ageing.

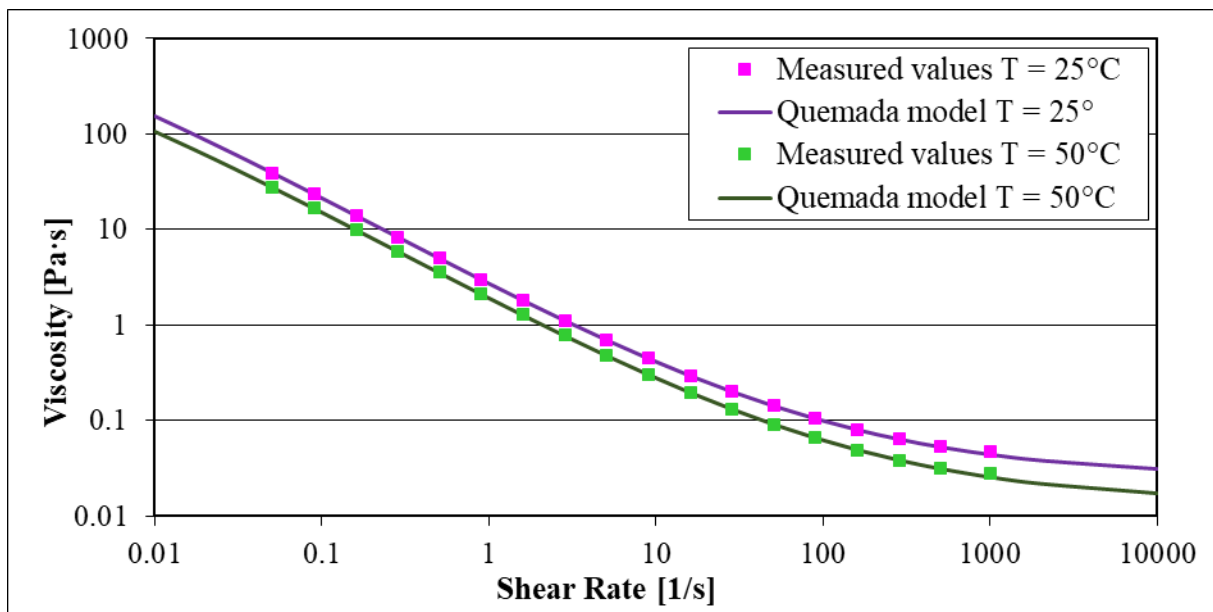


Figure 19. OBDF 2 at 25 and 50°C before ageing

On the other hand, the measured values of OBDF 2 in Fig. 19 indicated linear behaviour at LSRs, meaning these curves can be categorised as J-curves (Hodne et al., 2007). Under the assumption that yield stress existed, the OBDF 2 were a pseudo-plastic yield stress fluid, thus indicating the same as the results as the Herschel-Bulkley model in the previous section. However, this might suggest the fluid was not measured at sufficiently LSRs for the zero-shear plateau indication to appear, or that it was impossible to measure at sufficiently LSRs for it to appear. Consequently, it could be described by an apparent yield stress (Barnes et al., 1989).

With regards to temperature, the viscosity curve at 50°C shows the same behaviour as the one at 25°C, aside from generally having lower viscosity values.

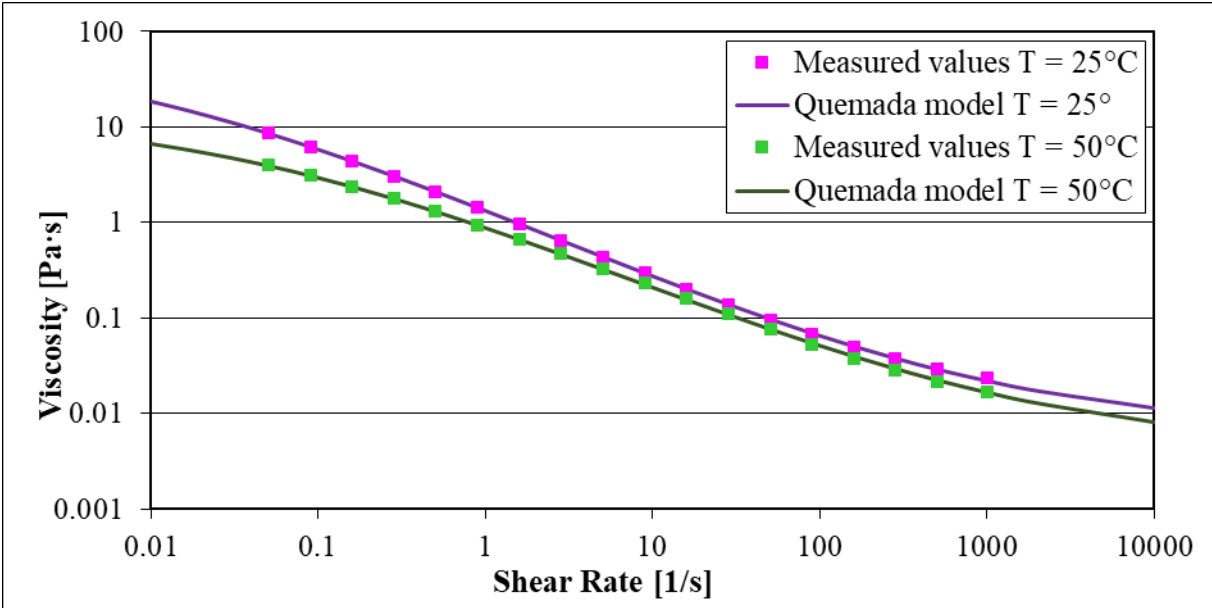


Figure 20. WBDF 3 at 25 and 50°C before ageing.

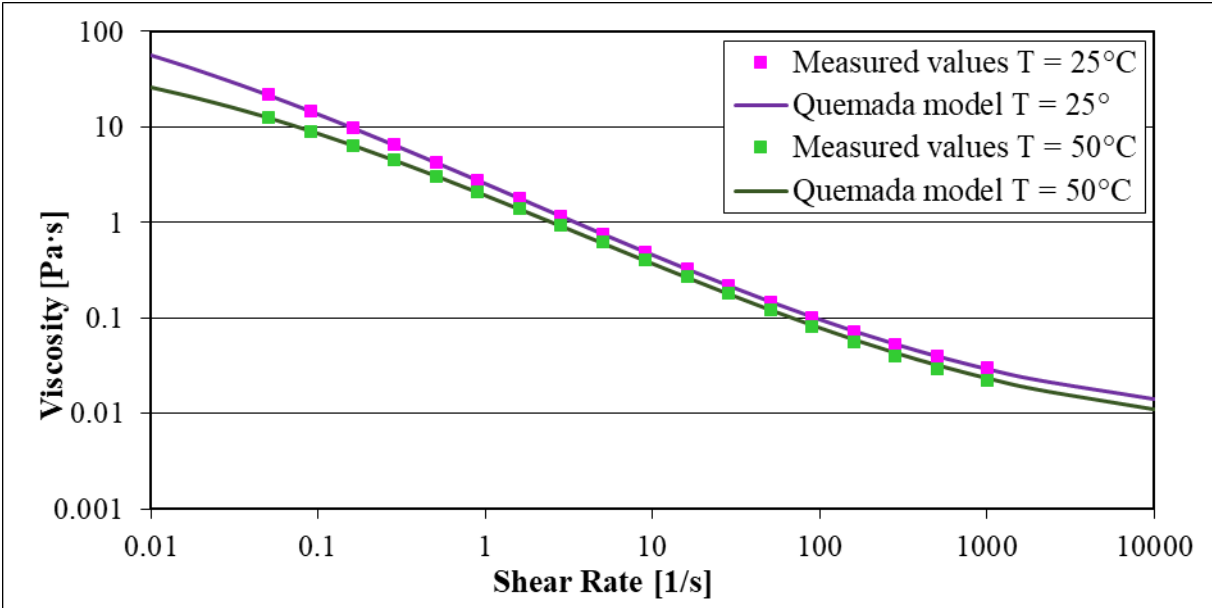


Figure 21. WBDF 4 at 25 and 50°C before ageing.

The viscosity curves, of the WBDFs at 25 and 50°C before ageing, are displayed in Fig. 20 and 21. The WBDFs behaved similarly to the OBDFs at HSRs in relation to the infinite-shear plateaus. Unlike OBDF 2, the measurement points of the WBDFs at LSRs clearly deviates from linear behaviour in Fig. 20 and 21, indicating the existence of zero-shear plateaus and were therefore categorised as S-curves. This fluid characteristic denies the existence of a true yield stress, opposing the assumptions made when modelling with the Herschel-Bulkley model.

The difference between the 25 and 50°C WBDF-viscosity curves were approximately constant at higher shear rates. This difference increased with decreasing shear rates due to the 50°C fluid-samples approaching the zero-shear plateau at a faster rate.

The curve fit of the model to the experimental data were evaluated through Fig. 18-21 by visual observation. All the obtained model curves hit all the measurement points, demonstrating the models' high accuracy in describing the fluid behaviour though the entire shear rate range. On the other hand, the Herschel-Bulkley model had to limit its shear rate range to obtain better accuracy, still missing several of the measurement points in most of the modelled curves. The study being limited to only four drilling fluids made the results more prone to coincidences. The study can conclude that the Quemada model can predict the rheological behaviours of the studied drilling fluids with high accuracy, but other drilling fluids may yield different results.

The differences between the viscosity converted Herschel-Bulkley model and the Quemada model is displayed in Fig. 22. The annular shear rates were assumed to not exceed 250 s⁻¹ and is marked in the figure. Herschel-Bulkley model were not able to account for the infinite- and zero-shear plateaus, due to its linear behaviour describing a yield stress fluid. The Herschel-Bulkley curve shows large discrepancies from the measurement points at LSRs because of the regression method used (RSS). However, it did describe the higher shear rates, still below 250 s⁻¹, more accurately. Quemada, on the other hand, followed the shape of the measurement points throughout the entire measurement range.

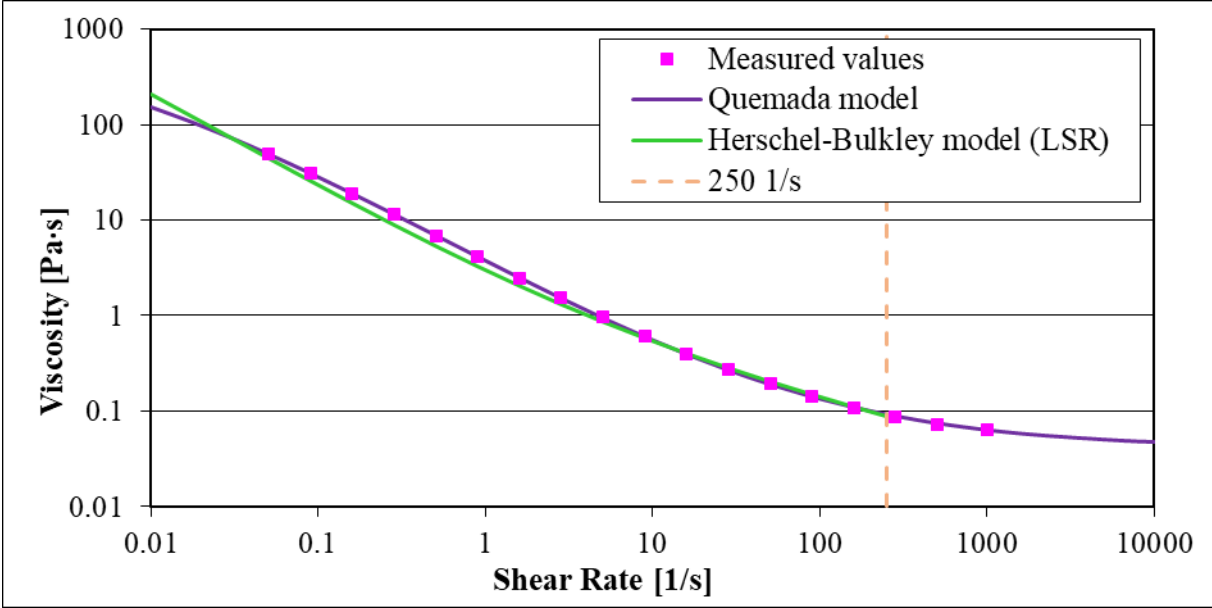


Figure 22. OBDF 1 at 25°C, Herschel-Bulkley and Quemada model comparison.

5.3.2 Curve Fitted Quemada Parameters

Each viscosity curve was fitted with four parameters: p , t_c , η_0 and η_∞ . The results of the fitting process of the OBDFs can be observed in Tab. 6 and the WBDFs in Tab. 7. The difference in the values depends on the fluid properties and the rheological behaviour at different simulated well conditions.

As mentioned in Chapter 2.2.2, according to Quemada (1998) the exponent p in Eq. (4) must be limited to $0 < p < 1$, and has often been found to be close to 0.5 (van der Werff & de Kruif, 1989). The p -parameter of the OBDF-samples were found to be close to 0.5, at 0.49880-0.52542 for OBDF 1 and at 0.49619-0.50439 for OBDF 2. The values of the WBDFs were somewhat lower, at 0.41436-0.43272 for WBDF 3 and at 0.43081-0.44746 for WBDF 4. Hodne et al. (2007) described the J- and S-curves in terms of the p -parameter, where J-curves had $p < 0.5$ and S-curves $p > 0.5$. The p -parameters of this study do not describe the shape of the curves, like the curves in Hodne et al.' (2007) study. However, increasing the p -parameter, while the other parameters were kept constant, gave the curve a more prominent S-shape.

Hodne et al. (2007) recognised the characteristic time t_c , as defined by Quemada (1998) to be the time needed for obtaining a suspension of almost mono-disperse SUs. The t_c -parameters ($t_c = \dot{\gamma}_c^{-1}$) of the OBDFs and WBDFs were limited within the given boundaries of pseudo-plastic behaviour, which were determined from the applied range of shear rates (Quemada, 1978). The applied shear rate range of 0.0511-1020 s^{-1} yielded the characteristic time range of 0.00098-19.569 s. The t_c -parameters for the OBDF-samples ranged from 0.00795-0.01488 s for OBDF 1 and 0.00698-0.01087 s for OBDF 2, with the respective $\dot{\gamma}_c$ interval of 67-126 s^{-1} and 92-143 s^{-1} . The WBDFs generally showed lower values of t_c , compared to the OBDFs. WBDF 3 ranged from 0.00098-0.00151 s and WBDF 4 from 0.00098-0.00112 s, with the respective $\dot{\gamma}_c$ ranging from 662-1020 s^{-1} and 893-1020 s^{-1} . In the heated WBDF 3 and the heated and/or aged WBDF 4, the t_c -parameters were equal the boundary limit of 0.00098 s^{-1} . As explained in Chapter 2.3.5, the t_c -parameters are temperature dependent and should decrease with increased temperatures. This effect was reflected in the results achieved by Baldino et al. (2018) and by the results of the fitted t_c -values in Tab. 6 and 7, except in WBDF 4 after ageing (Tab. 7), where t_c was constant at the lower boundary of 0.00098 s. The WBDFs at the lower boundary would have yielded even lower values without the limit. The model was still very accurate in describing the rheological behaviour despite the higher APEs at HSRs in comparison with the other curves. The low-viscosity values at HSRs made the APEs more prone to take on extreme values and did not necessarily describe a bad curve fit.

	OBDF 1		OBDF 1 (aged)		OBDF 2		OBDF 2 (aged)	
	25°C	50°C	25°C	50°C	25°C	50°C	25°C	50°C
p	0.52542	0.50691	0.51672	0.49883	0.49619	0.49727	0.50439	0.49997
t_c	0.01488	0.01001	0.01209	0.00796	0.01087	0.00807	0.00942	0.00698
η_0	859	1362	1244	2740	4345	2520	1254	1231
η_∞	0.04107	0.01937	0.04201	0.01897	0.02591	0.01392	0.02765	0.01447
WLS	0.00524	0.00069	0.00259	0.00030	0.00028	0.00024	0.00101	0.00028
MAPE	1.4%	0.9%	0.9%	0.8%	0.6%	0.8%	0.7%	0.8%

Table 6. OBDF: Optimal parameters of the Quemada model.

	WBDF 3		WBDF 3 (aged)		WBDF 4		WBDF 4 (aged)	
	25°C	50°C	25°C	50°C	25°C	50°C	25°C	50°C
p	0.41934	0.41436	0.42924	0.43272	0.43081	0.43195	0.43954	0.44746
t_c	0.00151	0.00098	0.00118	0.00098	0.00112	0.00098	0.00098	0.00098
η_0	71	14	112	19	403	63	525	90
η_∞	0.00651	0.00427	0.00592	0.00443	0.00765	0.00592	0.00731	0.00597
WLS	0.00030	0.00109	0.00027	0.00166	0.00010	0.00255	0.00026	0.00168
MAPE	1.0%	1.8%	0.9%	1.9%	0.4%	2.6%	0.7%	2.2%

Table 7. WBDF: Optimal parameters of the Quemada model.

The infinite- and zero-shear viscosities of OBDF 1 range from 0.01895-0.04201 Pa·s and 859-2739 Pa·s, respectively. The infinite- and zero-shear viscosities decreased when the fluid temperature were increased, due to the fluids rheological behaviour described in Chapter 5.1.2. Yet, the zero-shear viscosities of OBDF 1, before and after ageing, increased along with the temperature. The optimal infinite- and zero-shear viscosities being determined through curve fitting, instead of through fluid properties, explained this behaviour. OBDF 1 at 25°C deviated more from linear behaviour at LSRs compared to OBDF 1 at 50°C, which lead to lower fitted zero-shear viscosity. Another expectation was the increase of the limiting viscosities after ageing due to the fluid's viscosity increasing as shown in Chapter 5.1.3. This behaviour was observed in Tab. 6 at 25°C. However, the opposite happened when the fluid was compared before and after ageing at 50°C. This might have been due to the larger absolute percentage error (APE), between the modelled curve and the last measuring point, in the latter. Thus, indicating the HSR range of this curve not being fitted as accurately as the other. However, these values were outside the scope of interest and were not evaluated further, because the shear rates of interest were lower.

In OBDF 2, the infinite-shear viscosities range from 0.00592-0.00765 Pa·s, where the values decreased with increased temperature, and increased after ageing. The zero-shear viscosity decreased with increased temperature in the range of 1231-4345 Pa·s, thus having the

opposite behaviour of OBDF 1. This is expected due to the rheological behaviour described in Chapter 5.1.2. However, the zero-shear viscosity values decrease after the fluid had been aged. As explained in OBDF 1, this were due to the gradient of the viscosity curve at LSRs.

The infinite- and zero-shear viscosities of the WBDFs in Tab. 7 are far lower compared to the OBDFs in Tab. 6, as the WBDFs generally had a lower viscosity profile. The infinite- and zero-shear viscosities of WBDF 3 range is 0.00427-0.00651 Pa·s and 14-112 Pa·s, respectively. Additionally, WBDF 4's range were 0.00592-0.00765 Pa·s and 63-525 Pa·s, respectively. The resulting optimal parameters described the same behaviours as discussed in Chapter 5.1.2. Unlike the OBDFs, the fitted infinite-shear viscosity decreased after ageing due to the flow curves intersecting at HSRs at 25°C, while it increased at 50°C due to the flow curves never intersecting at HSRs. On the other hand, the fitted values of zero-shear viscosity increased when the fluid was aged and decreased at 50°C in both WBDF 3 and WBDF 4. These effects are represented better in the WBDFs due to the fluids more clearly indicating a zero-shear plateau. With this it was possible to conclude that the curve-fitted infinite- and zero-shear viscosities could to some degree describe the rheological behaviour of the drilling fluids. However, in the case of the zero-shear viscosity, this were made possible due to the LSR measurements, the same analysis may not have been possible by using an oilfield viscometer. This was illustrated in Fig. 4, Chapter 2.1.3.

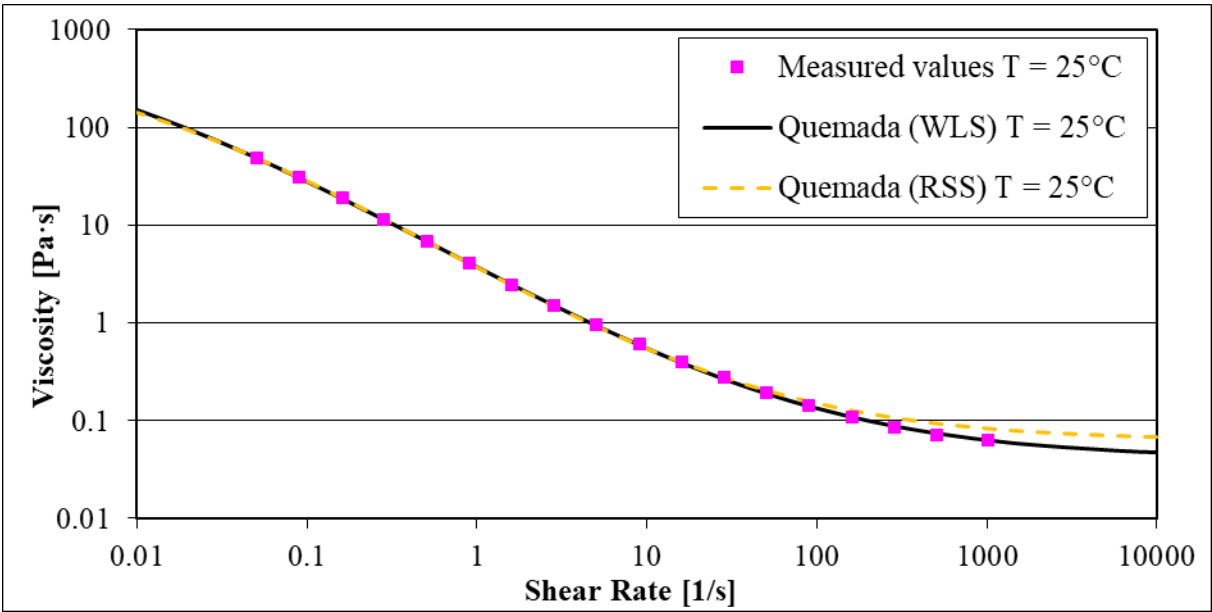


Figure 23. OBDF 1 at 25°C before ageing, curve fitted using residual sum of squares (RSS) and weighted least square (WLS).

The model was fitted with NRL by reducing the WLSs due to it better fitting the entire shear rate range without disregarding the low-viscosity measurements at HSRs. Fig. 23 illustrates how RSS can over-estimate the viscosity curve at HSRs, while the WLS regression

method yields an overall better fit. The WSL results, like RSS, can only be used as a comparison with the same model over the same range. The goodness-of-fit were the best in WBDF 4 at 25°C before ageing and the worst in OBDF 1 at 25°C before ageing. However, it can be concluded that the Quemada model were able to fit all the drilling fluids of this study by observing the model in comparison with the measurement data in Fig. 18-21.

As mentioned earlier, MAPE were added due to its intuitive measure of accuracy. The APE values, in Appendix D, show higher values at HSRs due to the low viscosities, thus drawing up the MAPEs. Nonetheless, the MAPE of all the modelled Quemada curves were very low, indicating great accuracy and were an improvement compared to the Heschel-Bulkley models.

A better fit were expected of the Quemada model, due to it having four parameters and yielding more degrees of freedom to fit the curve to the experimental data, compared to the two of the Herschel-Bulkley model. The added complexity of the Quemada made it statistically more likely to have higher accuracy. Whether the added accuracy of the Quemada model is a trade for Herschel-Bulkley's simplicity is something that can be explored further in future works.

5.3.3 Calculated Quemada Parameters

By using the fitted limiting viscosities of Tab. 6 and 7, the structural index χ and the limiting maximum packing fractions, ϕ_∞ and ϕ_0 , were calculated. The model criteria for pseudo-plastic behaviours are $0 < \chi < 1$ and $\phi < \phi_0 < \phi_\infty$ (Quemada, 1998) and were verified through the calculated parameters in Tab. 8 and 9.

The pseudo-plastic criteria of the structural indices were within the required limits and all the modelled cases were verified. The limiting maximum packing fractions, obtained through rearranging Eq. (6), also fulfilled the pseudo-plastic criteria and further verified the models. The zero-shear maximum packing fraction ϕ_0 were all slightly above ϕ , while the infinite-shear maximum packing fractions ϕ_∞ were increased more significantly in comparison. The conducted measurements, to calculate the solid volume fraction, were done at $20 \pm 1^\circ\text{C}$ and was assumed to be constant. In the OBDFs, the suspending fluid were mineral oil alone. The suspending fluid viscosity η_F of the mineral oil were approximated though Arrhenius relationship to get the viscosity at the relevant temperatures. Determining the solid volume fraction of the WBDFs were simplified by excluding the salt from the suspending fluid, leaving only water. Furthermore, tabulated values of water viscosity were used, assuming the salt

content to be negligible in both instances. The solid volume fraction was largest in OBDF 1, followed by OBDF 2, WBDF 4, and WBDF 3, respectively. This were reflected by the flow curves in Fig. 8 in Chapter 5.1.1, where OBDF 1 showed the largest viscosity followed by OBDF 2, WBDF 4, and WBDF 3, respectively.

Calculated Values	OBDF 1		OBDF 1 (aged)		OBDF 2		OBDF 2 (aged)	
	25°C	50°C	25°C	50°C	25°C	50°C	25°C	50°C
χ	0.00691	0.00377	0.00581	0.00263	0.00244	0.00235	0.00470	0.00343
η_F	0.00396	0.00232	0.00396	0.00232	0.00396	0.00232	0.00396	0.00232
Φ	0.399	0.399	0.399	0.399	0.336	0.336	0.336	0.336
ϕ_0	0.39986	0.39952	0.39971	0.39937	0.33632	0.33632	0.33660	0.33646
ϕ_∞	0.57886	0.60986	0.57594	0.61326	0.55188	0.56738	0.54081	0.56005

Table 8. OBDF: Calculated values of the Quemada model.

Calculated Values	WBDF 3		WBDF 3 (aged)		WBDF 4		WBDF 4 (aged)	
	25°C	50°C	25°C	50°C	25°C	50°C	25°C	50°C
χ	0.00958	0.01746	0.00727	0.01527	0.00436	0.00967	0.00373	0.00814
η_F	0.00089	0.00055	0.00089	0.00055	0.00089	0.00055	0.00089	0.00055
Φ	0.139	0.139	0.139	0.139	0.141	0.141	0.141	0.141
ϕ_0	0.13949	0.13986	0.13939	0.13975	0.14121	0.14136	0.14118	0.14135
ϕ_∞	0.22053	0.21641	0.22700	0.21422	0.21398	0.20255	0.21656	0.20213

Table 9. WBDF: Calculated values of the Quemada model.

5.3.4 Infinite- and Zero-Shear Viscosities

When the values of η_∞ and η_0 were treated as theoretical values, and they depended on the viscosity behaviours in the HSR and LSR range, respectively. A more limited range lead to a higher value of η_∞ and a lower value of η_0 . J-curves have linear behaviour at LSRs, i.e. no clear indication when or if the samples reach a zero-shear plateau. By starting the iteration of the model where zero-shear viscosity equalled the highest measured viscosity, the model iterated to the lowest acceptable value of the zero-shear viscosity. However, the linear behaviour yielded an accurate model over a large range of zero-shear viscosity values depending on the initial condition of the curve fitting. Thus, the modelled parameter might be too low compared to the sample's actual behaviour or this behaviour might not exist at all, depending on the existence of yield stress. Determining the infinite- and zero-shear viscosities through empirical curve fitting, yielded the most accurate results when there were indications

of the viscosity moving towards infinite- and zero-shear plateaus, i.e. diverging from linear behaviour.

If the OFITE were utilised, the lower limit of the shear rate range would be 1.7 s^{-1} and the zero-shear viscosity may have decreased as a consequence of the limited shear rate range. However, the model may still have been able to represent the LSRs outside the limited shear rate range of the OFITE. This is shown in Fig. 24, where the model of the entire measured shear rate range is compared to models with a limited shear rate range of $1.62\text{-}1020 \text{ s}^{-1}$. This range is comparable to OFITE 900's range of $1.7\text{-}1022 \text{ s}^{-1}$. The models of the limited shear rate range were curve fitted by weighted least squares (WLS) regression and by reducing RSS. By limiting the shear rate range, the RSS method were not heavily affected by the large difference between the HSR and LSR viscosities. Additionally, it described the LSR range slightly better, as seen in Fig. 24. Exploring the accuracy of the model with a limited shear rate range and a wider selection of drilling fluids can be done in the future.

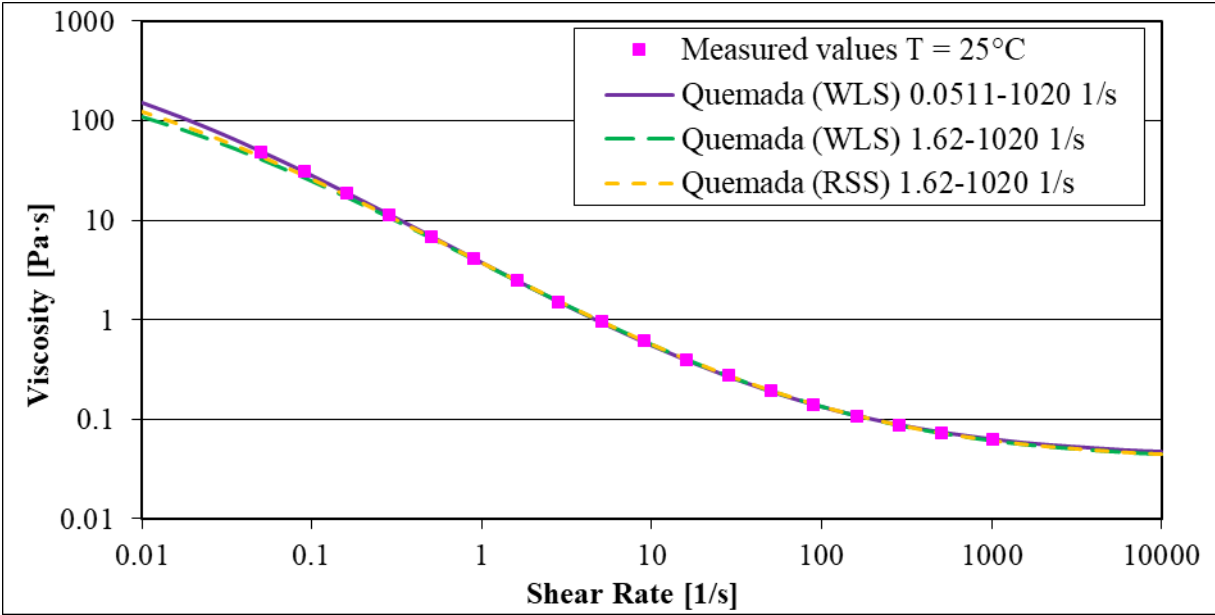


Figure 24. OBDF 1 at 25°C before ageing: Change in Quemada parameters when the shear rate range is shorter, including the difference between curve fitting with weighted least squares (WLS) and residual sum of squares (RSS).

6 Conclusion

The main objective of this thesis was to analyse the use of the Quemada model for predicting the viscous behaviour of drilling fluids. This were done through understanding the rheological properties and behaviours of the drilling fluids, by using the Herschel-Bulkley model as a basis of comparison, and by understanding the Quemada model parameters.

The composition of the fluids decided the rheological behaviours and the rate of viscosity change. Shear stress/shear rate measurements were conducted by two different instruments. By comparing the measurement data obtained by MCR 302 and OFITE 900, MCR 302 proved to be the superior measuring instrument. The drilling fluid measurements showed the desired shear-thinning behaviour, and when the fluids were exposed to simulated well conditions, the measurement results showed a general decrease in the fluid viscosity at elevated temperatures and a general increase in the fluid viscosity after the ageing test.

The characterised rheological behaviours were modelled with Herschel-Bulkley model and Quemada model. The Herschel-Bulkley models, which represented the shear stress of the annular gap, were limited to a shear rate range of $0.0511\text{-}287\text{ s}^{-1}$ to obtain higher model accuracy. The limited shear rate range resulted in models able to describe the characterised rheological behaviours of the fluids with decent accuracy.

The Quemada model were curve fitted to the entire measured shear rate range by reducing WLS. This resulted in a model curves able to represent the entire measured shear rate range with one highly accurate solution for all viscosity profiles. Fitting the Quemada model by reducing RSS resulted in over-estimated viscosity values at HSRs due to the magnitude of the measured viscosity. Thus, curve fitting with WLS improved the model at HSRs, while maintaining the high accuracy at the LSRs.

The infinite- and zero-shear viscosities were treated as curve fitting parameters and were therefore determined by the gradient of the curves. Linear behaviour at LSRs demonstrated a large interval of acceptable zero-shear viscosities. However, most of the curves indicated infinite- and zero-shear plateaus due to the extensive shear rate range. Thus, yielding a good estimation of the infinite- and zero-shear plateaus. The model indicating zero-shear plateaus in most of the viscosity profiles also meant no true yield stress existed.

In this study, the RSS proved to be the superior regression method when modelling a limited shear rate range of $1.62\text{-}1020\text{ s}^{-1}$. It predicted the viscosity values of the LSRs ($0.0511\text{-}1.62\text{ s}^{-1}$) slightly better than the WLS method. Thus, the appropriate regression method must be decided depending on the range of shear rates and the magnitude of the respective viscosities.

The introduction of this thesis explained the importance of understanding the rheological properties and behaviours of drilling fluids in relation to wellbore stability and hole cleaning. The Quemada model proved its ability to model the shear-thinning behaviour of the drilling fluid with improved accuracy in comparison with the traditional Heschel-Bulkley model. Thus, Quemada's (1998) statement that structural models are more appropriate for complex fluids, like drilling fluids, were verified in this study. Having highly accurate models when predicting the rheological behaviours of the fluids, ensures the efficiency of hole cleaning and the safety of the drilling operation.

This thesis was limited to only four drilling fluids, and further studies can be conducted on the Quemada model to confirm its reliability to predict the rheological behaviour of drilling fluids in general.

References

- American Petroleum Institute. (2014). Recommended Practice for Field Testing of Oil-based Drilling Fluids. In *API Recommended Practice 13B-2*. Washington D.C.
- American Petroleum Institute. (2019). Recommended Practice for Field Testing of Water-based Drilling Fluids. In *API Recommended Practice 13B-1*. Washington D.C.
- Anawe, P. A. L., & Folayan, J. A. (2018). Data analyses on temperature-dependent behaviour of water based drilling fluid rheological models. *Data in Brief*, *21*, 289-298. doi:<https://doi.org/10.1016/j.dib.2018.09.100>
- Andaverde, J. A., Wong-Loya, J. A., Vargas-Tabares, Y., & Robles, M. (2019). A practical method for determining the rheology of drilling fluid. *Journal of Petroleum Science and Engineering*, *180*, 150-158. doi:<https://doi.org/10.1016/j.petrol.2019.05.039>
- Anton Paar. (n.d.-a). Basics of Rheology. Retrieved 2020.04.21 from <https://wiki.anton-paar.com/en/basics-of-rheology/>
- Anton Paar. (n.d.-b). How to measure viscosity. Retrieved 2020.03.09 from <https://wiki.anton-paar.com/en/how-to-measure-viscosity/>
- Baldino, S., Osgouei, R. E., Ozbayoglu, E., Miska, S. Z., & May, R. (2018). Quemada model approach to oil or synthetic oil based drilling fluids rheological modelling. *Journal of Petroleum Science and Engineering*, *163*, 27-36. doi:<https://doi.org/10.1016/j.petrol.2017.12.042>
- Balmforth, N., Frigaard, I., & Ovarlez, G. (2014). Yielding to Stress: Recent Developments in Viscoplastic Fluid Mechanics. *Annual Review of Fluid Mechanics*, *46*, 121-146. doi:<https://www.doi.org/10.1146/annurev-fluid-010313-141424>
- Barnes, H. A., & Carnali, J. O. (1990). The vane-in-cup as a novel rheometer geometry for shear thinning and thixotropic materials. *Journal of Rheology*, *34*(6), 841-866. doi:<https://www.doi.org/10.1122/1.550103>
- Barnes, H. A., Hutton, J. F., & Walters, K. (1989). *An Introduction to Rheology*: Elsevier Science.
- Barnes, H. A., & Walters, K. (1985). The yield stress myth? *Rheologica Acta*, *24*(4), 323-326. doi:<https://doi.org/10.1007/BF01333960>
- Bartlett, L. E. (1967). *Effect of Temperature on the Flow Properties of Drilling Fluids*. Paper presented at the Fall Meeting of the Society of Petroleum Engineers of AIME, New Orleans, Louisiana. <https://doi.org/10.2118/1861-MS>
- Blair, G. W. S. (1933). On the Nature of "Yield-Value". *Physics*, *4*(3), 113-118. doi:<https://www.doi.org/10.1063/1.1745163>
- Caenn, R., Darley, H. C. H., & Gray, G. R. (2017). *Composition and Properties of Drilling and Completion Fluids*: Gulf Professional Publishing.
- Chhabra, R. P., & Richardson, J. F. (2008). Chapter 1 - Non-Newtonian Fluid Behaviour. In R. P. Chhabra & J. F. Richardson (Eds.), *Non-Newtonian Flow and Applied Rheology (Second Edition)* (pp. 1-55). Oxford: Butterworth-Heinemann.
- De Visscher, J., & Vanelstraete, A. (2004). Practical test methods for measuring the zero shear viscosity of bituminous binders. *Materials and Structures*, *37*(5), 360-364. doi:<https://doi.org/10.1007/BF02481684>
- Duffy, J. (2012). Ask the Expert: Using Rheology to Design Better Products—Yield Stress and How to Measure It. from <https://www.americanlaboratory.com/914-Application-Notes/117719-Ask-the-Expert-Using-Rheology-to-Design-Better-Products-Yield-Stress-and-How-to-Measure-It/>
- Duffy, J. (2016). Getting the Complete Picture: How to Best Measure a Viscosity Flow Curve. Retrieved May 6, 2020 from <https://www.americanlaboratory.com/914-Application->

- Notes/187241-Getting-the-Complete-Picture-How-to-Best-Measure-a-Viscosity-Flow-Curve/
- Dzuy, N. Q., & Boger, D. V. (1983). Yield Stress Measurement for Concentrated Suspensions. *Journal of Rheology*, 27(4), 321-349. doi:<https://www.doi.org/10.1122/1.549709>
- EngineerExcel. (n.d.). Excel solver: Which solving method should I use? Retrieved 2020.06.13 from <https://engineerexcel.com/excel-solver-solving-method-choose/>
- FrontlineSolvers. (n.d.). Excel solver - Global optimization. Retrieved 2020.06.13 from <https://www.solver.com/excel-solver-global-optimization>
- Fylstra, D., Lasdon, L., Watson, J., & Waren, A. (1998). Design and Use of the Microsoft Excel Solver. *INFORMS Journal on Applied Analytics*, 28(5), 29-55. doi:<https://doi.org/10.1287/inte.28.5.29>
- Ghasem, N. M., & Al-Marzouqi, M. H. (2011). Effects of Shear Rate, Temperature, and Polymer Composition on the Shear Stress of Polyethersulfone/1-Methyl-2-pyrrolidone Cast Solutions. *Journal of Chemical & Engineering Data*, 56(12), 4444-4448. doi:<https://doi.org/10.1021/je2002978>
- Gucuyener, I. H. (1983). *A Rheological Model for Drilling Fluids and Cement Slurries*. Paper presented at the Middle East Oil Technical Conference and Exhibition, Manama, Bahrain. <https://doi.org/10.2118/11487-MS>
- Gucuyener, I. H., Kok, M., & Batmaz, T. (2002). End Effect Evaluation in Rheological Measurement of Drilling Fluids Using Couette Coaxial Cylinder Viscometer. *Energy Sources*, 24, 441-449. doi:<https://doi.org/10.1080/00908310252889942>
- Guillot, D. (1990). A Digest of Rheological Equations. In E. B. Nelson (Ed.), *Developments in Petroleum Science* (Vol. 28, pp. A-1-A-8): Elsevier.
- Halvorsen, H. A., Jordbekk, H., Grelland, S. S., Saasen, A., & Khalifeh, M. (2019). Viscosity of Oil-Based Drilling Fluids. *Annual Transactions - The Nordic Rheology Society*, 27, 77-87.
- Herschel, W. H., & Bulkley, R. (1926). Konsistenzmessungen von Gummi-Benzollösungen. *Kolloid-Zeitschrift*, 39(4), 291-300. doi:<https://doi.org/10.1007/BF01432034>
- Hodne, H., Galta, S., & Saasen, A. (2007). Rheological modelling of cementitious materials using the Quemada model. *Cement and Concrete Research - CEM CONCR RES*, 37, 543-550. doi:<https://doi.org/10.1016/j.cemconres.2006.11.020>
- Lasdon, L. S., Waren, A. D., Jain, A., & Ratner, M. (1978). Design and Testing of a Generalized Reduced Gradient Code for Nonlinear Programming. *ACM Trans. Math. Softw.*, 4(1), 34-50. doi:<https://www.doi.org/10.1145/355769.355773>
- Mezger, T. G. (2006). *The rheology handbook : for users of rotational and oscillatory rheometers* (2nd revised ed. ed.). Hannover: Vincentz.
- Motulsky, H. J., & Christopoulos, A. (2003). *Fitting models to biological data using linear and nonlinear regression. A practical guide to curve fitting*. San Diego CA: GraphPad Software Inc.
- Nelson, A. Z., & Ewoldt, R. H. (2017). Design of yield-stress fluids: a rheology-to-structure inverse problem. *Soft Matter*, 13(41), 7578-7594. doi:<https://doi.org/10.1039/c7sm00758b>
- Nelson, E. B. (1990). *Well cementing*. Amsterdam; New York; New York, NY, USA: Elsevier; Distributors for the United States and Canada, Elsevier Science Pub. Co. Retrieved 2020.06.04 from http://www.123library.org/book_details/?id=41076
- NIST/SEMATECH. (2012). *e-Handbook of Statistical Methods*. Retrieved 2020.06.13. doi:<https://doi.org/10.18434/M32189>
- Nouri, H. H., & Root, P. J. (1971). *A Study of Polymer Solution Rheology, Flow Behavior, and Oil Displacement Processes*. Paper presented at the Fall Meeting of the Society of

- Petroleum Engineers of AIME, New Orleans, Louisiana. <https://doi.org/10.2118/3523-MS>
- OFITE. (2015). Model 900 Viscometer: Instruction Manual. Houston, Texas.
- Quemada, D. (1978). Rheology of concentrated disperse systems III. General features of the proposed non-newtonian model. Comparison with experimental data. *Rheologica Acta*, 17(6), 643-653. doi:<https://www.doi.org/10.1007/BF01522037>
- Quemada, D. (1998). Rheological modelling of complex fluids. I. The concept of effective volume fraction revisited. *European Physical Journal Applied Physics*, 1(1), 119-127. doi:<https://doi.org/10.1051/epjap:1998125>
- Saasen, A., & Ytrehus, J. (2018). Rheological Properties of Drilling Fluids – Use of Dimensionless Shear Rates in Herschel-Bulkley Models and Power-Law Models. *Applied Rheology*. doi:<https://doi.org/10.3933/ApplRheol-28-54515>
- Sayindla, S., Lund, B., Ytrehus, J. D., & Saasen, A. (2017). Hole-cleaning performance comparison of oil-based and water-based drilling fluids. *Journal of Petroleum Science and Engineering*, 159, 49-57. doi:<https://doi.org/10.1016/j.petrol.2017.08.069>
- Schlumberger. (n.d.-a). Oilfield Glossary - Starch. Retrieved 2020.06.15 from <https://www.glossary.oilfield.slb.com/en/Terms/s/starch.aspx>
- Schlumberger. (n.d.-b). Oilfield Glossary - Xanthan Gum. Retrieved 2020.06.15 from https://www.glossary.oilfield.slb.com/en/Terms/x/xanthan_gum.aspx
- Skadsem, H. J., Leulseged, A., & Cayeux, E. (2019). Measurement of Drilling Fluid Rheology and Modeling of Thixotropic Behavior. *Applied Rheology*, 29(1), 1-11. doi:<https://doi.org/10.1515/arh-2019-0001>
- Skadsem, H. J., & Saasen, A. (2019). Concentric cylinder viscometer flows of Herschel-Bulkley fluids. *Applied Rheology*, 29(1), 173-181. doi:<https://www.doi.org/10.1515/arh-2019-0015>
- Spiess, A.-N., & Neumeyer, N. (2010). An evaluation of R2 as an inadequate measure for nonlinear models in pharmacological and biochemical research: a Monte Carlo approach. *BMC Pharmacology*, 10(1), 6. doi:<https://www.doi.org/10.1186/1471-2210-10-6>
- Teymoori, R. N., & Alaskari, M. K. G. (2007). Effects of Salinity, ph and Temperature on CMC Polymer and XC Polymer Performance. *International Journal of Engineering*, 20(3), 283-290. Retrieved from http://www.ije.ir/article_71677.html
- Thermo Scientific. (2005). Chromeleon Tutorial and User Manual. In.
- van der Werff, J. C., & de Kruif, C. G. (1989). Hard-sphere Colloidal Dispersions: The Scaling of Rheological Properties with Particle Size, Volume Fraction, and Shear Rate. *Journal of Rheology*, 33(3), 421-454. doi:<https://www.doi.org/10.1122/1.550062>
- Watson, J. (2004). The Diabolical Case of the Recurring Yield Stress. *Applied Rheology*, 14(1), 40-45.
- Werner, B., Lund, B., Myrseth, V., Saasen, A., & Gyland, K. (2016). *Comparison of Rheological Properties of Oil-Based and KCl Drilling Fluids*.
- Werner, B., Myrseth, V., & Saasen, A. (2017). Viscoelastic properties of drilling fluids and their influence on cuttings transport. *Journal of Petroleum Science and Engineering*, 156, 845-851. doi:<https://doi.org/10.1016/j.petrol.2017.06.063>
- Willamson, D. (2013). The Defining Series: Drilling Fluid Basics. *Oilfield Review*, 25(1). Retrieved from <https://www.slb.com/resource-library/oilfield-review/defining-series/defining-drilling-fluids>

Appendix A – OFITE 900 Measurement Data

OBDF 1 Shear Rate $\dot{\gamma}$ [1/s]	Batch 3 Shear Stress τ [Pa]	Batch 4 Shear Stress τ [Pa]	Batch 3 Viscosity η [Pa·s]	Batch 4 Viscosity η [Pa·s]	APE
1021.38	81.66	81.71	0.0799	0.0800	0.1 %
510.69	48.24	49.11	0.0945	0.0962	1.8 %
340.46	36.08	37.00	0.1060	0.1087	2.5 %
170.23	22.89	23.81	0.1345	0.1399	4.0 %
102.14	16.97	18.09	0.1661	0.1771	6.6 %
51.07	12.11	12.88	0.2371	0.2521	6.3 %
34.05	9.20	9.81	0.2701	0.2881	6.7 %
17.02	8.07	8.74	0.4744	0.5134	8.2 %
10.21	7.00	7.72	0.6857	0.7557	10.2 %
5.11	6.03	6.59	1.1800	1.2900	9.3 %
3.4	5.72	6.18	1.6833	1.8186	8.0 %
1.7	5.21	5.62	3.0660	3.3065	7.8 %
Gel 10 sec.	5.42	5.83	MAPE		5.9 %
Gel 10 min.	6.69	7.36			

Table 10. OFITE 900 measurements of OBDF 1 at $21 \pm 1^\circ\text{C}$ before ageing, incl. gel-strength, APE, and MAPE. The values marked in “red” are the excluded 20 rpm readings.

OBDF 1 Shear Rate $\dot{\gamma}$ [1/s]	Batch 3 Shear Stress τ [Pa]	Batch 4 Shear Stress τ [Pa]	Batch 3 Viscosity η [Pa·s]	Batch 4 Viscosity η [Pa·s]	APE
1021.38	86.72	90.24	0.0849	0.0884	4.1 %
510.69	52.63	55.34	0.1031	0.1084	5.1 %
340.46	39.96	42.00	0.1174	0.1234	5.1 %
170.23	25.65	27.24	0.1507	0.1600	6.2 %
102.14	19.26	20.54	0.1886	0.2011	6.6 %
51.07	13.75	14.72	0.2692	0.2882	7.1 %
34.05	10.83	11.50	0.3182	0.3377	6.1 %
17.02	9.25	10.17	0.5434	0.5975	9.9 %
10.21	8.28	8.79	0.8108	0.8608	6.2 %
5.11	7.05	7.51	1.3800	1.4700	6.5 %
3.4	6.64	-	1.9538	-	-
1.7	6.03	6.23	3.5469	3.6672	3.4 %
Gel 10 sec.	6.18	6.64	MAPE		6.0 %
Gel 10 min.	7.56	7.72			

Table 11. OFITE 900 measurements of OBDF 1 at $21 \pm 1^\circ\text{C}$ after ageing, incl. gel-strength, APE, and MAPE. The values marked in “red” are the excluded 20 rpm readings.

OBDF 1 Shear Rate $\dot{\gamma}$ [1/s]	Batch 3 Shear Stress τ [Pa]	Batch 4 Shear Stress τ [Pa]	Batch 3 Viscosity η [Pa·s]	Batch 4 Viscosity η [Pa·s]	APE
1021.38	39.60	39.70	0.0388	0.0389	0.3 %
510.69	24.32	24.43	0.0476	0.0478	0.4 %
340.46	18.65	18.75	0.0548	0.0551	0.5 %
170.23	12.16	12.32	0.0714	0.0723	1.3 %
102.14	9.25	9.40	0.0906	0.0921	1.7 %
51.07	6.69	6.90	0.1311	0.1351	3.1 %
34.05	5.06	5.26	0.1486	0.1546	4.0 %
17.02	4.65	4.80	0.2732	0.2822	3.3 %
10.21	4.24	4.34	0.4154	0.4254	2.4 %
5.11	3.78	3.88	0.7400	0.7600	2.7 %
3.4	3.58	3.68	1.0521	1.0821	2.9 %
1.7	3.27	3.32	1.9238	1.9538	1.6 %
Gel 10 sec.	3.63	3.78	MAPE		1.8 %
Gel 10 min.	4.34	4.55			

Table 12. OFITE 900 measurements of OBDF 1 at $50 \pm 3^\circ\text{C}$ after ageing, incl. gel-strength, APE, and MAPE. The values marked in “red” are the excluded 20 rpm readings.

OBDF 2 Shear Rate $\dot{\gamma}$ [1/s]	Batch 2 Shear Stress τ [Pa]	Batch 3 Shear Stress τ [Pa]	Batch 2 Viscosity η [Pa·s]	Batch 3 Viscosity η [Pa·s]	APE
1021.38	59.53	59.89	0.0583	0.0586	0.6 %
510.69	35.31	36.08	0.0691	0.0706	2.2 %
340.46	26.32	27.19	0.0773	0.0798	3.3 %
170.23	16.66	17.53	0.0979	0.1030	5.2 %
102.14	12.26	13.23	0.1201	0.1296	7.9 %
51.07	8.69	9.50	0.1701	0.1861	9.4 %
34.05	6.49	7.10	0.1906	0.2086	9.4 %
17.02	5.77	6.13	0.3393	0.3603	6.2 %
10.21	4.96	5.67	0.4855	0.5555	14.4 %
5.11	4.29	4.55	0.8400	0.8900	6.0 %
3.4	3.99	4.39	1.1723	1.2925	10.3 %
1.7	3.58	4.09	2.1041	2.4047	14.3 %
Gel 10 sec.	4.04	4.34	MAPE		6.9 %
Gel 10 min.	4.91	5.67			

Table 13. OFITE 900 measurements of OBDF 2 at $21 \pm 1^\circ\text{C}$ before ageing, incl. gel-strength APE, and MAPE. The “red” values are the excluded 20 rpm readings.

OBDF 2 Shear Rate $\dot{\gamma}$ [1/s]	Batch 2 Shear Stress τ [Pa]	Batch 3 Shear Stress τ [Pa]	Batch 2 Viscosity η [Pa·s]	Batch 3 Viscosity η [Pa·s]	APE
1021.38	62.60	66.63	0.0613	0.0652	6.4 %
510.69	38.33	40.32	0.0750	0.0789	5.2 %
340.46	28.97	30.51	0.0851	0.0896	5.3 %
170.23	18.80	19.78	0.1105	0.1162	5.2 %
102.14	14.10	15.07	0.1381	0.1476	6.9 %
51.07	10.22	10.78	0.2001	0.2111	5.5 %
34.05	7.97	8.48	0.2341	0.2491	6.4 %
17.02	6.85	7.15	0.4023	0.4203	4.5 %
10.21	6.08	6.49	0.5956	0.6356	6.7 %
5.11	5.21	5.67	1.0200	1.1100	8.8 %
3.4	4.96	5.37	1.4579	1.5781	8.2 %
1.7	4.39	4.80	2.5851	2.8255	9.3 %
Gel 10 sec.	4.75	5.16	MAPE		6.4 %
Gel 10 min.	5.67	6.13			

Table 14. OFITE 900 measurements of OBDF 2 at $21 \pm 1^\circ\text{C}$ after ageing, incl. gel-strength APE, and MAPE. The “red” values are the excluded 20 rpm readings.

OBDF 2 Shear Rate $\dot{\gamma}$ [1/s]	Batch 2 Shear Stress τ [Pa]	Batch 3 Shear Stress τ [Pa]	Batch 2 Viscosity η [Pa·s]	Batch 3 Viscosity η [Pa·s]	APE
1021.38	31.22	32.81	0.0306	0.0321	5.1 %
510.69	19.32	20.24	0.0378	0.0396	4.8 %
340.46	14.56	15.23	0.0428	0.0447	4.6 %
170.23	9.71	10.22	0.0570	0.0600	5.3 %
102.14	7.31	7.92	0.0715	0.0775	8.4 %
51.07	5.57	5.93	0.1091	0.1161	6.4 %
34.05	4.09	4.34	0.1201	0.1276	6.3 %
17.02	3.88	4.14	0.2282	0.2432	6.6 %
10.21	3.53	3.73	0.3453	0.3654	5.8 %
5.11	3.01	3.27	0.5900	0.6400	8.5 %
3.4	2.76	3.12	0.8116	0.9168	13.0 %
1.7	2.56	2.76	1.5029	1.6232	8.0 %
Gel 10 sec.	3.12	3.32	MAPE		6.3 %
Gel 10 min.	3.78	3.83			

Table 15. OFITE 900 measurements of OBDF 2 at $50 \pm 1^\circ\text{C}$ after ageing, incl. gel-strength APE, and MAPE. The “red” values are the excluded 20 rpm readings.

WBDF 3 Shear Rate $\dot{\gamma}$ [1/s]	Batch 1 Shear Stress τ [Pa]	Batch 2 Shear Stress τ [Pa]	Batch 1 Viscosity η [Pa·s]	Batch 2 Viscosity η [Pa·s]	APE
1021.38	26.32	27.49	0.0258	0.0269	4.5 %
510.69	17.68	18.40	0.0346	0.0360	4.0 %
340.46	14.10	14.51	0.0414	0.0426	2.9 %
170.23	9.71	10.27	0.0570	0.0603	5.8 %
102.14	7.77	7.92	0.0760	0.0775	2.0 %
51.07	5.67	5.77	0.1111	0.1131	1.8 %
34.05	4.75	4.85	0.1396	0.1426	2.2 %
17.02	3.83	3.83	0.2252	0.2252	0.0 %
10.21	3.27	3.32	0.3203	0.3253	1.6 %
5.11	2.61	2.66	0.5100	0.5200	2.0 %
3.4	2.30	2.35	0.6763	0.6914	2.2 %
1.7	2.04	1.99	1.2024	1.1723	2.5 %
Gel 10 sec.	3.22	3.27	MAPE		2.7 %
Gel 10 min.	4.60	4.75			

Table 16. OFITE 900 measurements of WBDF 3 at $21 \pm 1^\circ\text{C}$ before ageing, incl. gel-strength, APE and MAPE. The “red” values are the excluded 20 rpm readings.

WBDF 3 Shear Rate $\dot{\gamma}$ [1/s]	Batch 1 Shear Stress τ [Pa]	Batch 2 Shear Stress τ [Pa]	Batch 1 Viscosity η [Pa·s]	Batch 2 Viscosity η [Pa·s]	APE
1021.38	25.29	26.52	0.0248	0.0260	4.8 %
510.69	17.48	18.19	0.0342	0.0356	4.1 %
340.46	14.15	14.82	0.0416	0.0435	4.7 %
170.23	10.07	10.58	0.0591	0.0621	5.1 %
102.14	8.12	8.48	0.0795	0.0830	4.4 %
51.07	6.13	6.34	0.1201	0.1241	3.3 %
34.05	5.11	5.21	0.1501	0.1531	2.0 %
17.02	4.34	4.34	0.2552	0.2552	0.0 %
10.21	3.73	3.88	0.3654	0.3804	4.1 %
5.11	3.07	3.12	0.6000	0.6100	1.7 %
3.4	2.76	2.96	0.8116	0.8717	7.4 %
1.7	2.40	2.45	1.4128	1.4428	2.1 %
Gel 10 sec.	3.73	3.83	MAPE		3.8 %
Gel 10 min.	5.01	5.21			

Table 17. OFITE 900 measurements of WBDF 3 at $21 \pm 1^\circ\text{C}$ after ageing, incl. gel-strength, APE and MAPE. The “red” values are the excluded 20 rpm readings.

WBDF 3 Shear Rate $\dot{\gamma}$ [1/s]	Batch 1 Shear Stress τ [Pa]	Batch 2 Shear Stress τ [Pa]	Batch 1 Viscosity η [Pa·s]	Batch 2 Viscosity η [Pa·s]	APE
1021.38	10.83	11.34	0.0106	0.0111	4.7 %
510.69	6.08	6.34	0.0119	0.0124	4.2 %
340.46	4.04	4.34	0.0119	0.0128	7.6 %
170.23	1.33	1.58	0.0078	0.0093	19.2 %
102.14	0.05	0.05	0.0005	0.0005	0.0 %
51.07	0.00	0.00	0.0000	0.0000	-
34.05	0.00	0.00	0.0000	0.0000	-
17.02	0.00	0.00	0.0000	0.0000	-
10.21	0.00	0.00	0.0000	0.0000	-
5.11	0.00	0.00	0.0000	0.0000	-
3.4	0.00	0.00	0.0000	0.0000	-
1.7	0.00	0.00	0.0000	0.0000	-
Gel 10 sec.	0.00	0.00	MAPE		-
Gel 10 min.	0.00	0.00			

Table 18. OFITE 900 measurements of WBDF 3 at $50 \pm 3^\circ\text{C}$ after ageing, incl. gel-strength, APE and MAPE.

Recipe 4 Shear Rate $\dot{\gamma}$ [1/s]	Batch 1 Shear Stress τ [Pa]	Batch 2 Shear Stress τ [Pa]	Batch 1 Viscosity η [Pa·s]	Batch 2 Viscosity η [Pa·s]	APE
1021.38	34.19	34.24	0.0335	0.0335	0.1 %
510.69	23.86	23.71	0.0467	0.0464	0.6 %
340.46	19.42	19.42	0.0570	0.0570	0.0 %
170.23	14.05	14.10	0.0826	0.0829	0.4 %
102.14	11.29	11.29	0.1106	0.1106	0.0 %
51.07	8.69	8.64	0.1701	0.1691	0.6 %
34.05	7.26	7.26	0.2131	0.2131	0.0 %
17.02	5.98	5.93	0.3513	0.3483	0.9 %
10.21	5.26	5.26	0.5155	0.5155	0.0 %
5.11	4.70	4.55	0.9200	0.8900	3.3 %
3.4	4.04	4.04	1.1873	1.1873	0.0 %
1.7	3.47	3.47	2.0440	2.0440	0.0 %
Gel 10 sec.	5.31	5.31		MAPE	0.5 %
Gel 10 min.	7.72	7.72			

Table 19. OFITE 900 measurements of WBDF 4 at $21 \pm 1^\circ\text{C}$ before ageing, incl. gel-strength, APE and MAPE. The “red” values are the excluded 20 rpm readings.

Recipe 4 Shear Rate $\dot{\gamma}$ [1/s]	Batch 1 Shear Stress τ [Pa]	Batch 2 Shear Stress τ [Pa]	Batch 1 Viscosity η [Pa·s]	Batch 2 Viscosity η [Pa·s]	APE
1021.38	33.27	34.08	0.0326	0.0334	2.5 %
510.69	23.76	24.02	0.0465	0.0470	1.1 %
340.46	19.57	19.83	0.0575	0.0582	1.3 %
170.23	14.41	14.61	0.0847	0.0859	1.4 %
102.14	11.86	12.01	0.1161	0.1176	1.3 %
51.07	9.25	9.30	0.1811	0.1821	0.6 %
34.05	8.02	8.02	0.2356	0.2356	0.0 %
17.02	6.59	6.69	0.3873	0.3933	1.6 %
10.21	5.83	5.83	0.5706	0.5706	0.0 %
5.11	5.16	5.16	1.0100	1.0100	0.0 %
3.4	4.75	4.75	1.3977	1.3977	0.0 %
1.7	3.93	4.04	2.3145	2.3746	2.6 %
Gel 10 sec.	5.98	5.98		MAPE	1.1 %
Gel 10 min.	8.69	8.79			

Table 20. OFITE 900 measurements of WBDF 4 at $21 \pm 1^\circ\text{C}$ after ageing, incl. gel-strength, APE and MAPE. The “red” values are the excluded 20 rpm readings.

Recipe 4 Shear Rate $\dot{\gamma}$ [1/s]	Batch 1 Shear Stress τ [Pa]	Batch 2 Shear Stress τ [Pa]	Batch 1 Viscosity η [Pa·s]	Batch 2 Viscosity η [Pa·s]	APE
1021.38	17.17	17.02	0.0168	0.0167	0.9 %
510.69	10.99	10.88	0.0215	0.0213	0.9 %
340.46	8.43	8.12	0.0248	0.0239	3.6 %
170.23	5.06	4.96	0.0297	0.0291	2.0 %
102.14	3.27	3.17	0.0320	0.0310	3.1 %
51.07	1.43	1.23	0.0280	0.0240	14.3 %
34.05	0.26	0.20	0.0075	0.0060	20.0 %
17.02	0.00	0.00	0.0000	0.0000	-
10.21	0.00	0.00	0.0000	0.0000	-
5.11	0.00	0.00	0.0000	0.0000	-
3.4	0.00	0.00	0.0000	0.0000	-
1.7	0.00	0.00	0.0000	0.0000	-
Gel 10 sec.	0.00	0.00		MAPE	-
Gel 10 min.	0.00	0.00			

Table 21. OFITE 900 measurements of WBDF 4 at $50 \pm 2^\circ\text{C}$ after ageing, incl. gel-strength, APE and MAPE. The “red” values are the excluded 20 rpm readings.

Appendix B – Anton Paar MCR 302 Measurement Data

OBDF 1	25°C			50°C			25°C (aged)			50°C (aged)		
	Batch 3	Batch 4	APE	Batch 3	Batch 4	APE	Batch 3	Batch 4	APE	Batch 3	Batch 4	APE
	Shear Stress τ [Pa]			Shear Stress τ [Pa]			Shear Stress τ [Pa]			Shear Stress τ [Pa]		
1020	63	65.7	4.3 %	35.1	36.7	4.6 %	68.50	71.00	3.6 %	37.80	39.40	4.2 %
511	36.3	38.3	5.5 %	20.1	21.2	5.5 %	40.20	42.00	4.5 %	21.90	23.00	5.0 %
287	24.4	25.9	6.1 %	13.6	14.4	5.9 %	27.30	28.60	4.8 %	14.90	15.70	5.4 %
162	17.1	18.3	7.0 %	9.7	10.3	6.2 %	19.40	20.40	5.2 %	10.70	11.30	5.6 %
90.9	12.6	13.5	7.1 %	7.24	7.73	6.8 %	14.30	15.20	6.3 %	8.00	8.50	6.3 %
51.1	9.66	10.4	7.7 %	5.64	6.04	7.1 %	11.10	11.80	6.3 %	6.26	6.67	6.5 %
28.7	7.72	8.37	8.4 %	4.57	4.91	7.4 %	8.89	9.49	6.7 %	5.10	5.45	6.9 %
16.2	6.39	6.96	8.9 %	3.83	4.12	7.6 %	7.41	7.93	7.0 %	4.30	4.60	7.0 %
9.09	5.46	5.97	9.3 %	3.31	3.57	7.9 %	6.37	6.83	7.2 %	3.74	4.00	7.0 %
5.11	4.8	5.26	9.6 %	2.93	3.17	8.2 %	5.62	6.04	7.5 %	3.33	3.57	7.2 %
2.87	4.31	4.74	10.0 %	2.65	2.87	8.3 %	5.07	5.45	7.5 %	3.03	3.24	6.9 %
1.62	3.95	4.34	9.9 %	2.44	2.64	8.2 %	4.65	5.00	7.5 %	2.80	3.00	7.1 %
0.909	3.66	4.03	10.1 %	2.27	2.46	8.4 %	4.31	4.64	7.7 %	2.61	2.79	6.9 %
0.511	3.42	3.78	10.5 %	2.13	2.32	8.9 %	4.03	4.33	7.4 %	2.46	2.62	6.5 %
0.287	3.21	3.56	10.9 %	2.01	2.19	9.0 %	3.78	4.05	7.1 %	2.32	2.47	6.5 %
0.162	3.01	3.35	11.3 %	1.89	2.07	9.5 %	3.53	3.76	6.5 %	2.19	2.31	5.5 %
0.0909	2.77	3.13	13.0 %	1.77	1.96	10.7 %	3.25	3.43	5.5 %	2.05	2.14	4.4 %
0.0511	2.45	2.89	18.0 %	1.62	1.84	13.6 %	2.90	2.97	2.4 %	1.91	1.92	0.5 %

Table 22. MCR 302 measurements of OBDF 1 including APE.

OBDF 2 Shear Rate $\dot{\gamma}$ [1/s]	25°C			50°C			25°C (aged)			50°C (aged)		
	Batch 3	Batch 4	APE	Batch 3	Batch 4	APE	Batch 3	Batch 4	APE	Batch 3	Batch 4	APE
	Shear Stress τ [Pa]			Shear Stress τ [Pa]			Shear Stress τ [Pa]			Shear Stress τ [Pa]		
1020	47.30	49.90	5.5 %	27.80	28.60	2.9 %	50.20	53.00	5.6 %	29.60	29.90	1.0 %
511	27.00	28.50	5.6 %	15.90	16.40	3.1 %	29.30	30.80	5.1 %	17.20	17.40	1.2 %
287	18.10	19.00	5.0 %	10.80	11.10	2.8 %	20.00	20.90	4.5 %	11.80	12.00	1.7 %
162	12.70	13.40	5.5 %	7.76	7.96	2.6 %	14.30	14.90	4.2 %	8.60	8.71	1.3 %
90.9	9.31	9.86	5.9 %	5.83	5.98	2.6 %	10.70	11.10	3.7 %	6.54	6.63	1.4 %
51.1	7.14	7.58	6.2 %	4.57	4.69	2.6 %	8.32	8.65	4.0 %	5.19	5.27	1.5 %
28.7	5.69	6.07	6.7 %	3.72	3.82	2.7 %	6.74	7.01	4.0 %	4.27	4.35	1.9 %
16.2	4.70	5.04	7.2 %	3.13	3.22	2.9 %	5.64	5.88	4.3 %	3.63	3.71	2.2 %
9.09	4.00	4.32	8.0 %	2.72	2.80	2.9 %	4.86	5.09	4.7 %	3.17	3.25	2.5 %
5.11	3.51	3.81	8.5 %	2.41	2.49	3.3 %	4.30	4.51	4.9 %	2.84	2.91	2.5 %
2.87	3.14	3.43	9.2 %	2.19	2.27	3.7 %	3.88	4.09	5.4 %	2.58	2.66	3.1 %
1.62	2.87	3.15	9.8 %	2.02	2.10	4.0 %	3.55	3.76	5.9 %	2.38	2.46	3.4 %
0.909	2.66	2.94	10.5 %	1.88	1.96	4.3 %	3.28	3.49	6.4 %	2.22	2.30	3.6 %
0.511	2.49	2.76	10.8 %	1.77	1.85	4.5 %	3.05	3.27	7.2 %	2.08	2.16	3.8 %
0.287	2.35	2.61	11.1 %	1.67	1.75	4.8 %	2.85	3.06	7.4 %	1.95	2.03	4.1 %
0.162	2.21	2.46	11.3 %	1.58	1.66	5.1 %	2.65	2.85	7.5 %	1.82	1.89	3.8 %
0.0909	2.08	2.32	11.5 %	1.49	1.56	4.7 %	2.44	2.62	7.4 %	1.69	1.74	3.0 %
0.0511	1.95	2.16	10.8 %	1.39	1.45	4.3 %	2.19	2.34	6.8 %	1.54	1.54	0.0 %

Table 23. MCR 302 measurements of OBDF 2 including APE.

WBDF 3 Shear Rate $\dot{\gamma}$ [1/s]	25°C			50°C			25°C (aged)			50°C (aged)		
	Batch 3	Batch 4	APE	Batch 3	Batch 4	APE	Batch 3	Batch 4	APE	Batch 3	Batch 4	APE
	Shear Stress τ [Pa]			Shear Stress τ [Pa]			Shear Stress τ [Pa]			Shear Stress τ [Pa]		
1020	23.80	24.40	2.5 %	17.00	17.30	1.8 %	23.80	24.50	2.9 %	17.50	17.90	2.3 %
511	14.70	15.10	2.7 %	10.80	10.90	0.9 %	15.10	15.40	2.0 %	11.30	11.50	1.8 %
287	10.50	10.80	2.9 %	7.90	7.95	0.6 %	11.00	11.20	1.8 %	8.41	8.54	1.5 %
162	7.88	8.02	1.8 %	6.04	6.06	0.3 %	8.41	8.55	1.7 %	6.56	6.65	1.4 %
90.9	6.08	6.16	1.3 %	4.75	4.75	0.0 %	6.65	6.73	1.2 %	5.27	5.32	0.9 %
51.1	4.81	4.86	1.0 %	3.81	3.80	0.3 %	5.38	5.43	0.9 %	4.32	4.35	0.7 %
28.7	3.87	3.91	1.0 %	3.08	3.07	0.3 %	4.43	4.47	0.9 %	3.58	3.60	0.6 %
16.2	3.17	3.20	0.9 %	2.51	2.50	0.4 %	3.71	3.74	0.8 %	2.98	3.00	0.7 %
9.09	2.63	2.64	0.4 %	2.05	2.05	0.0 %	3.13	3.15	0.6 %	2.49	2.51	0.8 %
5.11	2.19	2.20	0.5 %	1.66	1.67	0.6 %	2.66	2.68	0.8 %	2.07	2.09	1.0 %
2.87	1.83	1.84	0.5 %	1.34	1.35	0.7 %	2.27	2.29	0.9 %	1.70	1.73	1.8 %
1.62	1.53	1.54	0.7 %	1.07	1.08	0.9 %	1.93	1.95	1.0 %	1.38	1.41	2.2 %
0.909	1.27	1.28	0.8 %	0.84	0.86	2.3 %	1.64	1.66	1.2 %	1.11	1.15	3.6 %
0.511	1.05	1.07	1.9 %	0.66	0.68	3.5 %	1.38	1.41	2.2 %	0.88	0.92	4.7 %
0.287	0.86	0.88	1.7 %	0.50	0.53	5.0 %	1.15	1.18	2.6 %	0.68	0.72	6.2 %
0.162	0.70	0.71	2.4 %	0.38	0.40	6.6 %	0.95	0.98	3.1 %	0.52	0.56	8.2 %
0.0909	0.55	0.57	3.5 %	0.28	0.30	8.7 %	0.76	0.80	4.2 %	0.38	0.42	10.0 %
0.0511	0.43	0.45	4.4 %	0.20	0.22	11.0 %	0.61	0.64	5.3 %	0.28	0.31	12.3 %

Table 24. MCR 302 measurements of WBDF 3 including APE.

WBDF 4 Shear Rate $\dot{\gamma}$ [1/s]	25°C			50°C			25°C (aged)			50°C (aged)		
	Batch 3	Batch 4	APE	Batch 3	Batch 4	APE	Batch 3	Batch 4	APE	Batch 3	Batch 4	APE
	Shear Stress τ [Pa]			Shear Stress τ [Pa]			Shear Stress τ [Pa]			Shear Stress τ [Pa]		
1020	30.40	30.20	0.7 %	22.10	21.90	0.9 %	30.10	29.90	0.7 %	22.4	22.3	0.4 %
511	20.00	19.80	1.0 %	14.80	14.60	1.4 %	20.10	20.00	0.5 %	15.3	15.2	0.7 %
287	14.90	14.70	1.3 %	11.30	11.20	0.9 %	15.30	15.20	0.7 %	11.9	11.8	0.8 %
162	11.50	11.30	1.7 %	8.99	8.83	1.8 %	12.00	11.90	0.8 %	9.55	9.47	0.8 %
90.9	9.12	8.99	1.4 %	7.31	7.16	2.1 %	9.74	9.65	0.9 %	7.88	7.81	0.9 %
51.1	7.43	7.30	1.7 %	6.05	5.92	2.1 %	8.07	8.00	0.9 %	6.62	6.56	0.9 %
28.7	6.16	6.04	1.9 %	5.08	4.96	2.4 %	6.82	6.75	1.0 %	5.63	5.59	0.7 %
16.2	5.19	5.08	2.1 %	4.29	4.18	2.6 %	5.84	5.78	1.0 %	4.83	4.8	0.6 %
9.09	4.42	4.32	2.3 %	3.64	3.55	2.5 %	5.06	5.01	1.0 %	4.17	4.14	0.7 %
5.11	3.81	3.71	2.6 %	3.10	3.01	2.9 %	4.41	4.37	0.9 %	3.59	3.58	0.3 %
2.87	3.29	3.21	2.4 %	2.63	2.55	3.0 %	3.87	3.84	0.8 %	3.09	3.08	0.3 %
1.62	2.85	2.77	2.8 %	2.21	2.14	3.2 %	3.39	3.37	0.6 %	2.64	2.64	0.0 %
0.909	2.48	2.40	3.2 %	1.85	1.79	3.2 %	2.98	2.96	0.7 %	2.24	2.25	0.4 %
0.511	2.14	2.07	3.3 %	1.54	1.49	3.2 %	2.61	2.60	0.4 %	1.88	1.89	0.5 %
0.287	1.84	1.78	3.3 %	1.26	1.22	3.2 %	2.27	2.27	0.0 %	1.56	1.58	1.3 %
0.162	1.57	1.52	3.2 %	1.02	0.99	3.4 %	1.96	1.96	0.0 %	1.27	1.29	1.6 %
0.0909	1.32	1.27	3.8 %	0.81	0.78	3.6 %	1.66	1.67	0.6 %	1.01	1.03	2.0 %
0.0511	1.09	1.04	4.6 %	0.63	0.60	3.7 %	1.39	1.40	0.7 %	0.776	0.798	2.8 %

Table 25. MCR 302 measurements of WBDF 4 including APE.

Appendix C – Herschel-Bulkley Model Values

OBDF 1	25°C			50°C			25°C (aged)			50°C (aged)		
	Measured $\dot{\gamma}$ [1/s] τ [Pa]	HB* τ [Pa]	APE	Measured τ [Pa]	HB* τ [Pa]	APE	Measured τ [Pa]	HB* τ [Pa]	APE	Measured τ [Pa]	HB* τ [Pa]	APE
1020	63.00	62.85	0.2 %	35.10	35.00	0.3 %	68.50	68.35	0.2 %	37.80	37.71	0.2 %
511	36.30	36.87	1.6 %	20.10	20.46	1.8 %	40.20	40.76	1.4 %	21.90	22.26	1.7 %
HSR 287	24.40	23.90	2.0 %	13.60	13.30	2.2 %	27.30	26.80	1.8 %	14.90	14.60	2.0 %
LSR 162	17.10	17.67	3.3 %	9.70	9.98	2.9 %	19.40	19.94	2.8 %	10.70	10.97	2.6 %
90.9	12.60	13.38	6.2 %	7.24	7.64	5.5 %	14.30	15.22	6.4 %	8.00	8.42	5.3 %
51.1	9.66	10.28	6.4 %	5.64	5.95	5.4 %	11.10	11.78	6.1 %	6.26	6.58	5.1 %
28.7	7.72	8.02	3.9 %	4.57	4.71	3.1 %	8.89	9.26	4.2 %	5.10	5.24	2.8 %
16.2	6.39	6.39	0.0 %	3.83	3.82	0.2 %	7.41	7.44	0.4 %	4.30	4.28	0.4 %
9.09	5.46	5.20	4.8 %	3.31	3.17	4.3 %	6.37	6.09	4.3 %	3.74	3.58	4.3 %
5.11	4.80	4.33	9.7 %	2.93	2.69	8.1 %	5.62	5.11	9.0 %	3.33	3.07	7.8 %
2.87	4.31	3.70	14.1 %	2.65	2.35	11.5 %	5.07	4.39	13.3 %	3.03	2.70	10.9 %
1.62	3.95	3.25	17.7 %	2.44	2.10	14.0 %	4.65	3.87	16.7 %	2.80	2.44	13.0 %
0.909	3.66	2.92	20.3 %	2.27	1.91	15.7 %	4.31	3.49	19.0 %	2.61	2.24	14.2 %
0.511	3.42	2.68	21.7 %	2.13	1.78	16.4 %	4.03	3.21	20.3 %	2.46	2.10	14.6 %
0.287	3.21	2.50	22.0 %	2.01	1.68	16.2 %	3.78	3.01	20.5 %	2.32	2.00	13.9 %
0.162	3.01	2.38	21.0 %	1.89	1.61	14.6 %	3.53	2.86	19.1 %	2.19	1.92	12.1 %
0.0909	2.77	2.28	17.5 %	1.77	1.56	11.7 %	3.25	2.75	15.5 %	2.05	1.87	8.7 %
0.0511	2.45	2.22	9.5 %	1.62	1.53	5.8 %	2.90	2.67	8.0 %	1.91	1.83	4.1 %

Table 26. Measured and *Herschel-Bulkley model shear stress of OBDF 1.

OBDF 2	25°C			50°C			25°C (aged)			50°C (aged)		
	Shear Rate $\dot{\gamma}$ [1/s]	Measured τ [Pa]	HB* τ [Pa]	APE	Measured τ [Pa]	HB* τ [Pa]	APE	Measured τ [Pa]	HB* τ [Pa]	APE	Measured τ [Pa]	HB* τ [Pa]
1020	47.30	47.19	0.2 %	27.80	27.72	0.3 %	50.20	50.07	0.3 %	29.60	29.52	0.3 %
511	27.00	27.44	1.6 %	15.90	16.20	1.9 %	29.30	29.79	1.7 %	17.20	17.52	1.9 %
HSR 287	18.10	17.72	2.1 %	10.80	10.53	2.5 %	20.00	19.58	2.1 %	11.80	11.52	2.3 %
LSR 162	12.70	13.05	2.7 %	7.76	7.97	2.7 %	14.30	14.72	3.0 %	8.60	8.83	2.7 %
90.9	9.31	9.75	4.7 %	5.83	6.12	4.9 %	10.70	11.34	6.0 %	6.54	6.92	5.9 %
51.1	7.14	7.43	4.0 %	4.57	4.78	4.6 %	8.32	8.85	6.4 %	5.19	5.51	6.1 %
28.7	5.69	5.78	1.5 %	3.72	3.81	2.5 %	6.74	7.02	4.1 %	4.27	4.45	4.2 %
16.2	4.70	4.62	1.7 %	3.13	3.12	0.5 %	5.64	5.67	0.6 %	3.63	3.67	1.0 %
9.09	4.00	3.79	5.3 %	2.72	2.60	4.3 %	4.86	4.67	3.9 %	3.17	3.07	3.0 %
5.11	3.51	3.20	8.7 %	2.41	2.24	7.3 %	4.30	3.94	8.5 %	2.84	2.64	7.2 %
2.87	3.14	2.79	11.2 %	2.19	1.97	10.2 %	3.88	3.39	12.6 %	2.58	2.31	10.5 %
1.62	2.87	2.50	13.0 %	2.02	1.77	12.2 %	3.55	2.99	15.6 %	2.38	2.07	13.2 %
0.909	2.66	2.29	14.0 %	1.88	1.63	13.1 %	3.28	2.70	17.7 %	2.22	1.88	15.2 %
0.511	2.49	2.14	14.0 %	1.77	1.53	13.5 %	3.05	2.48	18.7 %	2.08	1.75	16.0 %
0.287	2.35	2.04	13.3 %	1.67	1.46	12.8 %	2.85	2.32	18.6 %	1.95	1.64	15.6 %
0.162	2.21	1.96	11.2 %	1.58	1.40	11.2 %	2.65	2.20	16.9 %	1.82	1.57	13.7 %
0.0909	2.08	1.91	8.2 %	1.49	1.36	8.4 %	2.44	2.11	13.3 %	1.69	1.51	10.5 %
0.0511	1.95	1.87	3.9 %	1.39	1.34	3.9 %	2.19	2.05	6.4 %	1.54	1.47	4.5 %

Table 27. Measured and *Herschel-Bulkley model shear stress of OBDF 2.

WBDF 3	25°C			50°C			25°C (aged)			50°C (aged)		
Shear Rate $\dot{\gamma}$ [1/s]	Measured τ [Pa]	HB* τ [Pa]	APE	Measured τ [Pa]	HB* τ [Pa]	APE	Measured τ [Pa]	HB* τ [Pa]	APE	Measured τ [Pa]	HB* τ [Pa]	APE
1020	23.80	23.72	0.4 %	17.00	16.93	0.4 %	23.80	23.71	0.4 %	17.50	17.42	0.4 %
511	14.70	15.00	2.0 %	10.80	11.03	2.1 %	15.10	15.39	1.9 %	11.30	11.55	2.3 %
HSR 287	10.50	10.26	2.3 %	7.90	7.72	2.3 %	11.00	10.77	2.1 %	8.41	8.21	2.3 %
LSR 162	7.88	8.04	2.0 %	6.04	6.16	2.0 %	8.41	8.59	2.1 %	6.56	6.69	2.0 %
90.9	6.08	6.34	4.2 %	4.75	4.88	2.7 %	6.65	6.93	4.2 %	5.27	5.42	2.8 %
51.1	4.81	5.01	4.2 %	3.81	3.87	1.6 %	5.38	5.61	4.2 %	4.32	4.40	1.7 %
28.7	3.87	3.98	2.7 %	3.08	3.08	0.1 %	4.43	4.55	2.8 %	3.58	3.57	0.3 %
16.2	3.17	3.17	0.1 %	2.51	2.45	2.3 %	3.71	3.72	0.2 %	2.98	2.91	2.4 %
9.09	2.63	2.54	3.5 %	2.05	1.96	4.6 %	3.13	3.04	2.7 %	2.49	2.37	4.8 %
5.11	2.19	2.04	6.7 %	1.66	1.56	5.7 %	2.66	2.51	5.7 %	2.07	1.94	6.4 %
2.87	1.83	1.66	9.5 %	1.34	1.26	6.3 %	2.27	2.08	8.3 %	1.70	1.59	6.5 %
1.62	1.53	1.36	11.4 %	1.07	1.01	5.2 %	1.93	1.74	9.6 %	1.38	1.31	5.0 %
0.909	1.27	1.12	11.9 %	0.84	0.82	2.3 %	1.64	1.47	10.3 %	1.11	1.08	2.4 %
0.511	1.05	0.93	11.0 %	0.66	0.67	2.0 %	1.38	1.26	9.0 %	0.88	0.90	2.6 %
0.287	0.86	0.79	8.4 %	0.50	0.55	9.2 %	1.15	1.08	5.9 %	0.68	0.75	10.5 %
0.162	0.70	0.68	2.6 %	0.38	0.46	20.8 %	0.95	0.95	0.5 %	0.52	0.64	23.5 %
0.0909	0.55	0.59	7.1 %	0.28	0.38	37.4 %	0.76	0.83	9.3 %	0.38	0.54	41.8 %
0.0511	0.43	0.52	21.3 %	0.20	0.32	60.8 %	0.61	0.75	23.5 %	0.28	0.46	67.2 %

Table 28. Measured and *Herschel-Bulkley model shear stress of WBDF 3.

OBDF 4	25°C			50°C			25°C (aged)			50°C (aged)		
Shear Rate $\dot{\gamma}$ [1/s]	Measured τ [Pa]	HB* τ [Pa]	APE	Measured τ [Pa]	HB* τ [Pa]	APE	Measured τ [Pa]	HB* τ [Pa]	APE	Measured τ [Pa]	HB* τ [Pa]	APE
1020	30.40	30.30	0.3 %	22.10	22.00	0.4 %	30.10	29.98	0.4 %	22.40	22.30	0.5 %
511	20.00	20.33	1.7 %	14.80	15.11	2.1 %	20.10	20.49	1.9 %	15.30	15.63	2.2 %
HSR 287	14.90	14.65	1.7 %	11.30	11.07	2.0 %	15.30	15.00	1.9 %	11.90	11.66	2.1 %
LSR 162	11.50	11.70	1.8 %	8.99	9.13	1.5 %	12.00	12.22	1.9 %	9.55	9.72	1.8 %
90.9	9.12	9.50	4.1 %	7.31	7.50	2.6 %	9.74	10.10	3.7 %	7.88	8.10	2.8 %
51.1	7.43	7.74	4.2 %	6.05	6.18	2.2 %	8.07	8.39	4.0 %	6.62	6.78	2.4 %
28.7	6.16	6.34	2.9 %	5.08	5.11	0.5 %	6.82	7.00	2.6 %	5.63	5.68	0.9 %
16.2	5.19	5.23	0.8 %	4.29	4.24	1.2 %	5.84	5.88	0.7 %	4.83	4.78	1.1 %
9.09	4.42	4.33	2.0 %	3.64	3.52	3.2 %	5.06	4.96	1.9 %	4.17	4.03	3.4 %
5.11	3.81	3.62	5.0 %	3.10	2.94	5.1 %	4.41	4.22	4.2 %	3.59	3.41	5.0 %
2.87	3.29	3.05	7.3 %	2.63	2.47	6.1 %	3.87	3.62	6.4 %	3.09	2.90	6.2 %
1.62	2.85	2.60	8.8 %	2.21	2.09	5.6 %	3.39	3.14	7.5 %	2.64	2.48	6.1 %
0.909	2.48	2.23	9.9 %	1.85	1.77	4.2 %	2.98	2.74	8.1 %	2.24	2.13	5.0 %
0.511	2.14	1.94	9.2 %	1.54	1.52	1.5 %	2.61	2.42	7.3 %	1.88	1.84	2.1 %
0.287	1.84	1.71	7.0 %	1.26	1.31	3.9 %	2.27	2.16	4.9 %	1.56	1.60	2.8 %
0.162	1.57	1.53	2.7 %	1.02	1.14	11.8 %	1.96	1.95	0.6 %	1.27	1.41	10.9 %
0.0909	1.32	1.38	4.5 %	0.81	1.00	24.3 %	1.66	1.78	7.1 %	1.01	1.25	23.3 %
0.0511	1.09	1.26	15.8 %	0.63	0.89	41.9 %	1.39	1.64	17.9 %	0.78	1.11	43.2 %

Table 29. Measured and *Herschel-Bulkley model shear stress of WBDF 4.

Appendix D – Quemada Model Values

OBDF 1	25°C			50°C			25°C (aged)			50°C (aged)		
	Shear Rate $\dot{\gamma}$ [1/s]	Measured η [Pa·s]	Quemada η [Pa·s]	APE	Measured η [Pa·s]	Quemada η [Pa·s]	APE	Measured η [Pa·s]	Quemada η [Pa·s]	APE	Measured η [Pa·s]	Quemada η [Pa·s]
1020	0.0618	0.0629	1.8 %	0.0344	0.0331	3.9 %	0.0672	0.0679	1.1 %	0.0371	0.0346	6.7 %
511	0.0710	0.0739	4.0 %	0.0393	0.0399	1.4 %	0.0787	0.0808	2.7 %	0.0429	0.0424	1.1 %
287	0.0850	0.0877	3.2 %	0.0474	0.0485	2.3 %	0.0951	0.0972	2.2 %	0.0519	0.0522	0.6 %
162	0.106	0.108	2.4 %	0.0599	0.0612	2.2 %	0.120	0.121	1.3 %	0.0660	0.0668	1.1 %
90.9	0.139	0.139	0.6 %	0.0796	0.0807	1.3 %	0.157	0.158	0.7 %	0.088	0.089	1.3 %
51.1	0.189	0.188	0.7 %	0.110	0.111	0.4 %	0.217	0.216	0.7 %	0.123	0.124	1.1 %
28.7	0.269	0.264	1.8 %	0.159	0.159	0.4 %	0.310	0.306	1.1 %	0.178	0.179	0.7 %
16.2	0.394	0.386	2.1 %	0.236	0.235	0.7 %	0.457	0.451	1.3 %	0.265	0.267	0.5 %
9.09	0.601	0.589	2.0 %	0.364	0.361	0.9 %	0.701	0.691	1.4 %	0.411	0.412	0.1 %
5.11	0.939	0.924	1.6 %	0.573	0.569	0.7 %	1.10	1.09	1.0 %	0.652	0.652	0.0 %
2.87	1.50	1.49	0.8 %	0.923	0.919	0.4 %	1.77	1.76	0.6 %	1.06	1.05	0.1 %
1.62	2.44	2.44	0.1 %	1.51	1.50	0.1 %	2.87	2.87	0.0 %	1.73	1.73	0.1 %
0.909	4.03	4.05	0.6 %	2.50	2.50	0.2 %	4.74	4.77	0.5 %	2.87	2.87	0.1 %
0.511	6.69	6.76	1.0 %	4.17	4.18	0.4 %	7.89	7.94	0.7 %	4.81	4.81	0.1 %
0.287	11.18	11.3	0.7 %	7.00	7.02	0.2 %	13.2	13.2	0.4 %	8.08	8.08	0.0 %
0.162	18.6	18.5	0.2 %	11.7	11.7	0.1 %	21.8	21.8	0.1 %	13.5	13.5	0.1 %
0.0909	30.5	30.2	0.8 %	19.5	19.4	0.4 %	35.8	35.6	0.5 %	22.6	22.6	0.1 %
0.0511	47.9	48.1	0.3 %	31.7	31.7	0.1 %	56.8	56.9	0.2 %	37.4	37.4	0.0 %

Table 30. Measured and Quemada model viscosity of OBDF 1.

OBDF 2 Shear Rate $\dot{\gamma}$ [1/s]	25°C			50°C			25°C (aged)			50°C (aged)		
	Measured η [Pa·s]	Quemada η [Pa·s]	APE	Measured η [Pa·s]	Quemada η [Pa·s]	APE	Measured η [Pa·s]	Quemada η [Pa·s]	APE	Measured η [Pa·s]	Quemada η [Pa·s]	APE
1020	0.0464	0.0439	5.3 %	0.0273	0.0254	7.0 %	0.0492	0.0480	2.5 %	0.0290	0.0273	6.0 %
511	0.0528	0.0527	0.3 %	0.0311	0.0310	0.3 %	0.0573	0.0581	1.3 %	0.0337	0.0337	0.2 %
287	0.0631	0.0636	0.8 %	0.0376	0.0382	1.5 %	0.0697	0.0708	1.7 %	0.0411	0.0419	2.0 %
162	0.078	0.080	1.4 %	0.0479	0.0488	1.8 %	0.0883	0.0897	1.6 %	0.0531	0.0541	1.9 %
90.9	0.102	0.104	1.3 %	0.0641	0.0650	1.4 %	0.118	0.119	0.7 %	0.0719	0.0730	1.4 %
51.1	0.140	0.141	0.8 %	0.0894	0.0901	0.8 %	0.163	0.163	0.2 %	0.102	0.102	0.7 %
28.7	0.198	0.199	0.3 %	0.130	0.130	0.3 %	0.235	0.234	0.5 %	0.149	0.149	0.2 %
16.2	0.290	0.290	0.1 %	0.193	0.193	0.1 %	0.348	0.346	0.6 %	0.224	0.224	0.1 %
9.09	0.440	0.440	0.0 %	0.299	0.298	0.4 %	0.535	0.531	0.7 %	0.349	0.348	0.3 %
5.11	0.687	0.685	0.2 %	0.472	0.471	0.1 %	0.841	0.836	0.7 %	0.556	0.553	0.5 %
2.87	1.09	1.09	0.0 %	0.763	0.761	0.3 %	1.35	1.35	0.5 %	0.899	0.897	0.2 %
1.62	1.77	1.77	0.0 %	1.25	1.24	0.2 %	2.19	2.19	0.1 %	1.47	1.47	0.0 %
0.909	2.93	2.93	0.0 %	2.07	2.07	0.1 %	3.61	3.62	0.3 %	2.44	2.44	0.0 %
0.511	4.87	4.87	0.0 %	3.46	3.46	0.0 %	5.97	6.00	0.5 %	4.07	4.07	0.0 %
0.287	8.19	8.17	0.3 %	5.82	5.83	0.2 %	9.93	10.0	0.2 %	6.79	6.80	0.1 %
0.162	13.6	13.7	0.1 %	9.75	9.76	0.1 %	16.4	16.4	0.0 %	11.2	11.3	0.2 %
0.0909	22.9	22.9	0.1 %	16.4	16.4	0.1 %	26.8	26.7	0.4 %	18.6	18.6	0.2 %
0.0511	38.2	38.1	0.0 %	27.2	27.2	0.0 %	42.9	42.9	0.2 %	30.1	30.2	0.0 %

Table 31. Measured and Quemada model viscosity of OBDF 2.

WBDF 3	25°C			50°C			25°C (aged)			50°C (aged)		
	Shear Rate $\dot{\gamma}$ [1/s]	Measured η [Pa·s]	Quemada η [Pa·s]	APE	Measured η [Pa·s]	Quemada η [Pa·s]	APE	Measured η [Pa·s]	Quemada η [Pa·s]	APE	Measured η [Pa·s]	Quemada η [Pa·s]
1020	0.0233	0.0216	7.5 %	0.0167	0.0165	0.9 %	0.0233	0.0216	7.3 %	0.0172	0.0172	0.2 %
511	0.0288	0.0285	0.8 %	0.0211	0.0222	5.0 %	0.0295	0.0293	0.9 %	0.0221	0.0235	6.1 %
287	0.0366	0.0371	1.5 %	0.0275	0.0292	6.1 %	0.0383	0.0389	1.5 %	0.0293	0.0314	7.0 %
162	0.0486	0.0495	1.8 %	0.0373	0.0393	5.3 %	0.0519	0.0530	2.1 %	0.0405	0.0429	5.9 %
90.9	0.0669	0.0679	1.6 %	0.0523	0.0540	3.4 %	0.0732	0.0743	1.5 %	0.0580	0.0602	3.9 %
51.1	0.0941	0.0951	1.1 %	0.0746	0.0756	1.4 %	0.105	0.106	1.0 %	0.0845	0.0860	1.8 %
28.7	0.135	0.136	0.8 %	0.107	0.107	0.0 %	0.154	0.155	0.6 %	0.125	0.125	0.1 %
16.2	0.196	0.197	0.4 %	0.155	0.153	1.0 %	0.229	0.229	0.1 %	0.184	0.182	0.9 %
9.09	0.289	0.289	0.2 %	0.226	0.221	1.9 %	0.344	0.344	0.1 %	0.274	0.269	1.8 %
5.11	0.429	0.427	0.3 %	0.325	0.319	1.7 %	0.521	0.519	0.3 %	0.405	0.397	2.1 %
2.87	0.638	0.635	0.4 %	0.467	0.459	1.6 %	0.791	0.788	0.4 %	0.592	0.583	1.6 %
1.62	0.944	0.942	0.3 %	0.660	0.655	0.9 %	1.19	1.19	0.1 %	0.852	0.847	0.6 %
0.909	1.40	1.40	0.0 %	0.924	0.925	0.2 %	1.80	1.80	0.2 %	1.22	1.22	0.2 %
0.511	2.05	2.06	0.1 %	1.28	1.29	0.3 %	2.70	2.70	0.1 %	1.72	1.72	0.2 %
0.287	3.00	3.00	0.1 %	1.75	1.76	0.3 %	4.01	4.01	0.2 %	2.38	2.38	0.2 %
0.162	4.30	4.30	0.0 %	2.33	2.34	0.8 %	5.86	5.85	0.2 %	3.18	3.21	0.9 %
0.0909	6.05	6.07	0.3 %	3.05	3.06	0.4 %	8.40	8.42	0.2 %	4.19	4.22	0.6 %
0.0511	8.40	8.38	0.1 %	3.91	3.89	0.6 %	11.8	11.8	0.1 %	5.42	5.38	0.7 %

Table 32. Measured and Quemada model viscosity of WBDF 3.

WBDF 4	25°C			50°C			25°C (aged)			50°C (aged)		
	Shear Rate $\dot{\gamma}$ [1/s]	Measured η [Pa·s]	Quemada η [Pa·s]	APE	Measured η [Pa·s]	Quemada η [Pa·s]	APE	Measured η [Pa·s]	Quemada η [Pa·s]	APE	Measured η [Pa·s]	Quemada η [Pa·s]
1020	0.0298	0.0287	3.7 %	0.0217	0.0233	7.5 %	0.0295	0.0290	1.6 %	0.0220	0.0235	7.1 %
511	0.0391	0.0391	0.1 %	0.0290	0.0319	10.2 %	0.0393	0.0401	2.0 %	0.0299	0.0326	8.9 %
287	0.0519	0.0522	0.6 %	0.0394	0.0428	8.8 %	0.0533	0.0544	2.1 %	0.0415	0.0443	7.0 %
162	0.0710	0.0716	0.9 %	0.0555	0.0589	6.2 %	0.0741	0.0757	2.2 %	0.0590	0.0619	5.0 %
90.9	0.100	0.101	0.8 %	0.0804	0.0833	3.6 %	0.107	0.109	1.3 %	0.0867	0.0889	2.5 %
51.1	0.145	0.146	0.3 %	0.118	0.120	1.5 %	0.158	0.159	0.7 %	0.130	0.130	0.7 %
28.7	0.215	0.215	0.1 %	0.177	0.176	0.3 %	0.238	0.238	0.0 %	0.196	0.195	0.6 %
16.2	0.320	0.320	0.0 %	0.265	0.262	1.1 %	0.360	0.360	0.2 %	0.298	0.294	1.3 %
9.09	0.486	0.486	0.1 %	0.400	0.394	1.7 %	0.557	0.554	0.5 %	0.459	0.450	1.9 %
5.11	0.746	0.743	0.3 %	0.607	0.594	2.0 %	0.863	0.859	0.4 %	0.703	0.691	1.6 %
2.87	1.15	1.14	0.1 %	0.916	0.899	1.8 %	1.35	1.34	0.5 %	1.08	1.06	1.3 %
1.62	1.76	1.76	0.2 %	1.36	1.35	0.8 %	2.09	2.09	0.0 %	1.63	1.62	0.4 %
0.909	2.73	2.72	0.1 %	2.04	2.03	0.2 %	3.28	3.28	0.0 %	2.46	2.47	0.1 %
0.511	4.19	4.19	0.1 %	3.01	3.01	0.0 %	5.11	5.11	0.0 %	3.68	3.70	0.5 %
0.287	6.41	6.42	0.1 %	4.39	4.41	0.5 %	7.91	7.91	0.0 %	5.44	5.46	0.4 %
0.162	9.69	9.69	0.0 %	6.30	6.33	0.5 %	12.1	12.1	0.1 %	7.84	7.86	0.3 %
0.0909	14.5	14.5	0.1 %	8.87	8.90	0.4 %	18.3	18.3	0.2 %	11.1	11.1	0.2 %
0.0511	21.3	21.3	0.0 %	12.3	12.2	0.5 %	27.2	27.2	0.1 %	15.2	15.2	0.0 %

Table 33. Measured and Quemada model viscosity of WBDF 4.